Numerical Analysis of Wind Turbine Aerodynamics

Iván Herráez Hernández

Von der Fakultät für Mathematik und Naturwissenschaften
der Carl von Ossietzky Universität Oldenburg
zur Erlangung des Grades und Titels eines

DOKTORS DER INGENIEURWISSENSCHAFTEN
DR. ING.

angenommene Dissertation

von Herrn Iván Herráez Hernández
geboren am 30.01.1979 in Barcelona (Spanien)

CARL VON OSSIETZKY universität OLDENBURG

Gutachter: Prof. Dr. Joachim Peinke
Zweitgutachter: Prof. Dr. Martin Kühn
Tag der Abgabe: 04.01.2016
Tag der Disputation: 22.01.2016

To Zoe and Yara. To their generation.

Contents

Abstract

The flow over the rotor blades of horizontal axis wind turbines is subjected to complex physical mechanisms that are still poorly understood. Even stationary, axisymmetric and uniform inflow conditions can lead to fluid dynamic phenomena not well characterized yet. The root and tip regions of the blade, where the flow is highly three-dimensional and strongly influenced by the trailing vortices, are especially prone to this problem. As a consequence, the characterization of the blade flow can be extremely challenging, what implies a high level of uncertainty in the wind turbine design process. This work addresses this issue by means of computational fluid dynamics (CFD) simulations. The scope is to unveil the physics of the blade aerodynamics, with a special focus on the root and tip flows.

Reynolds Averaged Navier-Stokes (RANS) simulations are used in this work for all the computations in which the true geometry of the blades is simulated. Owing to the high computational cost of Large Eddy Simulations (LES), their utilization is restricted to computations in which the blade geometry is replaced by an actuator line model. All the simulations presented in this thesis are compared with measurements obtained from model wind turbines operating under controlled conditions in wind tunnels. Special emphasis is put on the validation of the flow features governing the root and tip aerodynamics. The agreement between simulations and experiments is in general very good.

Spanwise flows are shown to influence drastically the performance of the blade inboard region when it operates at high angles of attack, both with attached and separated flow. Their origin as well as their significance for the Himmelskamp effect are discussed in detail. The Himmelskamp effect is analysed in two wind turbines and in both cases the lift is enhanced but the drag is not significantly affected. Furthermore, it is shown that the spanwise flows (and correspondingly also the Himmelskamp effect) can be disrupted by vortices trailing from the blade transition regions between different airfoil types. This, however, only occurs if the aerodynamic characteristics of two adjacent airfoils differ much from each other.

The origin and relevance of the root and tip vortices are also investigated in detail. The numerical results show how in the root and tip regions the bound vorticity is deflected from the spanwise towards the chordwise direction, what gives rise to the trailing vortices. However, this process is more gradual at the root than at the tip. Correspondingly, the formation of the root vortex extends over a comparatively large area. This makes the root vortex to present a less defined and distinctive structure than the tip vortex.

The load acting on the chordwise vorticity at the tip and root is orthogonal to the blade chord. This implies that it does not contribute to the power generation. Hence, it can be considered as a conservative load. This load is typically disregarded in all calculation methods based on the blade element theory (e.g. in blade element momentum and actuator line models). However, a detailed study of its role in the turbine aerodynamics suggests that it can slightly modify the blade tip trajectory. In order to prove this hypothesis, an actuator line model is implemented, which automatically computes and applies the conservative force. It is demonstrated that the conservative force induces a short inboard motion of the tip vortex just after release. This, in turn, reduces slightly the turbine performance.

These results show the great potential of CFD for the study of wind turbine aerodynamics. Furthermore, they pave the way for a better characterization of the flow over the rotor blades.

Zusammenfassung

Die Strömung entlang der Rotorblätter von Windkraftanlagen ist komplexen physikalischen Mechanismen ausgesetzt, welche noch immer nicht vollständig verstanden sind. Selbst stationäre, achsensymmetrische und gleichförmige Einströmungen können zu strömungsmechanischen Phänomenen führen, die bisher noch nicht gut charakterisiert sind. Dies ist besonders ausgeprägt an der Blattwurzel und Blattspitze, wo die Strömung hochgradig dreidimensional und stark von den abgelösten Wirbeln abhängig ist. Deswegen kann die Charakterisierung der Strömung um Windkraftanlagenblätter sehr komplex werden, was zu einem hohen Level an Unsicherheit im Designprozess der Windkraftanlagen führt. Diese Arbeit geht diese Problematik unter Nutzung von numerischen Strömungssimulationen (CFD, aus dem Englischen: Computational Fluid Dynamics) an. Ziel ist es, das physikalische Verständnis der Blattaerodynamik zu verbessern. Der Fokus liegt dabei vor allem auf der Strömung um Blattwurzel und Blattspitze.

In dieser Arbeit werden Reynolds-gemittelte Navier-Stokes (RANS, aus dem Englischen: Reynolds-Averaged Navier-Stokes) Simulationen für sämtliche Untersuchungen genutzt, in welchen die Geometrie des Blattes aufgelöst wird. Aufgrund des hohen Rechenaufwands von Grobstruktursimulationen (LES, aus dem Englischen: Large Eddy Simulations), werden die aufgelösten Blattgeometrien durch sogenannte Aktuatorlinien ersetzt. Die Simulationen, die in dieser Arbeit präsentiert werden, werden mit Messungen an Modellwindkraftanlagen verglichen. Die Messungen wurden dabei unter kontrollierten Bedingungen in Windkanälen erfasst. Ein Fokus der Arbeit liegt dabei in der Validierung der Simulationen für die Blattwurzel- und Blattspitzenaerodynamik. Die Übereinstimmung zwischen den Experimenten und den Simulationen ist generell sehr gut.

Es wird gezeigt, dass radiale Strömungen einen drastischen Einfluss auf das aerodynamische Verhalten im Blattwurzelbereich haben, sobald das Blatt mit hohen Angriffswinkel angeströmt wird. Dies ist sowohl bei angelegter als auch bei abgelöster Strömung zu erkennen. Die Herkunft und Bedeutung der radialen Strömung für den Himmelskampeffekt werden im Detail diskutiert und analysiert. Dafür wird der Himmelskampeffekt an zwei Windkraftanlagen untersucht und in beiden Fällen kann gezeigt werden, dass der Auftrieb verstärkt, aber der Widerstand nicht deutlich beeinflusst wird. Des Weiteren wird gezeigt, dass radiale Strömungen (und daher auch der Himmelskampeffekt) durch Wirbelablösungen gestört werden können, welche im übergangsbereich zwischen verschiedenen Blattprofilen entstehen. Dies ist allerdings nur der Fall, wenn sich zwei nebeneinander liegende Profile deutlich unterscheiden.

Der Ursprung und die Relevanz des Blattwurzel- und des Blattspitzenwirbels wird ebenfalls im Detail untersucht. Die numerischen Ergebnisse zeigen, wie die gebundene Vortizität im Blattwurzel- und Blattspitzenbereich von der radialen Richtung in die Sehnenrichtung abgelenkt wird, was die Entstehung von abgelösten Wirbeln verursacht. Da dieser Prozess an der Blattwurzel graduell verläuft, ist die Entstehung des dortigen Wirbels über eine vergleichsweise große Fläche ausgedehnt. Dies sorgt dafür, dass der Wirbel an der Blattwurzel eine weniger definierte und ausgeprägte Form hat als der Blattspitzenwirbel.

Die Lasten, die auf die Vortizität in Sehnenrichtung an der Blattspitze und -wurzel wirken, sind senkrecht zur Blattsehne ausgerichtet. Dies hat zur Folge, dass diese nicht zur Leistungserzeugung beitragen und daher als konservative Kräfte angesehen werden können. Konservative Lasten werden üblicherweise in allen Berechnungsmodellen, welche auf der Blatt-Element-Theorie (z.B. Blatt-Element-Impuls-Theorie und Aktuatorlinien) basieren, ver-

nachlässigt. Eine detaillierte Betrachtung der wirkende Kräfte weist allerdings darauf hin, dass die Vortizität in Sehnenrichtung die Trajektorie des Blattspitzenwirbels evtl. beeinflussen könnte. Um diese Hypothese zu beweisen, wird ein Aktuatorlinien-Modell implementiert, welches automatisch die konservativen Kräfte bestimmt und in der Simulation berücksichtigt. Es wird gezeigt, dass die konservative Kraft zu einer nach innen gerichteten Bewegung des Blattspitzenwirbels kurz nach seiner Entstehung führt. Dies wiederum zieht eine leichte Reduktion der Anlagenleistung nach sich.

Die Ergebnisse dieser Arbeit zeigen das große Potential der CFD für die Untersuchung der Windkraftanlagenaerodynamik. Des Weiteren ebnen sie den Weg für eine bessere Charakterisierung der Strömung entlang von Rotorblättern.

Chapter 1

Introduction

1.1 Motivation of research

Wind power must be rapidly further deployed for addressing the current environmental challenges associated with the generation of electricity. This requires reliable and cost-effective wind turbines. However, the design of wind turbines is currently subjected to a high level of uncertainty, what plays a negative role in the economic feasibility of wind energy. One of the main sources of uncertainty is the aerodynamic behaviour of the rotor, which is subjected to many unsteady effects that are still poorly understood (Leishman, 2002). Indeed, even stationary, homogeneous and axisymmetric inflow conditions lead to several physical phenomena that make the blade section characteristics to deviate substantially from the characteristics obtained from 2D airfoils operating at the same angle of attack (Schepers, 2012). This is especially true for the tip and root blade regions, where several interrelated aerodynamic effects like e.g. spanwise flows, the Himmelskamp effect, aerodynamic losses, flow separation, the root and tip vortices, etc. affect to a great extent the aerodynamic performance. The existence of those effects is known since many decades ago (Himmelskamp, 1947; Glauert, 1935), but they are still far being from well understood and characterized. This thesis aims at shedding light into those effects by means of computational fluid dynamics (CFD) models. This allows not only to gain insight into those phenomena, but also to asses the capabilities and limitations of current state of the art CFD simulations.

1.2 Scope of this thesis

This thesis is devoted to the study of the flow over wind turbine blades by means of Computational Fluid Dynamics (CFD) simulations. Special attention is paid to the study of the tip and root regions of the rotor blades, where the aerodynamic characteristics of the blade sections can deviate substantially from the equivalent two-dimensional profiles operating at the same angle of attack (AoA). The scope can be summarized in the following points:

1. Simulation of wind turbine rotor models with the open-source toolbox OpenFOAM.
2. Validation of the numerical models against experimental results.
3. Analysis of the flow over the blade root and tip regions.

4. Detailed study of the following phenomena affecting the aerodynamic performance of the root and tip:
    - Spanwise flows in the boundary layer.
    - Himmelskamp effect.
    - Origin and evolution of the root and tip vortices.
    - Role of the conservative forces.

1.3 Outline

This thesis is a collection of scientific articles and it is structured in the following way:

- *Chapter 2* introduces the numerical methods used in this work.
- *Chapter 3* presents the simulation of a model wind turbine and its extensive validation against experimental results. Furthermore, the analysis of the results includes the study of radial flows in the boundary layer as well as their interaction with trailing vortices departing from blade radial positions corresponding to the transition between different airfoil types.
- *Chapter 4* is devoted to the detailed study of the root flow. The role and origin of radial flows, Himmelskamp effect as well as root vortex are thoroughly discussed.
- *Chapter 5* focuses on the analysis of the Himmelskamp effect, including its sources and influence on the blade performance.
- *Chapter 6* consists on an exhaustive study of the blade tip flow. The radial flows, the bound vorticity distribution, the origin of the tip vortex and the existence and role of conservative aerodynamic forces are discussed in detail.
- *Chapter 7* verifies the influence of the conservative loads on the tip vortex trajectory and the rotor performance by means of an enhanced actuator line model.
- *Chapter 8* summarizes the main conclusions of this work.
- *Chapter 9* presents suggestions for future work.

Chapter 2

Numerical method

2.1 The governing equations of flow motion

The motion of viscous fluids (e.g. the air flow over wind turbine blades) can be described by means of the Navier-Stokes equations, which are based on the conservation of mass, momentum and energy. The energy equation is disregarded in this thesis, since it is only required for compressible flows (compressible effects are negligible in wind turbines since $Ma < 0.3$). The Navier-Stokes equations assuming constant density can be written in differential, scalar form as:

$$\frac{\partial u}{\partial x} + \frac{\partial v}{\partial y} + \frac{\partial w}{\partial z} = 0 \tag{2.1}$$

$$\rho \frac{Du}{Dt} = -\frac{\partial p}{\partial x} + \frac{\partial \tau_{xx}}{\partial x} + \frac{\partial \tau_{yx}}{\partial y} + \frac{\partial \tau_{zx}}{\partial z} + \rho f_x \tag{2.2}$$

$$\rho \frac{Dv}{Dt} = -\frac{\partial p}{\partial y} + \frac{\partial \tau_{xy}}{\partial x} + \frac{\partial \tau_{yy}}{\partial y} + \frac{\partial \tau_{zy}}{\partial z} + \rho f_y \tag{2.3}$$

$$\rho \frac{Dw}{Dt} = -\frac{\partial p}{\partial z} + \frac{\partial \tau_{xz}}{\partial x} + \frac{\partial \tau_{yz}}{\partial y} + \frac{\partial \tau_{zz}}{\partial z} + \rho f_z \tag{2.4}$$

Eq. 2.1 is the continuity equation and Eq. 2.2-2.4 are the momentum equations for the x,y and z components, respectively. The momentum equations are derived from Newton's second law. The left part of the momentum equations represents the mass acceleration per unit volume, whereas the right part represents the sum of body and surface forces per unit volume. Body forces are forces that act at a certain distance (like e.g. the gravitational and electromagnetic forces). On the contrary, surface forces act directly on the surface of the fluid element. There are two types of surface forces: pressure and friction forces. The friction forces can also be subdivided in two categories: normal and shear stress forces. The first term on the right-hand side of Eq. 2.2-2.4 represents the pressure forces. The second, third and fourth terms are the viscous forces. The fifth term stands for the body forces.

The shear stresses from the viscous terms can be expressed as

$$\tau_{xy} = \tau_{yx} = \mu \left(\frac{\partial v}{\partial x} + \frac{\partial u}{\partial y} \right) \tag{2.5}$$

$$\tau_{yz} = \tau_{zy} = \mu \left(\frac{\partial w}{\partial y} + \frac{\partial v}{\partial z} \right) \tag{2.6}$$

$$\tau_{zx} = \tau_{xz} = \mu \left(\frac{\partial u}{\partial z} + \frac{\partial w}{\partial x} \right) \tag{2.7}$$

where μ is the viscosity coefficient.

The normal stresses τ_{xx}, τ_{yy} and τ_{zz} can be neglected in many cases, since the shear stresses from Eq. 2.5-2.7 are usually much larger. However, if the velocity gradients $\partial u/\partial x$, $\partial v/\partial y$ and $\partial w/\partial z$ are big enough, then the normal stresses can contribute noticeably to the normal force induced by the pressure. The effect of the normal stresses is to expand or compress the volume in the normal direction and they can be computed as

$$\tau_{xx} = 2\mu \frac{\partial u}{\partial x} \tag{2.8}$$

$$\tau_{yy} = 2\mu \frac{\partial v}{\partial y} \tag{2.9}$$

$$\tau_{zz} = 2\mu \frac{\partial w}{\partial z} \tag{2.10}$$

After rearranging Eq. 2.2-2.4 with Eq. 2.5-2.10, we obtain

$$\frac{Du}{Dt} = -\frac{1}{\rho} \frac{\partial p}{\partial x} + \nu \nabla^2 u + f_x \tag{2.11}$$

$$\frac{Dv}{Dt} = -\frac{1}{\rho} \frac{\partial p}{\partial y} + \nu \nabla^2 v + f_y \tag{2.12}$$

$$\frac{Dw}{Dt} = -\frac{1}{\rho} \frac{\partial p}{\partial z} + \nu \nabla^2 w + f_z \tag{2.13}$$

where ν is the dynamic viscosity of the fluid defined as

$$\nu = \frac{\mu}{\rho} \tag{2.14}$$

From Eq. 2.1 and Eq. 2.11-2.13, the Navier-Stokes equations for a three-dimensional, unsteady incompressible fluid can also be written in differential, tensor form as:

$$\frac{\partial u_i}{\partial x_i} = 0 \tag{2.15}$$

$$\frac{\partial u_i}{\partial t} + u_j \frac{\partial u_i}{\partial x_j} = -\frac{1}{\rho} \frac{\partial p}{\partial x_i} + \nu \nabla^2 u_i + f_i \tag{2.16}$$

2.2 Turbulence modelling

The Reynolds number is a fundamental quantity for characterizing the flow regime of a fluid. It relates the relative importance of the inertial to the viscous forces:

$$Re = \frac{|\mathbf{V}|\, L}{\nu} \tag{2.17}$$

where V is the velocity magnitude, L is the characteristic length and ν is the kinematic viscosity. At low Reynolds numbers the flow is laminar and viscous effects play an important role. Under these conditions, adjacent layers of fluid move orderly and smoothly without disrupting each other and without significant lateral mixing. However, at high Reynolds numbers the flow becomes turbulent, presenting continuous chaotic changes in the velocity and pressure fields. These fluctuations are highly three-dimensional and are caused by numerous eddies on many different scales. As a consequence, mixing and diffusion of mass, momentum and energy is increased. The largest eddies extract energy from the mean flow by a process called vortex stretching, in which the eddies are distorted by mean velocity gradients in sheared flows (Versteeg and Malalasekera, 1995). These eddies eventually break up and their energy is transferred to smaller and smaller eddies through the vortex stretching process. This is known as the *energy cascade*. At the smallest scales of turbulence the viscous effects dissipate the kinetic energy into thermal energy.

The transition to turbulence can be caused by different mechanisms, but it is usually related to sheared flows, which cause small disturbances that trigger flow instabilities. These instabilities always occur upstream of the transition point to turbulent flow. The amplification of the flow instabilities leads to areas of concentrated rotational structures, what gives rise to the formation of intense small scale motions and finally to the growth and merging of these areas of small scale motion into fully turbulent flows (Versteeg and Malalasekera, 1995). Different strategies exist for the simulation of turbulent flows. The most common approached are described in the following.

2.2.1 Direct Numerical Simulation

The Direct Numerical Simulation (DNS) method consists on solving numerically the complete Navier-Stokes equations, what allows to compute all turbulence scales. However, solving all scales of turbulence requires a huge number of cells in order to capture the smallest eddies. Furthermore, the use of DNS also requires very accurate, low-dissipative numerical schemes Mockett (2009). This makes this type of simulation unsuitable for most technical applications, especially for high Reynolds number flows. According to Spalart (2000), the computational power required for simulating an aircraft by means of CFD will not be readily available before the year 2080. However, DNS is already used for performing basic turbulence research at low Reynolds numbers (Laizet and Vassilicos, 2011).

2.2.2 Large Eddy Simulation

The Large Eddy Simulation method consists on solving the large scale eddies and modelling the small scales. Large scale eddies contain more energy and transport more effectively the

conserved properties than the small scale eddies (Ferziger and Peric, 2002). Hence, putting the computational effort on solving only the large scale turbulence is an efficient technique (in comparison to the DNS method) and it does not compromise severely the simulation accuracy. Furthermore, modelling the small scale turbulence is comparatively simple because of its isotropic, homogeneous and universal characteristics (in opposition to the anisotropic and problem-specific characteristics of large scale turbulence).

The LES method requires a filter for dividing the flow into large and small scale eddies, i.e. resolved and modelled fields. Different types of filter exist, but all of them have in common the usage of a length scale Δ that sets the limit between large and small eddies. The size of Δ must be greater than the local cell size but it can be either uniform throughout the whole domain or applied as a constant multiple of the local cell size (Mockett, 2009). Two different approaches exist for modelling the effect of turbulence scales smaller than Δ. The first one consists on choosing numerical schemes that resemble the dissipation from small scale turbulence. The second one consists on using a specific mathematical model for describing the subgrid-scale (SGS) turbulence (Mockett, 2009).

Two types of widely used SGS-models are described in the following:

Smagorinsky SGS model

The earliest, simplest and most commonly used sub-grid scale model is the one from Smagorinsky (1963). It belongs to the eddy viscosity type of models and as such it enhances transport and dissipation by means of the eddy viscosity. The subgrid viscosity is modelled as

$$\nu_{sgs} = (C_s \Delta)^2 \sqrt{2 \overline{S_{ij}} \overline{S_{ij}}} \tag{2.18}$$

where Δ is the filter length scale, S_{ij} is the strain rate tensor and C_s is the Smagorinsky parameter, for which different values have been proposed ($C_s \approx 0.2$ for isotropic turbulence). The Smagorinsky model has some drawbacks like the fact that C_s is very dependent on the flow characteristics and therefore it is not a constant. Another issue is the fact that it can not predict transition to turbulence. Furthermore, it requires several modification for modelling realistically wall-bounded flows.

Dynamic SGS models

The mentioned drawbacks of the Smagorinsky model can be partly overcome using a dynamic SGS model, like the one from Germano et al. (1991). In these models the optimal value of C_s is computed automatically and it varies in space and time. Transition is accounted for and wall bounded flows can be well predicted without requiring special modifications like damping functions. However, the use of dynamic SGS models also presents some issues. The main problem is that numerical instabilities often arise when C_s adopts negative values in large space or time ranges.

2.2.3 Reynolds Averaged Navier-Stokes Simulation

The computational cost of both DNS and LES makes those types of simulations prohibitive for most technical applications. However, in many cases the use of Reynolds Averaged Navier-

Stokes Simulations (RANS) is a good alternative that offers a reasonable comprise between simulation accuracy and computational cost. The main idea of RANS is to divide the flow variables into a mean and a fluctuating part:

$$\phi_{x_i,t} = \overline{\phi}(x_i) + \phi'(x_i,t) \tag{2.19}$$

with

$$\overline{\phi}(x_i) = \frac{1}{T}\int_0^T \phi(x_i,t)\,dt \tag{2.20}$$

where t is the time and T is the averaging interval. As Ferziger and Peric (2002) explains, T must be large compared to the time scale of the fluctuations. This is necessary for making the solution time-independent.

When the flow presents more unsteadiness than the one attributed to the turbulence (e.g. because of vortex shedding or time-dependent wall motion), $\overline{\phi}(x_i)$ can not be obtained from time averaging. In that case, ensemble averaging is used:

$$\overline{\phi}(x_i) = \frac{1}{N}\sum_{n=1}^{N} \phi(x_i,t) \tag{2.21}$$

where N is the number of elements in the ensemble. A large number of elements is required for eliminating the influence of the fluctuations (Ferziger and Peric, 2002)

$\overline{\phi}(x_i)$ is solved numerically and $\phi'(x_i,t)$ is modelled by means of dedicated turbulence models.

The application of any of both averaging techniques (Eq. 2.20 and 2.21) leads to the Reynolds-Averaged Navier-Stokes equations. The continuity and momentum equations for incompressible flows become:

$$\frac{\partial \overline{u}_i}{\partial x_i} = 0 \tag{2.22}$$

$$\frac{\partial \overline{u}_i}{\partial t} + \overline{u}_j\frac{\partial \overline{u}_i}{\partial x_j} = -\frac{1}{\rho}\frac{\partial \overline{p}}{\partial x_i} + \nu\nabla^2\overline{u}_i - \frac{\partial}{\partial x_j}\overline{u_i'u_j'} + f_i \tag{2.23}$$

Equations 2.22 and 2.23 highly resemble the unmodified Navier-Stokes equations from Eq. 2.15 and 2.16. The only differences are the time averaging of the flow variables and the additional tensor $\overline{u_i'u_j'}$, which is known as Reynolds stress tensor. This tensor describes the fluctuations owed to the turbulence but it leads to a closure problem because it is a new unknown. Hence, a turbulence model is required for approximating this variable.

Eddy viscosity models

The Boussinesq hypothesis addresses the turbulence closure problem by introducing the turbulent eddy viscosity ν_t for coupling the Reynolds stresses with the mean velocity gradients. This method is based on the assumption that the effects of turbulence are similar to an increased viscosity (Mockett, 2009):

$$\overline{u_i'u_j'} = -\frac{2}{3}k\,\delta_{ij} - \nu_t\left(\frac{\partial \overline{u}_i}{\partial \overline{x_j}} + \frac{\partial \overline{u}_j}{\overline{x_i}}\right) \tag{2.24}$$

The strain tensor S_{ij} is defined as

$$S_{ij} = \frac{1}{2}\left(\frac{\partial \overline{u}_i}{x_j} + \frac{\partial \overline{u}_j}{x_i}\right) \tag{2.25}$$

so that Eq. 2.24 can be written as

$$\overline{u_i' u_j'} = -\frac{2}{3} k\,\delta_{ij} - 2\,\nu_t\,S_{ij} \tag{2.26}$$

Many turbulence models are based on the Boussinesq approximation for closing the RANS equations. Those models are termed *eddy viscosity models* and they are used for determining the unknown ν_t. Some widely used examples of such models are presented in the following.

Spalart-Allmaras' turbulence model

The Spalart-Allmaras Spalart and Allmaras (1994) turbulence model is a robust one-equation model that has proven to work well for wall-bounded attached flows with adverse pressure gradients. It was designed for aeronautic applications, what makes it also suitable for the simulation of wind turbines. Furthermore, since it only solves one equation, it is faster than two-equation turbulence models. However, its prediction capabilities are substantially diminished with separated flows.

The transport equation is solved for a viscosity-like variable known as $\tilde{\nu}$. The relationship between the ν_t and $\tilde{\nu}$ is:

$$\nu_t = \tilde{\nu}\,f_{v1}, \qquad f_{v1} = \frac{\chi^3}{\chi^3 + c_{v1}^3}, \qquad \chi = \frac{\tilde{\nu}}{\nu} \tag{2.27}$$

And the transport equation is:

$$\frac{D\tilde{\nu}}{Dt} = P - D + T + \frac{1}{\sigma}\left[\nabla\cdot((\nu+\tilde{\nu})) + c_{b2}\,(\nabla\tilde{\nu})^2\right] \tag{2.28}$$

where the production P, wall destruction D and trip terms T are

$$P = c_{b1}\,(1-f_{t2})\,\tilde{S}\tilde{\nu}, \quad D = \left(c_{w1}\,f_w - \frac{c_{b1}}{k^2} f_{t2}\right)\left[\frac{\tilde{\nu}}{d}\right]^2, \quad T = f_{t1}\,(\Delta u)^2 \tag{2.29}$$

and where $\tilde{S}$ is the modified vorticity:

$$\tilde{S} = S + \frac{\tilde{\nu}}{k^2 d^2} f_{v2}, \quad f_{v2} = 1 - \frac{\chi}{1+\chi\,f_{v1}} \tag{2.30}$$

Standard $k-\varepsilon$ turbulence model

The standard $k-\varepsilon$ turbulence model (Launder and Spalding, 1974) is a very widespread two-equations model that obtains the turbulent eddy viscosity ν_t from the transported variables k and ε, which represent the turbulent kinetic energy and the turbulent dissipation, respectively:

$$\nu_t = C_\mu\,k^{1/2}\,l = C_\mu\frac{k^2}{\varepsilon}, \quad l = \frac{k^{3/2}}{\varepsilon} \tag{2.31}$$

The transport equation for k is

$$\frac{\partial k}{\partial t} + u_j \frac{\partial k}{\partial x_j} = \tau_{ij} \frac{\partial u_i}{\partial x_j} - \varepsilon + \frac{\partial}{\partial x_j} \left[\left(\mu + \frac{\nu_t}{\sigma_k} \right) \frac{\partial k}{\partial x_j} \right] \tag{2.32}$$

and the transport equation for ε is

$$\frac{\partial \varepsilon}{\partial t} + u_i \frac{\partial \varepsilon}{\partial x_i} = C_{\varepsilon 1} \frac{\varepsilon}{k} \tau_{ij} \frac{\partial u_i}{\partial x_j} - C_{\varepsilon 2} \frac{\varepsilon^2}{k} + \frac{\partial}{\partial x_j} \left[\left(\mu + \frac{\mu_t}{\sigma_\varepsilon} \right) \frac{\partial \varepsilon}{\partial x_j} \right] \tag{2.33}$$

The model coefficients can be found e.g. in Wilcox (1998) In spite of its high stability and its popularity for many types of flows, this model is rather unsuitable for large adverse pressure gradients (Wilcox, 1998) and rotating flows. Therefore, it is not the best option for the simulation of wind turbine blades.

Wilcox's $k-\omega$ turbulence model

The Wilcox's $k-\omega$ turbulence model is also a widely used two-equation turbulence model that obtains the turbulent eddy viscosity ν_t from the transported variables k and ω, which represent the turbulent kinetic energy and its specific rate of dissipation, respectively.

The turbulent eddy viscosity ν_t is obtained from k and ω in the following way:

$$\nu_t = \frac{k}{\omega} \tag{2.34}$$

The transport equation for k is

$$\frac{\partial k}{\partial t} + u_j \frac{\partial k}{\partial x_j} = \tau_{ij} \frac{\partial u_i}{\partial x_j} - \beta^* k\omega + \frac{\partial}{\partial x_j} \left[(\nu + \sigma^* \nu_t) \frac{\partial k}{\partial x_j} \right] \tag{2.35}$$

and the transport equation for ω is

$$\frac{\partial \omega}{\partial t} + u_j \frac{\partial \omega}{\partial x_j} = \alpha \frac{\omega}{k} \tau_{ij} \frac{\partial u_i}{\partial x_j} - \beta \omega^2 + \frac{\partial}{\partial x_j} \left[(\nu + \sigma \nu_t) \frac{\partial \omega}{\partial x_j} \right] \tag{2.36}$$

The recommended value for the different closure coefficients can be found in Wilcox (1998). The $k-\omega$ turbulence model is better suited than $k-\varepsilon$ for wall-bounded flows with adverse pressure gradients. However, its performance for free shear flows is rather poor.

Menter's $k-\omega$ Shear-Stress-Transport turbulence model

The $k-\omega$ Shear-Stress-Transport model was developed by Menter (1993) and it combines the advantages of both the $k-\varepsilon$ and $k-\omega$ models. The wall bounded-flow is computed following a $k-\omega$ formulation, whereas the free shear flow makes use of the $k-\varepsilon$ model. Switching between both types of formulations is achieved by means of the blending function F_1.

The following expression relates the turbulent eddy viscosity ν_t with k and ω:

$$\nu_t = \frac{\alpha_1 k}{max(\alpha_1 \omega, SF_2)} \tag{2.37}$$

The transport equation for k is

$$\frac{\partial k}{\partial t} + u_j \frac{\partial k}{\partial x_j} = min\left(\tau_{ij}\frac{\partial u_i}{\partial x_j}, 10\beta^* k\omega\right) - \beta^* k\omega + \frac{\partial}{\partial x_j}\left[(\nu + \sigma_k \nu_t)\frac{\partial k}{\partial x_j}\right] \tag{2.38}$$

and the transport equation for ω becomes

$$\frac{\partial \omega}{\partial t} + u_j \frac{\partial \omega}{\partial x_j} = \alpha S^2 - \beta\omega^2 + \frac{\partial}{\partial x_j}\left[(\nu + \sigma_\omega \nu_t)\frac{\partial \omega}{\partial x_j}\right] + 2(1-F_1)\sigma_{\omega 2}\frac{1}{\omega}\frac{\partial k}{\partial x_i}\frac{\partial \omega}{\partial x_i} \tag{2.39}$$

The blending functions F_1 and F_2 as well as the model coefficients are documented in Menter (1994).

This model is often the preferred option for large adverse pressure gradients with separated flow. However, it is computationally more expensive than the other turbulence models previously described.

Reynolds stress models

A more advanced approach for closing the RANS equations consists on directly computing the Reynolds stress tensor, as Launder et al. (1975) first proposed. This type of model is called Reynolds Stress Model (RSM) or Reynolds Transport Model (RTM). It presents a greater complexity than eddy viscosity models but it has the advantage that the turbulence is not assumed to be isotropic (as it is the case for the eddy viscosity models). Hence, all components of the turbulent transport are computed individually. RSM models are more general than eddy viscosity models and therefore they can be applied to many different cases. One of its drawbacks is that they are computationally expensive. Furthermore, in spite of the fact that RSM models are in principle more physically-sound than eddy viscosity models, they had so far only moderate success on predicting real flows (Ferziger and Peric, 2002).

Wall treatment

There are two different methods for treating turbulence in the wall region by means of RANS models: either using a high or a low Reynolds number approach. The low-Re approach consists on resolving the equations of the turbulence model in the whole boundary layer. This requires a very fine grid resolution in the boundary layer, since the first mesh point needs to be placed at the dimensionless wall distance $y^+ < 5$ (ideally $y^+ \approx 1$ or lower) for properly resolving the strong velocity gradients in that region. Recall that y^+ is defined as

$$y^+ = \frac{y u_\tau}{\nu}, \qquad u_\tau = \sqrt{\frac{\tau_w}{\rho}} \tag{2.40}$$

with y the distance from the wall, u_τ the friction velocity, ν the kinematic viscosity, τ_w the wall shear stress and ρ the fluid density. On the contrary, the high-Re approach allows to place the first grid point at a distance $30 \leq y^+ \leq 300$, implying an important reduction in the number of cells. This is achieved by making use of *wall functions*, which are based on the law of the wall and allow to prescribe the velocity profile in the inner layer of the boundary layer. The law of the wall divides the inner boundary layer into the following sublayers:

- viscous sublayer: $y^+ < 5$
- buffer layer: $5 < y^+ < 25$
- log-law region: $25 < y^+ < 250$

As Fig. 2.1 shows, the dimensionless velocity u^+ in the y^+ range corresponding to the viscous sublayer can be approximated as:

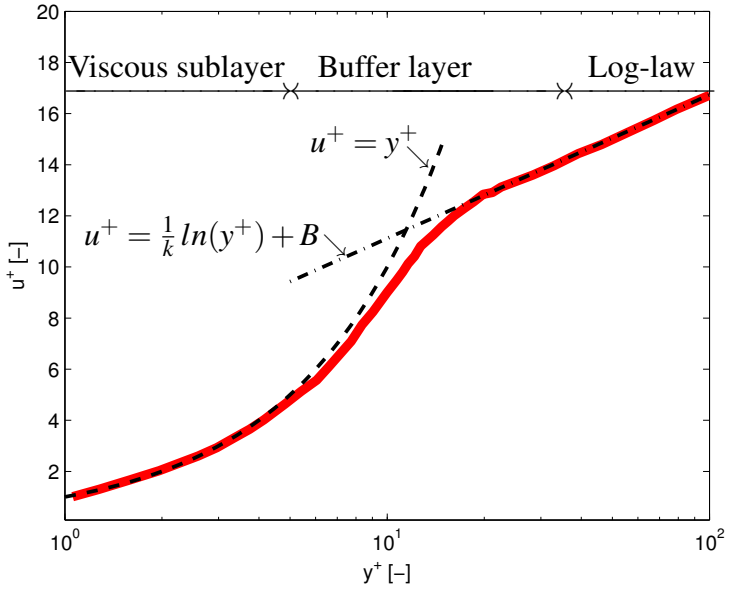

Figure 2.1: Law of the wall representing the three regions of the inner part of a turbulent boundary layer. The red line displays the real velocity profile and the black lines indicate a mathematical approximation for the viscous sublayer and the log-law region.

$$u^+ = y^+ \tag{2.41}$$

and the following expression can be applied to the y^+ range corresponding to the log-law region:

$$u^+ = \frac{1}{k} ln(y^+) + B \tag{2.42}$$

where $k = 0.41$ and $B = 5.1$.

Hence, the velocity in the inner part of the boundary layer can be quite accurately prescribed with a wall function if the first grid point is placed in the log-law region. It is however important to recall that the mentioned law only applies to attached turbulent boundary layers. Hence, the application of wall functions to separated flows is fundamentally wrong. An important problem of both the high-Re and low-Re approaches is that both of them are very restrictive in terms of the grid requirements. As described above, the required height of the first layer of cells depends on the local y^+ , and hence also on the friction velocity u_τ (as shown in Eq.

2.40). Therefore, the wall-bounded flow needs to be known prior to generating the mesh. This information is only rarely available, though, so producing an adequate grid is an iterative process that is only stopped when all the wall regions present a suitable range of y^+. A possible solution for overcoming this issue is the utilization of so-called *adaptive* (also known as *continuous*) wall functions. This type of wall functions can switch automatically between a high-Re and a low-Re approach depending on the local y^+. A blending function allows a smooth transition between both approaches.

2.2.4 Detached Eddy Simulations

Although several hybrid RANS-LES methods have been proposed in the last years, the Detached Eddy Simulation (DES) approach, which was introduced by Spalart et al. (1997), has received most attention. This method represents an effort for combining the advantages of LES and RANS, i.e. enhancing the simulation accuracy with respect to RANS without increasing too much the computational cost. The main idea is to simulate with RANS the boundary layer of the considered geometry and to resolve by means of LES the free shear flow (i.e. the *detached* flow). The turbulence model must therefore work as a RANS model in areas of wall-bounded flow and as a subgrid-scale model in areas outside the boundary layer. This implies that the point of separation is predicted by the RANS model, what can be considered as a substantial drawback of DES since predicting separation is one of the weak points of RANS. In fact, the high dependency of DES on the underlying RANS model has been identified as one of the main issues of DES (Mockett, 2009). Another important challenge associated to DES is the transition region between RANS and LES, where turbulence fluctuations should be transmitted from the RANS solution to LES. Since RANS does not really resolve turbulence but just models its influence, no realistic turbulence can be convected into the LES area.

2.3 Selection of numerical methods for this work

The flow over the blades of wind turbines is viscous and incompressible ($Ma < 0.3$). Therefore, in this work the energy equation was disregarded.

The DNS method for treating turbulence (Sect. 2.2.1) was ruled out from the beginning due to its prohibitive computational cost. The same applies to the application of the LES method (Sect. 2.2.2) for the simulation of wall-bounded flows. However, LES simulations were performed for cases in which the true geometry of the blade was replaced by an actuator line. The use of the actuator line technique prevented from resolving the blade boundary layer, what allowed to drastically reduce the computational cost. The standard Smagorinky subgrid-scale model was chosen for the LES simulations because of its simplicity, robustness and stability (see Sect. 2.2.2). The use of this type of simulations was restricted to the analysis of the tip vortex trajectory since the actuator line technique is not suitable for the study of the flow over the blades (this is due to the huge simplification of the blade geometry).

The RANS method was used for all the simulations in which the true geometry of the blade was considered. The turbulence closure problem was addressed with the Spalart-Allmaras and the $k-\omega\,SST$ turbulence models (see Sect. 2.2.3 for a description of those models). At early stages of this work, the available meshing tools did not allow for an optimal control of the

grid quality. Therefore, the Spalart-Allmaras model was the preferred option because of its robustness, simplicity, computational-efficiency and suitability for aerodynamic simulations with large adverse pressure gradients. The mentioned meshing limitations also prevented from generating suitable meshes for treating the turbulence in the boundary layer consistently with a low-Re approach. Therefore, an *adaptive* wall function was used for switching automatically between a high-Re and a low-Re approach depending on the local non-dimensional wall distance y^+ (see Sect. 2.2.3 for more information). The use of standard wall functions was ruled out because of their unsuitability for the simulation of separated flows.

At a later stage, when the quality of the meshes could be enhanced thanks to a new meshing tool, the $k-\omega\,SST$ model became the preferred option because of its greater adequacy for predicting flow separation. Furthermore, the greater mesh control of the boundary layer region allowed to use a low-Re approach for the wall treatment along the whole blade.

2.3.1 Own developments in OpenFOAM

All the simulations have been performed with the open source C++ object-oriented library OpenFOAM (2015). OpenFOAM is a finite-volume toolbox for performing numerical simulations of partial differential equations. It offers over 80 solvers for different kinds of CFD simulations and over 170 utilities for pre- and post-processing tasks. However, the standard libraries from OpenFOAM often had to be adapted or extended for carrying out the investigations presented in this work. Also, a large number of Matlab scripts were implemented for postprocessing the numerical results. Examples of such tools include routines for computing the angle of attack, the aerodynamic forces, the bound vorticity and circulation, etc. Different types of mesh motion algorithms were also implemented. Some solvers were modified for meeting the requirements of the research. For instance, a laminar solver with pressure-velocity coupling based on the PISO algorithm was adapted for solving turbulent flows with the PIMPLE algorithm. Another example is the actuator line model used in Chapter 7, which is an extension of the standard SOWFA (2015) package. The modifications performed in this model include the following features:

- Calculation of the bound radial and chordwise circulation.
- Calculation and application of the conservative load at the blade tip.
- Pressure-velocity coupling based on the PIMPLE algorithm.
- Implementation of different types of tip correction models (Shen et al., 2005).
- Implementation of different types of blade element distribution along the blade span.
- Implementation of different methods for computing and applying automatically the regularization parameter ε (Shives and Crawford, 2013; Jha et al., 2014).

Much work has also been devoted to the mesh generation process. The meshing tool from OpenFOAM for structured grids, known as blockMesh, is only suited for very simple meshes with few blocks. Doing complex grids with that tool is nearly impossible without writing dedicated automatization scripts. Therefore, several utilities were written for the automatic meshing of airfoils.

Chapter 3

CFD simulation of a wind turbine[1]

Abstract CFD (Computational Fluid Dynamics) simulations are a very promising method for predicting the aerodynamic behavior of wind turbines in an inexpensive and accurate way. One of the major drawbacks of this method is the lack of validated models. As a consequence, the reliability of numerical results is often difficult to assess. The MEXICO project aimed at solving this problem by providing the project partners with high quality measurements of a 4.5 meters rotor diameter wind turbine operating under controlled conditions. The large measurement data-set allows the validation of all kind of aerodynamic models. This work summarizes our efforts for validating a CFD model based on the open source software OpenFoam. Both steady-state and time-accurate simulations have been performed with the Spalart-Allmaras turbulence model for several operating conditions. In this paper we concentrate on axisymmetric inflow for 5 different wind speeds corresponding to flow states ranging from pre- to post-stall. The numerical results are compared with pressure distributions from several blade sections and PIV-flow data from the near wake region. In general, a reasonable agreement between measurements and simulations is found. Some discrepancies, which require further research, are also discussed. Special attention is devoted to the vortices trailing from the blade at high wind speeds and to their influence on the radial pumping mechanism.

3.1 Introduction

The unsteady nature of wind makes the flow over wind turbine blades extremely difficult to predict. Indeed, even with stationary inflow conditions, complex unsteady phenomena will occur, including flow separation, secondary flows and stall delay due to rotational augmentation Leishman (2002). CFD simulations are a very promising method for predicting accurately the flow over the blades (Duque et al., 1999, 2003; Le Pape and Lecanu, 2004; Johansen et al., 2002; Johansen and Sørensen, 2004; Sørensen and Schreck, 2012). Once the flow characteristics are well predicted and understood, improved and efficient engineering models can be developed for avoiding the high computational cost of CFD (Schepers, 2012). Detailed measurements of wind turbines operating under controlled conditions are required for performing extensive

[1]This chapter is an extended and improved version of the article published as I. HERRÁEZ, W. MEDJROUBI, B. STOEVESANDT and J. PEINKE, Aerodynamic Simulation of the MEXICO Rotor, *Journal of Physics: Conference Series*, **555**, 012051, 2014

validations. The aim of the MEXICO project (Snel et al., 1993) was to provide the project partners with the afore mentioned data for validation purposes. The available measurements, which cover different operating conditions, have been used within the project MexNext IEA Task 29 by 20 research institutions from 11 different countries for validating numerical models and for the analysis of aerodynamic effects (Bechmann et al., 2011; Shen et al., 2012; Nilsson et al., 2015a; Sørensen et al., 2014). In this work we summarize our efforts for validating a CFD model of the Mexico-turbine based on the open source toolbox OpenFOAM (2015). We focus on axisymmetric inflow conditions under different wind speeds, keeping the rotational speed and pitch angle constant. The simulations correspond to five different cases ranging from fully attached to fully separated flow conditions. The numerical results are compared with Particle Image Velocimetry (PIV) measurements, experimental surface pressure data and tower loads. Special emphasis is put in the analysis of the trailing vortices and their relevance for the radial pumping effect.

The MEXICO experiment and the numerical method are described in Sect. 3.2. Section 3.3 presents the results of this study, focusing first in the validation of the numerical model (Sect. 3.3.1) and then in the study of the radial flows and trailing vortices (Sect. 3.3.2). Finally, the conclusions of this work are summarized in Sect. 3.4.

3.2 Methods

This section begins with a description of the MEXICO experiment. Afterwards, the numerical method and computational mesh are presented. Finally, the method used for calculating the angle of attack (AoA) is explained.

3.2.1 Experimental data

The MEXICO project stands for Model Experiments in Controlled Conditions. The measurement campaign took place in December 2006 and involved the extensive measuring of load, pressure and flow data from a 3 bladed wind turbine placed in the Large Low-Speed Facility (LLF) of the German-Dutch Wind tunnel DNW, which has an open section of 9.5x9.5 m^2 (Schepers and Snel, 2007; Schepers et al., 2011). The blockage ratio of the wind tunnel is 18 % and the use of breathing slots behind the collector helps to reduce tunnel effects. Prior studies by other project-partners show that tunnel effects do not influence dramatically the rotor flow (Réthoré et al., 2011). The wind turbine has a rotor diameter of 4.5 m. The blades rotate in clockwise direction and are twisted and tapered. Their design is based on 3 different aerodynamic profiles, as seen in Table 3.1.

As it can be seen in Fig. 3.1, the RISØ-A1-21 lift characteristics are substantially different from the two other airfoils, especially in the stall onset and post-stall range (Boorsma and Schepers, 2003). As it will be seen later, this is a critical issue for the MEXICO turbine.

A zig-zag tape placed at 5 % of the chord was used on both the suction and pressure sides of the blades for triggering the laminar to turbulent flow transition. The material used for the blades is Aluminium 7075-T651 Alloy. The tower center is located 2.1 m downwind from the rotor, and its influence on the rotor flow is believed to be minimal. The measurements were carried out under several flow conditions, including 2 different rotational speeds (324 rpm and 424 rpm),

Table 3.1: Airfoil type distribution along the span of the MEXICO blade

Radial position [%]	Radius [m]	Airfoil type
9-17	0.21-0.375	Cylinder
17-20	0.375-0.45	Transition
20-50	0.45-1.125	DU91-W2-250
50-54	1.125-1.225	Transition
54-70	1.225-1.575	RISØ-A1-21
70-74	1.575-1.675	Transition
74-100	1.675-2.250	NACA64-418

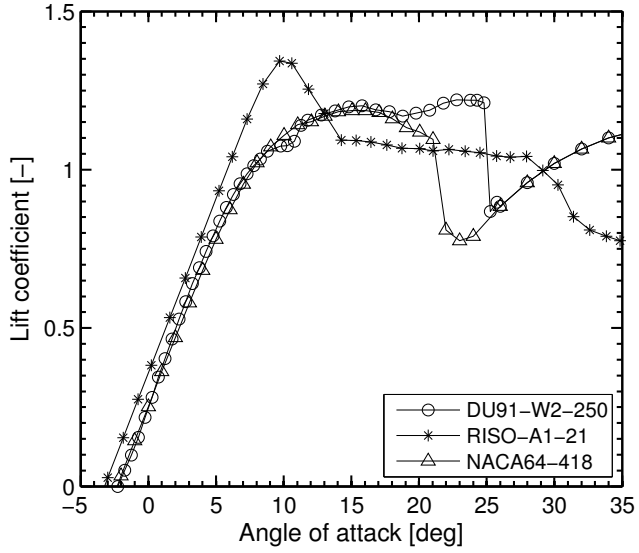

Figure 3.1: Lift curves for the 3 airfoil types used in the MEXICO experiment.

several wind speeds (ranging from 10 to 30 m/s), several pitch angles (from -5.3 deg to 1.7 deg) and several yaw-inflow angles (from 0 deg to 45 deg). The pressure measurements were performed by means of Kulite transducers placed at 5 different blade sections corresponding to 25% , 35%, 60%, 82% and 92% blade span positions. Some pressure transducers located at the 0.25 blade span position were malfunctioning during most of the measurements, so they are disregarded in this work. The PIV measurements were performed along multiple PIV windows upstream and downstream of the turbine. Two radial and two axial traverses were performed. Unfortunately, only outer radial positions can be analyzed with the available PIV data, since the innermost PIV-data are at the 45 % radial position. This is an important draw-back for the study of 3D effects, which play a major role in the inner region of the blades. In this work five different wind speeds have been considered (10 m/s, 15 m/s, 19 m/s, 24 m/s and 30 m/s), while the rotational speed has been kept constant at 424.4 rpm. The rated wind speed is 15 m/s. For higher wind speeds the blades present flow separation. The Reynolds number varies

between $3.5 \cdot 10^5$ at the blade root to $7 \cdot 10^5$ at the blade tip. The tip speed is 100 m/s for all cases, resulting in a tip speed ratio of 6.7 at design conditions (15 m/s). The Mach number is well below 0.3 and compressible effects can be disregarded.

Further details about the experiment can be found in Boorsma and Schepers (2003).

3.2.2 Numerical method

The simulations have been performed with the open source C++ object-oriented library OpenFoam (OpenFOAM, 2015). OpenFoam is a finite-volume toolbox for performing numerical simulations of partial differential equations. It offers over 80 solvers, for performing different kinds of CFD simulations and over 170 utilities for performing pre- and post-processing tasks. Most of the solvers and many of the utilities can be run in parallel by means of Message Passing Interface (MPI).

Steady state and time-accurate simulations have been performed in this work. The steady state simulations rely on the Reynolds Averaged Navier-Stokes (RANS) method. The time-accurate simulations rely on the Unsteady Reynolds Averaged Navier-Stokes (URANS) method. The rotation of the blades can be simulated in different ways. In the present simulations the "frozen rotor" method was chosen for the steady state simulations. For the time-accurate simulations an sliding mesh approach is used. In the frozen rotor approach the rotating flow field is solved in a non-inertial reference system, whereas the non-rotating parts are solved in an inertial reference system. The Coriolis and centrifugal forces are added to the momentum equation in the regions subjected to rotation. In this way, it is possible to simulate a rotating system without a moving mesh. This allows a considerable speed-up of the simulations. The relative position of the rotor and the stator remains constant for the whole simulation. This is an obvious disadvantage when a strong rotor-stator interaction is expected. In the case of the MEXICO turbine, the interaction between the rotor (blades) and the stator (tower) is believed to be negligible. Consequently the tower is not modelled. This implies that the flow unsteadiness is not resolved in time. The use of unsteady simulations with sliding meshes is useful when the above mentioned limitations can influence negatively the solution. The solver used for the frozen rotor simulations can deal with multiple reference frames (MRF) and uses the SIMPLE algorithm for pressure-velocity coupling. Hence its name MRFSimpleFoam. It is an incompressible, isotherm, turbulent and stationary flow solver. The transient simulations make use of the so called General Grid Interface (GGI) between the rotor and the stator. This approach allows for a relative mesh motion between the rotor and the stator, avoiding at the same time mesh topology modifications. This is done by means of a special algorithm that allows the interpolation of the flow variables between the GGI interfaces. Both meshes (the moving and the static meshes) can be conformal or non-conformal. Since no tower was modelled in the MEXICO turbine, the interest of performing simulations with the sliding mesh was only to obtain a time-dependent solution. This should in principle allow a better prediction of unstationary effects. The use of GGI implies the calculation of weighting factors for every facet, originating from the geometric intersection of the faces of the rotor and the stator interfaces. This is done in order to ensure flux conservation between both parts. The price that has to be paid for the enhanced accuracy and more realistic flow prediction of the unsteady simulations with moving meshes is a much higher computational cost. The solver used for the transient simulations, named pimpleDyMFoam, is an incompressible, isotherm, turbulent solver which can deal with moving meshes. It

makes use of the PIMPLE algorithm for the pressure-velocity coupling. The PIMPLE algorithm is a hybrid of the standard SIMPLE and PISO algorithms that allows the use large time steps. The 2nd order linear-upwind discretization scheme has been used in this work for the convective terms of both the steady-state and the transient simulations. The time is discretized with a 2nd-order backward formulation. The simulations, which are run fully turbulent, make use of the Spalart and Allmaras (1994) turbulence model. The transient computations use the steady-state results as a pre-solution. All the simulations have been run at the FLOW computer cluster (FLOW, 2015) of the University of Oldenburg using 240 processors. The steady-state computations reached convergence in less than 5 hours. For the transient simulations, however, more than 1 week was required for solving 4 rotor revolutions. The wind speed at the inlet and the pressure at the outlet were set to Dirichlet boundary conditions. The pressure at the outlet was always set to atmospheric pressure. No-slip boundary conditions were set for the blades and the nacelle. For the wind speed at the outlet and the pressure at the inlet Neumann conditions (zero gradient) were used. At the interfaces between the moving and the static part of the mesh, a special GGI boundary condition was used.

The same mesh was used for all the simulations. As explained above, only the blades and the nacelle were simulated. The high computational cost of the transient simulations made it necessary to keep the number of grid cells as low as possible. On the other hand, the high requirements on the solution quality made it advisable to use a fine mesh. After several computations with different meshes, it was decided that the best compromise between computational cost and solution accuracy was offered by a mesh with $11 \cdot 10^6$ cells. The mesh was made with the tool snappyHexMesh, which is included in the OpenFOAM (2015) package. In fact, the mesh consist of a non-moving mesh merged to a moving mesh. The domain is cylindrical, with a radius of 16 m and a length of 52 m. The rotating region has a radius of 6 m and a length of 14.5 m. Most of the cells are hexaedrons, although split hexaedrons are also present in the proximity of the boundary layer. The boundary layer of the blades was resolved with 10 prism-layers. For the nacelle, 3 prism-layers were used. Since wall functions were employed in the computations, an extremely fine resolution of the cells in the boundary layer could be avoided. The y+ value on the blades oscillated between 50 and 200. The wake and the regions where high gradients were expected were accordingly refined. In figure 3.2, showing a slice of the mesh at the inboard region of one blade, a refinement region in the vicinity of the blade can be seen.

3.3 Results and discussion

Steady-state simulations have been performed for all wind speeds. Furthermore, transient simulations have been computed for the cases with 15 and 24 m/s (i.e. stall onset and post-stall conditions). The scope of performing transient simulations was to assert if the results vary substantially as compared to the steady-state simulations, what would imply that important transient effects dominate the blade aerodynamics under axial inflow conditions. However, only minor differences were found between numerical results from steady state and transient simulations. This is consistent with the observations done by Sørensen et al. (2002) with steady and unsteady RANS computations of the UAE Phase VI wind turbine. Consequently, the simulation of more transient runs would not be justified considering their very high computational cost. Hence,

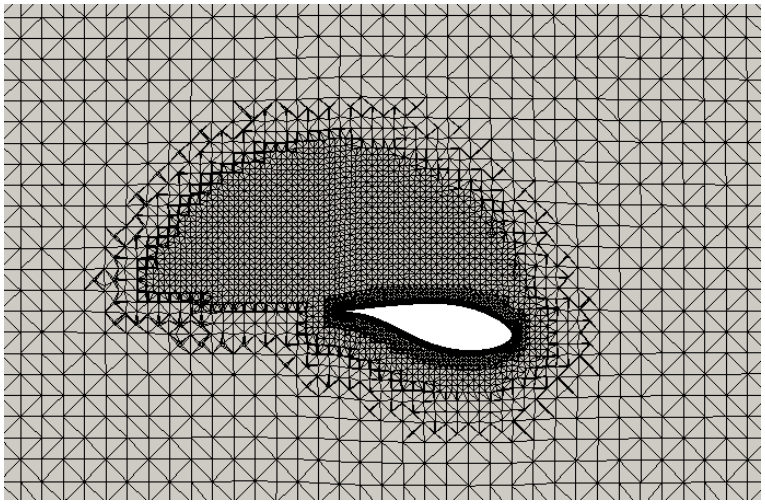

Figure 3.2: Detail of a mesh slice, showing a blade section and the adjacent refinement region.

the numerical results presented in this work correspond to steady-state simulations, except for the 15 and 24 m/s cases, where the results are taken from transient simulations, and then are averaged over the last 4 rotor revolutions.

It is worth remarking that in the experimental results for the 10 and 15 m/s cases, the wind speed at several rotor diameters upwind of the rotor is about 9.7 and 14.7 m/s, respectively. The reason for this effect is not clear yet, but it is probably related to the high tunnel blockage when the rotor is heavily loaded. Consequently, in the CFD simulations the inflow wind speed for the mentioned cases has been set to 9.7 and 14.7 m/s.

3.3.1 Validation of the numerical model

Thrust force

The axial force is the most reliable load that can be extracted from the tower balance. The rest of the loads were apparently too low for the operating range of the balance, leading to very inconsistent measurements. Therefore, the thrust force of the rotor, which is aligned with the axial force measured by the balance, is used here for a first validation of the model. Furthermore, this integrated load presents the advantage that it is very representative of the flow state, so it gives a good idea of the accuracy of the model. The axial force measured by the balance includes both the tower drag and the rotor thrust. Hence, the tower drag must be estimated and subtracted from the axial force for obtaining the rotor thrust.

The range of Reynolds numbers corresponding to the tower for the considered wind speeds goes from $Re = 2.7 \times 10^5$ to $Re = 8.3 \times 10^5$. The drag crisis for a cylinder is known to take place at approximately $Re = 4 \times 10^5$ (although this value also depends among other things on the surface roughness). This suggests that only a very coarse approximation of the tower drag can be obtained for the considered wind speeds. However, the fact that the tower had a helical strake around its outer walls helps to delay remarkably the drag crisis. This effect was seen among

others by Kwon et al. (2002) in their experimental work in the field of offshore structures and by Constantinides and Oakley (2006) in their numerical investigations in the same field. The drag force coefficient remains therefore stable for the whole range of considered Reynolds numbers, and its estimation is of reasonable accuracy. A parked rotor case with a wind speed of 30 m/s and the blades pitched to feathered position has been chosen as a reference for the estimation of the tower drag force coefficient. At those conditions the rotor thrust is assumed to be negligible in comparison to the tower drag. Therefore, the axial force measured by the balance is assumed to correspond to the tower drag. Using the equation

$$C_{D_{tower}} = \frac{F_{axial}}{0.5\rho H_{tower} D_{tower} U_{wind}^2} \tag{3.1}$$

a tower drag coefficient $C_{D_{tower}}$ equal to 1.11 is obtained. F_{axial} is the axial force measured by the balance, ρ is the air density, H_{tower} is the tower height, D_{tower} is the tower diameter and U_{wind} is the wind speed. $C_{D_{tower}}$ is then used for calculating the tower drag force associated with every considered wind speed. Finally, the tower drag force is subtracted from F_{axial} for calculating the rotor thrust force. The experimental rotor thrust force obtained in this way is plotted against the numerical results in Fig. 3.3 and, as it is shown, a very good agreement between measurements and simulations is achieved. At 30 m/s, where the blade is completely stalled, the simulations slightly overpredict the thrust force. However, this is still a good prediction considering the limitations of the RANS method in simulating separated flows.

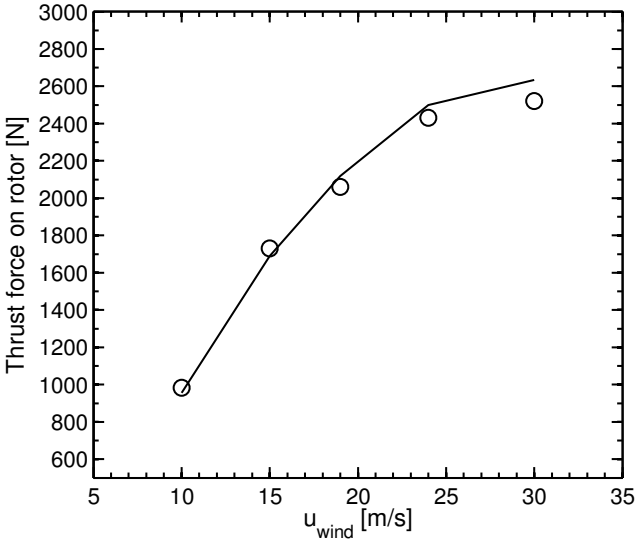

Figure 3.3: Thrust force on the rotor for different wind speeds. Lines are simulations and circles are experiments.

Surface pressure distributions

The simulated and measured C_p distributions for five wind speeds and five radial blade stations are plotted in Fig. 3.4. As observed by Schepers and Snel (2007), some sensors in the

inboard region of the blade were malfunctioning during the measurements, especially at low wind speeds. This can be seen e.g. in Fig. 3.4-a at 25% radius, where the numerical results seem more reliable than the measurements. In the cases where the sensors are working properly,

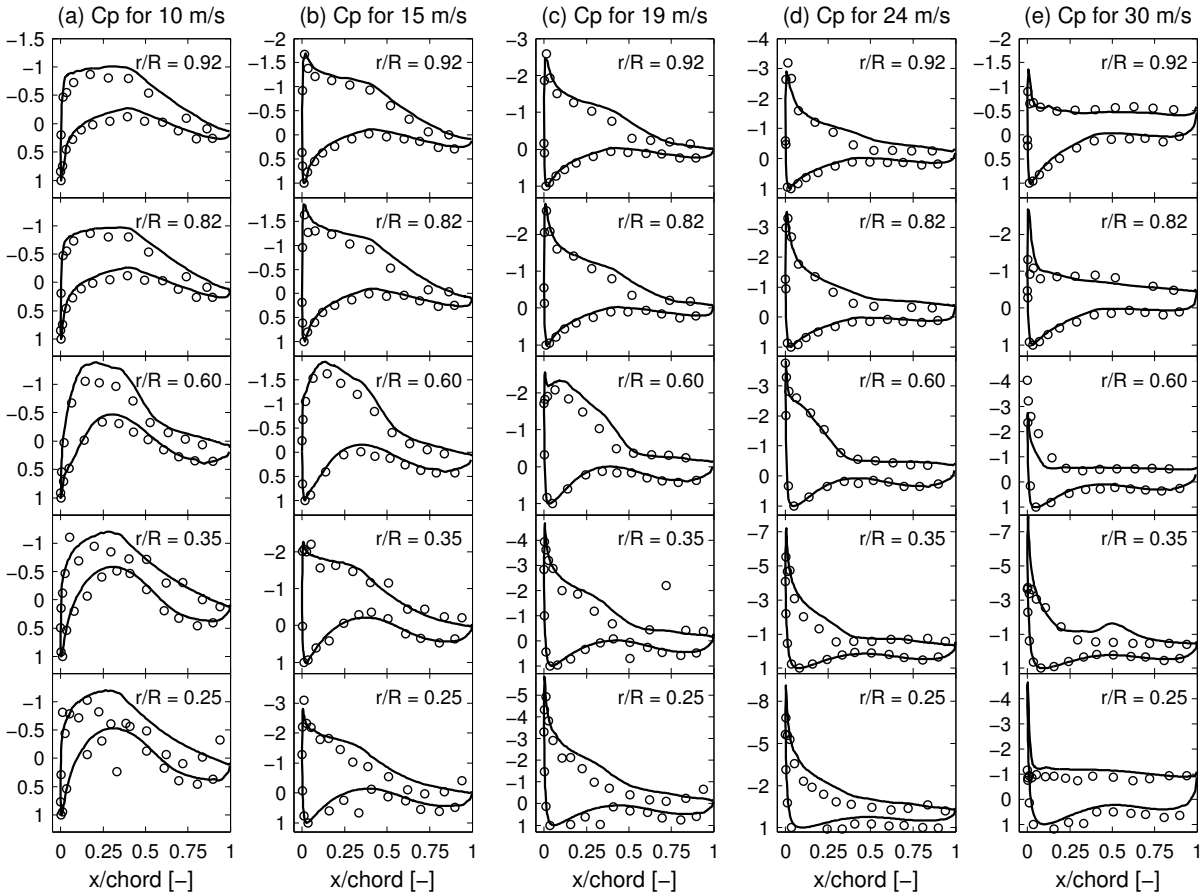

Figure 3.4: C_p distributions for 5 radial stations and 5 different wind speeds: a) 10 m/s, b) 15 m/s, c) 19 m/s, d) 24 m/s and e) 30 m/s. Circles are measurements and solid lines are simulations.

in general a fairly good agreement between experimental and numerical results exists. At 10 m/s (Fig. 3.4-a) the simulations tend to slightly underpredict the pressure on the upper blade surface, especially at 60 % radius. This occurs probably because the simulations were run fully turbulent, whereas in the experiment a zig-zag tape was used at 5% chord for triggering the laminar to turbulent transition. The same trend is seen at 15 m/s (Fig. 3.4-b) and 19 m/s (Fig. 3.4-c). On the other hand, at 24 m/s (Fig. 3.4-d) and 30 m/s (Fig. 3.4-e) this trend is much less pronounced. The reason for this is that the separation point moves closer to the leading edge at high wind speeds (being the rotational speed constant, an increase in wind speed involves a rise in the AoA and consequently greater flow separation). Correspondingly, when the separation point is located before the zig-zag tape or in its proximity, the influence of the zig-zag tape on the pressure distribution is minimized. Performing simulations with a fixed point of laminar-

turbulent transition should help to improve the accuracy of the numerical results at low wind speeds.

At 19 m/s (Fig. 3.4-c) the predicted adverse pressure gradient on the upper blade surface is a bit delayed with respect to the experimental results. This is a well known problem of RANS simulations, which commonly have difficulties at predicting accurately the point of separation (Johansen and Sørensen, 2004).

The pressure distribution at 24 m/s (Fig. 3.4-d) and 60% radius is especially important because it is very close to the location at which the trailing of a strong vortex is supposed to take place at this wind speed, as it will be shown in Section 3.3.1 and 3.3.2. As it is observed, the agreement between numerical and experimental results at this station is very good, which again confirms the optimal prediction of the flow characteristics by the CFD model.

At 30 m/s (see Fig. 3.4-e), massive flow separation is present along the complete blade span, leading to a flat pressure distribution along the whole chord length (or most of it) on the upper blade surface. The simulations tend to overpredict the suction peak at the leading edge, which at some stations is almost non existing in the measurements. This explains the light overprediction of the thrust force at 30 m/s (see Fig. 3.3).

Wind speed traverses

An axial traverse has been extracted from the PIV experiments for comparing the measured wind speed (which has been averaged over time) with the simulations (Fig. 3.5). The PIV interrogation windows were located in the horizontal plane at the 9 o'clock position. The axial traverse is therefore in that horizontal plane and it is parallel to the axis of rotation of the turbine. The distance between the axial traverse and the axis of rotation is 1.37 m. The measurements were carried out when blade 1 was pointing upwards (12 o'clock position). The comparison is performed for the three wind speeds for which PIV measurements are available, namely 10, 15 and 24 m/s, i.e. pre-stall, design and post-stall conditions. For the 24 m/s case, an excellent agreement is achieved. The wind speed fluctuations observed downstream of the rotor are related to turbulent wake structures, which is characteristic for separated flows. It is important to notice that the simulations are able to predict in great detail the wake turbulence, showing the high level of accuracy obtained for such complex flow conditions. At 15 m/s, the measurements also show wind speed fluctuations in the wake. Apparently, the blade begins to stall at this wind speed, which corresponds to the design conditions of the MEXICO rotor. However, the simulations do not predict a turbulent wake. This is again attributed to the limitations of RANS for predicting the stall onset. At 10 m/s the flow is satisfactorily predicted, with only a light overprediction of the wind speed in the near-wake region.

A radial traverse located 1.53 m behind the rotor plane has been extracted from the PIV measurements in a similar fashion like the axial traverse. The radial traverse is also in the 9 o'clock horizontal plane, and it is orthogonal to the rotor axis of rotation. Fig. 3.6 shows the comparison between experimental and numerical results for an inflow wind speed of 24 m/s. The interpretation of the experimental results has been the object of much discussion (Schepers et al., 2011). We attribute the sudden wind speed drop observed experimentally at around 1.25 m radius to an edge effect of the PIV window. The edges of the PIV interrogation windows are usually slightly overlapped in order to avoid such effects. However, this radial position corresponds to the bottom border of the innermost PIV window, so no overlapping with other

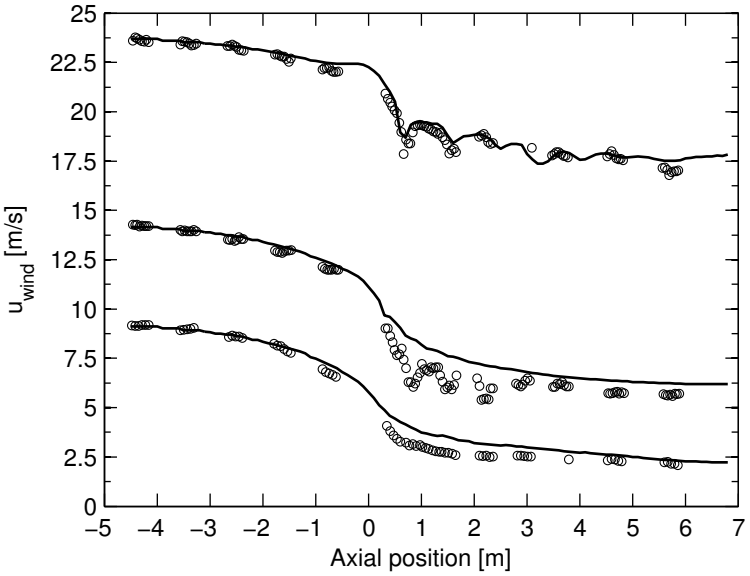

Figure 3.5: Axial traverse of the wind speed for three inflow wind speeds: 10, 15 and 24 m/s. Symbols are measurements and solid lines are simulations. The 0 m axial position corresponds to the rotor plane and positive axial positions represent the rotor wake.

window was possible. This wind speed drop is also visible at other radial traverses located at different axial positions and wind speeds. This confirms that the drop is unrealistic and it is caused by an experimental error. Apart from that, the radial distribution of the wind speed presents important fluctuations along the measured region. As it is shown, the numerical results also display the mentioned fluctuations, and a good qualitative agreement is obtained.

3.3.2 Trailing vorticity

This section is devoted to the study of the trailing vorticity behaviour in the MEXICO rotor.

Fig. 3.7 shows numerical results displaying the isovorticity contours in the plane where the PIV windows are located (9 o'clock position). Blade 1 is at the 12 o'clock position, corresponding to the azimuthal position at which the PIV measurements are performed. As it can be seen, the radial traverse (represented with the vertical line in the wake) crosses a trailing vortex departing from the mid-span region. This is the reason for the strong velocity fluctuations seen in Fig. 3.6. Schepers et al. (2011) suggested the existence of a strong vortex in this blade region, which is now confirmed by our numerical results.

Fig. 3.8 shows by means of streamlines of the relative wind speed the departure from the blade of the mentioned vortex. As it can be seen, the origin of the vortex is on the suction side of the blade root. Hence, air is "pumped" from the root outwards. This effect of "radial pumping" has been commonly observed experimentally (using wool tufts) (Robinson et al., 1999) and numerically (Sørensen et al., 2002) in other turbines operating under stall conditions. Indeed, it is commonly considered as a major source of rotational effects (Sørensen et al., 2002; Schreck et al., 2007; Lindenburg, 2003). One more interesting feature of the standing vortex is its high

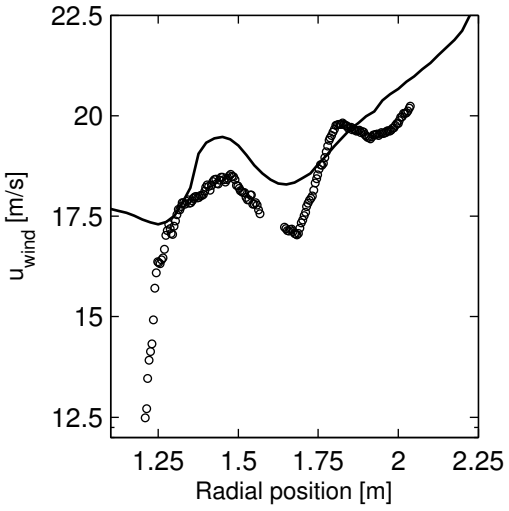

Figure 3.6: Radial traverse at 1.53 m radial position for 24 m/s inflow wind speed. Blade 1 is at the 12 o'clock position and the PIV traverse is at the 9 o'clock position. Symbols are measurements and solid lines are simulations.

stability over all the computed time. This is consistent with the experimental observations done by Robinson et al. (1999) and Schreck and Robinson (2002). Both works focused on the UAE Phase VI wind turbine, the former on the downwind configuration and the latter in the upwind configuration. In both cases the high stability of the radial pumping effect was highlighted.

Further insight is gained by investigating the radial distributions of the normal and tangential forces (F_n and F_t, respectively), which are obtained by integrating the pressure distributions.

Fig. 3.9 shows the normal and tangential forces (F_n and F_t, respectively) along the blade span. The experimental results are only available for five radial stations. The numerical results, which have a much higher resolution, offer additional information for understanding the blade aerodynamics. A good agreement between measurements and simulations is found for F_n at all wind speeds. The predicted F_t is not always consistent with the experiments at separated flow conditions. However, it must be noticed that determining F_t experimentally from pressure distributions is often connected to a considerable level of uncertainty, since it highly depends on the density of sensors in the leading edge region. Nevertheless, the consistency between experiments and simulations is in general good, especially when the flow is attached, i.e. at low wind speeds and at outboard positions (where the AoA is lower).

At 10 and 15 m/s, i.e. when the flow is mainly attached and 2D, no significant oscillations in the F_n (Fig. 3.9-e, 3.9-d) and F_t (Fig. 3.9-j, 3.9-i) distributions occur. However, from 19 m/s onwards, i.e. at stall conditions, great F_n and F_t fluctuations take place at outboard positions.

At 19 m/s an important drop in F_n (Fig. 3.9-c) and F_t (Fig. 3.9-h) exists at 75% radius. This radial position corresponds to the end of the transition from the RISØ-A1-21 to the NACA 64-418 airfoils (see Table 3.1). The AoA at this location for the given wind speed is 11°, which matches approximately with the stall onset of the RISØ-A1-21 airfoil, but is still about 4° before the AoA of maximum lift in the NACA 64-418 airfoil. Therefore, the C_l coefficients associated

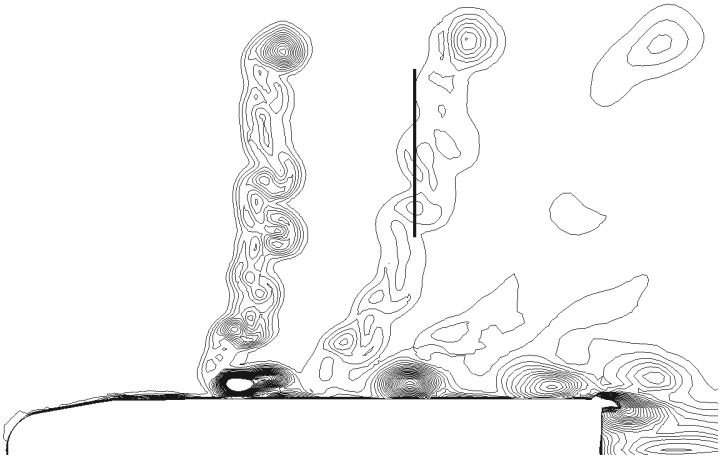

Figure 3.7: Isovorticity contour extracted from numerical results showing the plane where the radial traverse is located (9 o'clock position) when blade 1 is at the 12 o'clock position. The vertical line represents the position of the radial traverse. Inflow wind speed is 24 m/s.

with both airfoil types for this AoA are very different from each other (see Fig. 3.1). The important change in C_l and hence in bound circulation results in increased trailing vorticity, what affects negatively the aerodynamic performance.

At 24 m/s, two important fluctuations can be recognized in the F_n (Fig. 3.9-b) and F_t (Fig. 3.9-g) distributions. The first one takes place at 55% radius, i.e. just at the end of the transition between the DU91-W2-250 and the RISØ-A1-21 airfoils. The corresponding AoA is 16°, which is related with great disparities in C_l between both airfoils (see Fig. 3.1). As a result, a vortex is trailed from that location (see also Fig. 3.9). As it was previously described, this vortex disrupts the radial pumping effect, which is associated to 3D rotational effects. Hence, the existence of this vortex is expected to play a substantial role in the aerodynamic performance of the rotor (particularly in relation to the rotational effects) .

A second and stronger drop in F_n and F_t at 24 m/s takes place at 85% radius, i.e. in the NACA 64-418 airfoil region. The AoA at this location is 14°, corresponding approximately to the stall onset (see Fig. 3.1).

At 30 m/s (Fig. 3.9-a and 3.9-f) the blades are completely stalled, with most of the flow already separating at the leading edge. Accordingly, the blades present extremely high oscillations in F_n and F_t all along the blade span.

Summarizing, trailing vorticity along the span is not significant at pre-stall conditions (except at the tip and root, of course). However, at stall and post-stall conditions, trailing vortices exist in the transition regions between airfoil types. This is due to the disparities in aerodynamic characteristics of the different blade sections. Further, the changes in AoA in the vicinity of the trailing vortices (induced by the corresponding upwash and downwash) are particularly critical when the AoA is in the proximity of the stall onset, since they can lead to attached flow on one side of the trailing vortex and separated flow on the other side, implying important fluctuations in the aerodynamic forces. The existence of trailing vortices along the span can affect the radial pumping or create interactions with the tip vortex, influencing in both cases the blade

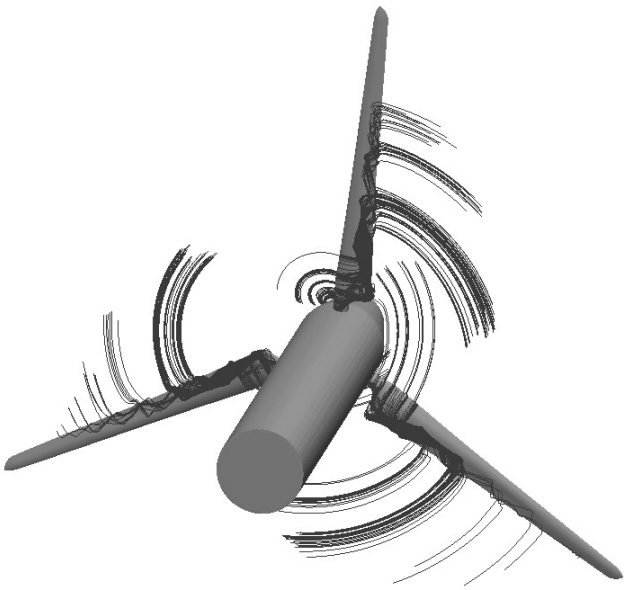

Figure 3.8: Streamlines of the relative wind speed over the blade upper surface, showing a strong standing vortex on the upper surface of every blade, which pumps air from the root region outwards. The inflow wind speed is 24 m/s.

performance.

It is worth mentioning that Tangler (2004), who studied the experimental data of the NREL UAE Phase VI wind turbine, made similar observations about the trailing vorticity in that rotor. More specifically, the author also suggested the existence (under certain conditions) of a mid-span vortex, which supposedly emanated from a standing vortex on the upper surface of the blade. Furthermore, he saw the same influence of the vortex-induced upwash and downwash on the AoA. This indicates, that the effects observed in the MEXICO turbine might be common also in other rotors, even if their blade design is not based on airfoils with significant disparities in their characteristics (the UAE Phase VI blade is based exclusively on the S809 airfoil).

One more interesting feature of the F_n and F_t force distributions along the blade span is how they evolve from low to high wind speeds: At low wind speeds (attached flow), the region of the blade producing the highest aerodynamic forces is the tip. When the wind speed increases (stall conditions), the tangential force, i.e. the force contributing the most to the driving torque, is greater at inboard locations. This is very meaningful, because inboard locations are subjected to greater separation owing to the thicker airfoil type and greater AoA (the twist angle does not completely compensate for the higher inflow angle). The existence of rotational effects at inboard positions make therefore the rotating blades behaviour to differ substantially from stationary blades, where flow separation is connected to a reduction in aerodynamic performance.

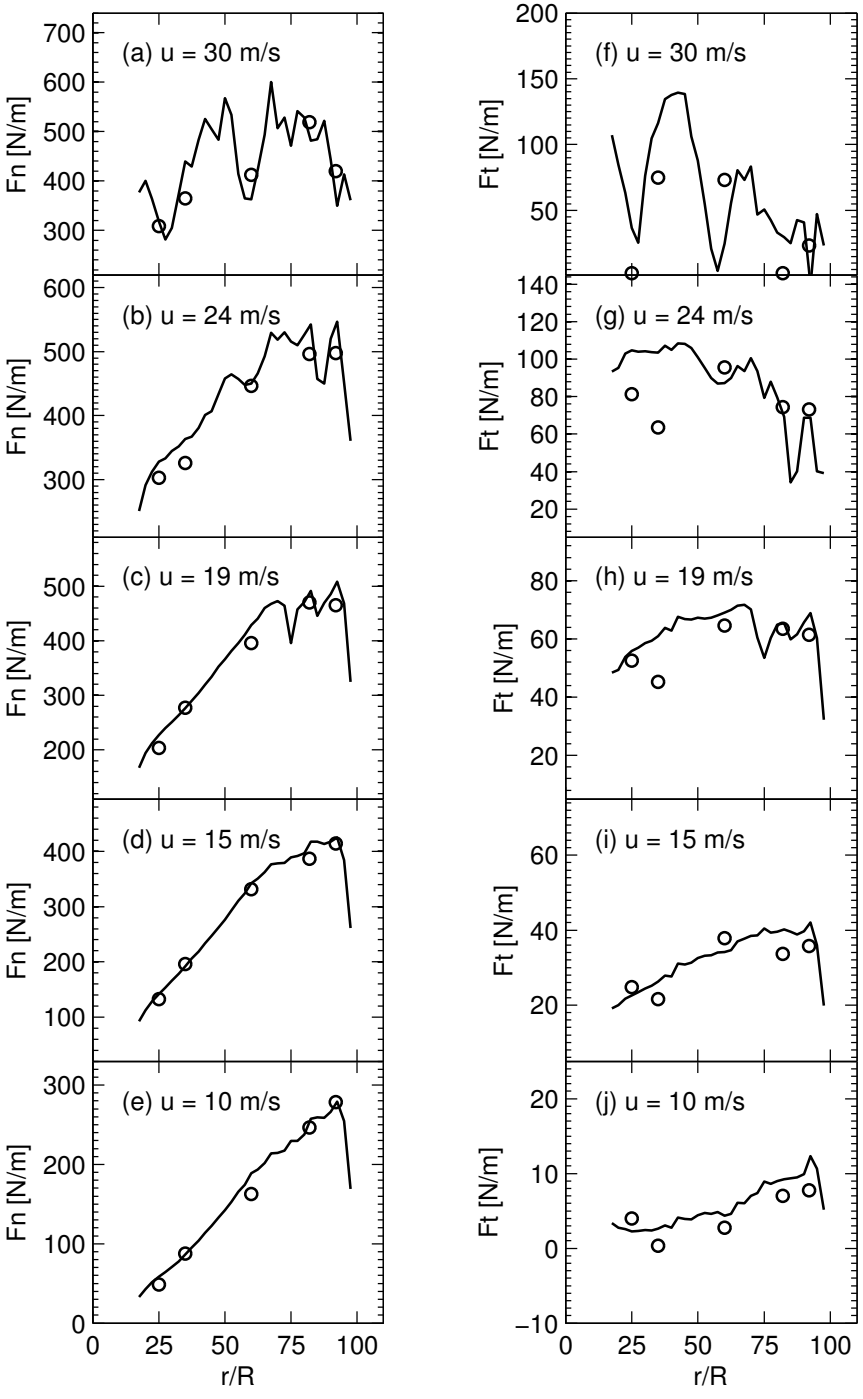

Figure 3.9: Normal and tangential force along the blade span for 5 different wind speeds. Circles are measurements and solid lines are simulations.

3.4 Conclusions

A CFD model of the MEXICO wind turbine based on the open source code OpenFOAM has been successfully validated against experimental data. This validation enabled the synergetic use of numerical and experimental results for the study of the trailing vortices and their interaction with the radial pumping effect, which in turn is related to the rotational effects that make 3D blade characteristics to deviate substantially from 2D airfoil data. The authors infer that the use of rather incompatible airfoil types of the MEXICO rotor leads to increased trailing vorticity at mid-span positions. In that region, the radial pumping effect is disrupted as a consequence of a trailing vortex. This is believed to play an important role for the 3D rotational effects on the blade.

Chapter 4

Insight into the blade root flow[1]

Abstract The root flow of wind turbine blades is subjected to complex physical mechanisms that influence significantly the rotor aerodynamic performance. Spanwise flows, the Himmelskamp effect and the formation of the root vortex are examples of interrelated aerodynamic phenomena observed in the blade root region. In this study we address those phenomena by means of Particle Image Velocimetry (PIV) measurements and Reynolds Averaged Navier-Stokes (RANS) simulations. The numerical results obtained in this study are in very good agreement with the experiments and unveil the details of the intricate root flow. The Himmelskamp effect is shown to delay the stall onset and enhance the lift force coefficient C_l even at a moderate angle of attack (AoA $\approx 13^\circ$). The results also show that the vortex emanating from the spanwise position of maximum chord length rotates in the opposite direction of the root vortex, what affects the wake evolution.

4.1 Introduction

The aerodynamic design of wind turbine blades is subjected to important levels of uncertainty. As a matter of fact, not only transient operational states can pose a challenge to the wind turbine designer, but also seemingly simple cases involving steady operation under axisymmetric, uniform inflow conditions (Leishman, 2002; Schepers, 2012). This is especially true for the tip and root regions of the blades, where the flow is three-dimensional and strongly influenced by the trailing vortices (Micallef, 2012).

Spanwise flows and Himmelskamp effect

At the root of the blade, the angle of attack (AoA) is usually considerably higher than at the tip. This increases the complexity of the flow, since it often leads to flow separation, what in this part of the blade generally gives rise to the Himmelskamp effect (Himmelskamp, 1947). This effect delays the stall onset and enhances the lift force as compared to non-rotating blades operating at the same AoA. The Himmelskamp effect, also known as *stall delay* or *rotational*

[1] Accepted for publication as discussion paper as I. HERRÁEZ, B. AKAY, G.J.W. VAN BUSSEL, J. PEINKE and B. STOEVESANDT: Detailed Analysis of the Blade Root Flow of a Horizontal Axis Wind Turbine, *Wind Energ. Sci.*.

augmentation, has been studied by many authors both experimentally (Schreck and Robinson, 2002; Sicot et al., 2008; Ronsten, 1992) and numerically (Guntur and Sørensen, 2014; Herráez et al., 2014; Schreck et al., 2007), although it still remains far from being well understood and characterized. It mainly affects the blade root region and is known to be closely related to the existence of spanwise flows in the boundary layer. Snel et al. (1993) were the first to propose a correction model to be applied to 2D airfoil characteristics in order to account for this effect in Blade Element Momentum (BEM) and other engineering tools that rely in 2D airfoil data. More correction models have been developed since then (Chaviaropoulos and Hansen, 2000; Bak et al., 2006; Raj, 2000; Corrigan and Schillings, 1994, etc.). However, Breton et al. (2008) and Guntur et al. (2011) proved that their accuracy is still a critical issue. Currently, a major impediment in the development of accurate correction models is the incomplete understanding of the physical mechanisms. It is worth highlighting that, up to now, the study of the Himmelskamp effect has been mostly focused on post-stall conditions. Consequently, very little is known about its onset at moderate angles of attack.

The root vortex

One fundamental feature of the root (and tip) flow is the formation of trailing vorticity that rolls up into a discrete vortex. Several authors have attempted to capture experimentally the root vortex in the near wake of a wind turbine. However, as Vermeer et al. (2003) highlighted, this can be extremely difficult to achieve due to the fact that the near wake usually does not present a distinctive, well defined root vortex (opposite to the tip vortex). Many wind tunnel experiments with model wind turbines confirmed this. For instance, Massouh and Dobrev (2007) and Haans et al. (2008) also came to that conclusion after studying a wind turbine rotor wake with Particle Image Velocimetry (PIV) and hot film wake measurements, respectively. Furthermore, Ebert and Wood (2001) and Sherry et al. (2013) observed by means of PIV (among other measurement techniques) that the root vortex diffuses very rapidly. The PIV measurements performed by Akay et al. (2012b) on two different rotors demonstrated that the evolution and strength of the root vortex highly depends on the blade root geometry and the spanwise distribution of circulation. In a subsequent work also based on PIV measurements, Akay et al. (2014) suggested that the flow in the root region is driven by the bound vorticity.

The study of the root (and tip) vortices can also be addressed by means of numerical simulations. For this purpose, Large Eddy Simulations (LES) are commonly combined with actuator line models (Ivanell et al., 2007; Troldborg et al., 2007; Nilsson et al., 2015b). This technique is very useful for analysing the evolution of the trailing vortices in the wake. However, it implies a very strong simplification of the blade geometry, what makes it unsuitable for studying the origin of the root and tip vortices. This is well exemplified in van Kuik et al. (2014), where it is concluded that the fact that actuator line models disregard the chordwise bound circulation at the blade tip prevents them from computing correctly the tip vortex trajectory in the vicinity of the blade. The same article also shows that full blade Reynolds Averaged Navier-Stokes Simulations (RANS) as well as panel code computations allow a much more realistic study of the tip vortex formation mechanism. Indeed, the use of a panel code allowed Micallef et al. (2012) to study the origin of the tip vortex on a wind tunnel model rotor, unveiling the complex distribution of bound vorticity at the blade tip. However, to the best of our knowledge, the origin of the root vortex has still not been addressed in detail up to now.

Scope and outline

This article aims at gaining insight both experimentally and numerically into the root flow of a horizontal axis wind turbine operating at design conditions. The focus is put into two important and interrelated aspects of the root flow that, as above explained, are insufficiently understood so far:

1. Spanwise flows and onset of the Himmelskamp effect at moderate angles of attack (design operating conditions)

2. The origin of the root vortex

Section 4.2.1 and Sect. 4.2.2 describe the experimental and numerical set-up, respectively. The main characteristics of the flow over the root region are presented in Sect. 4.3.1. Furthermore, in this section the simulations are validated against experimental results. The presence of spanwise flows is further discussed in Sect. 4.3.2. Section 4.3.3 addresses the onset of the Himmelskamp effect. The origin of the root vortex is analysed in Sect. 4.3.4. Finally, the main conclusions of this work are summarized in Sect. 4.4.

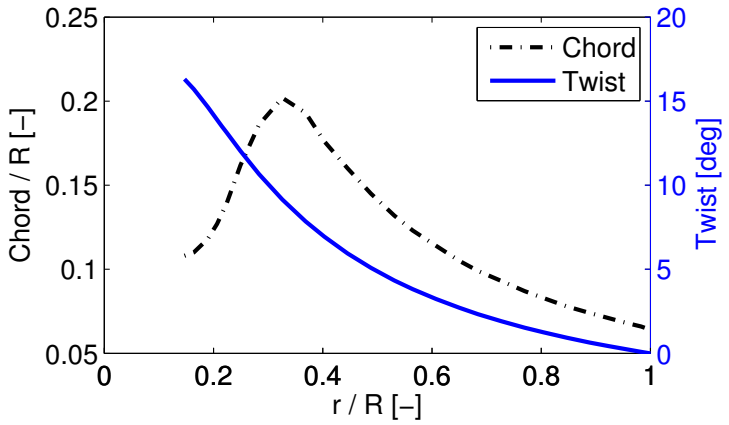

Figure 4.1: Chord and twist distribution along the blade span.

4.2 Methods

4.2.1 Experimental setup

The scope of the experimental campaign is to measure the three components of the flow over the root region of a wind turbine blade. This is achieved by means of stereoscopic Particle Image Velocimetry (PIV).

The measurements are carried out in the Open Jet Facility of the Faculty of Aerospace Engineering at the Delft University of Technology. This wind tunnel has an octagonal open jet with an equivalent diameter of 3 m. The studied wind turbine consists of a two-bladed rotor with a diameter of 2 m. The chord and twist distributions are shown in Fig. 4.2.1. Table 4.1 shows the used airfoil types.

Table 4.1: Airfoil type distribution along the blade span

Radial position range $[r/R]$	Airfoil type
0.14 - 0.16	Cylinder
0.16 - 0.21	Transition
0.21 - 1.0	DU96-W-180

The measurement campaign includes both a spanwise and a chordwise configuration of the PIV windows. The spanwise measurements are carried out at different azimuth angles for capturing the evolution of the near wake. In the chordwise configuration the PIV windows are orthogonal to the blade axis around the blade chord. This configuration, which included 40 different radial positions, offers the best insight into the flow around the blade surface.

The measurements are phase-locked and phase-averaged with the azimuthal position of the rotor blade rotation. This allows to reconstruct the flow over each blade section after measuring the pressure and suction sides separately.

The rotor operated at rated conditions with a freestream wind speed $U_\infty = 6$ m/s and a rotational speed $\omega = 400$ rpm (tip speed ratio $\lambda = 7$). The turbulence intensity is $TI = 0.28\%$ and there is no yaw misalignment. The Reynolds number at the radial position of maximum chord reached $Re \approx 1.5 \times 10^5$.

Further details about the experimental set-up can be found in Akay et al. (2014).

4.2.2 Numerical method and computational mesh

The simulations presented in this work are based on the Reynolds-Averaged Navier-Stokes (RANS) method and they are performed with the open source code OpenFOAM (OpenFOAM, 2015). The computational model solves the incompressible Navier-Stokes equations using a finite volume approach for the spatial discretization. The convective terms are discretized with a second order linear-upwind scheme. For the viscous terms a second-order central differences linear scheme is employed. The use of a non-inertial reference frame and the addition of the Coriolis and centrifugal forces to the momentum equations allows to account for the rotation of the system. The SIMPLE algorithm is employed for enforcing the pressure-velocity coupling. The turbulence in the boundary layer is modelled by means of the $k-\omega$ Shear-Stress Transport (SST) model proposed by Menter (1993).

The grid is generated with the software Pointwise (Pointwise, 2015). It exploits the symmetry of the rotor by modelling only one half of it and using periodic boundary conditions. The computational domain is represented in Fig. 4.3 and it consists of two independent block-structured grids connected by means of a so called arbitrary mesh interface. The outer grid is a

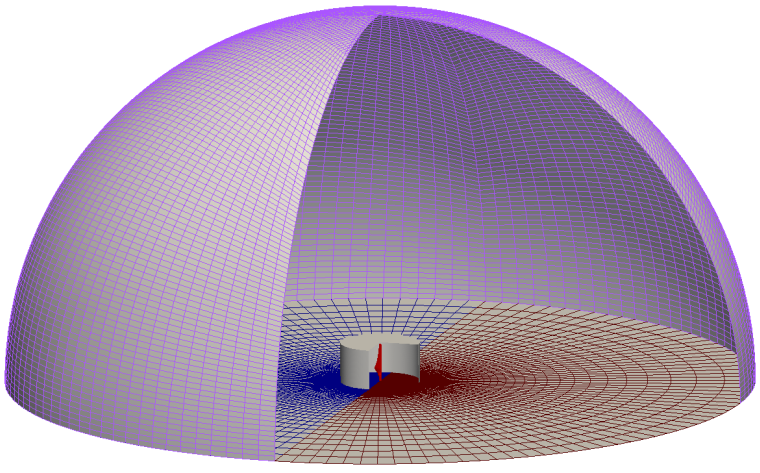

Figure 4.2: Schematic representation of the computational domain. The inner cylinder represents the arbitrary mesh interface.

semi-sphere with the radius 22R, where R is the blade radius. The inner grid, which contains the blade, is a cylinder with the radius 1.1R and the height 1.1R. The motivation for using two structured grids connected by an interface is to independently control the mesh resolution in the proximity of the blade and in the far field. The total number of cells is 9.8×10^6. The blade

surface mesh (see Fig. 4.3) contains 130 cells along the chord, while 210 cells are used in the spanwise direction. In order to properly resolve the boundary layer, the height of the first cell in the normal direction to the blade surface is set to 5×10^{-6} m, what ensures that Y+ is smaller than one along the whole blade. The semi-spherical outer boundary employs a boundary condi-

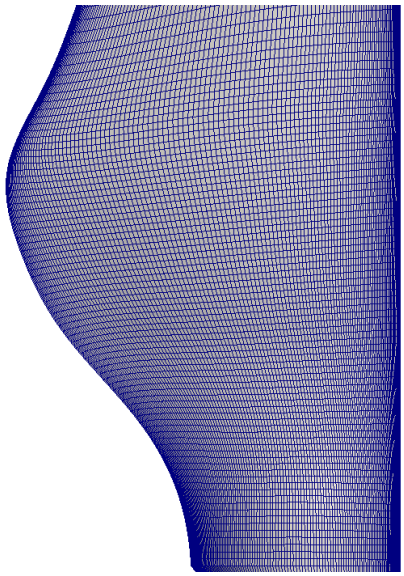

Figure 4.3: Detail of the surface mesh in the blade root region

tion that changes its behaviour depending on the direction of the flow: in regions where the flow goes in, it works like a Dirichlet boundary condition assuming a predefined value of the velocity field. In regions where the flow goes out, it enforces a zero gradient condition (Neumann condition). The symmetry plane made use of periodic boundary conditions. Non-slip boundary conditions were applied to the blade surface.

4.3 Results and discussion

4.3.1 Main characteristics of the flow field over the blades

The detailed PIV and numerical results provide a good insight into the main flow characteristics over the blade root. It is important to note that the PIV data are partly affected by (sickle-shaped) reflection artefacts in front of the leading edge. Those artefacts are easily recognizable in Fig. 4.4, 4.5 and 4.6, and they will be just neglected in the interpretation of the results.

Figure 4.4 shows the azimuthal velocity component in an inertial reference frame for the radial stations r=0.26R, r=0.35R (the position of maximum chord length) and r=0.45R. The results are normalized with the free-stream wind speed U_∞. The agreement between experimental and numerical results is excellent for all the studied radial positions. At r/R=0.35 and r/R=0.45, the azimuthal velocities are positive over the whole suction side except in the trailing edge region. However, at r=0.26R the suction side presents negative velocities from the mid-chord until the trailing edge. This does not necessarily imply flow separation and recirculation,

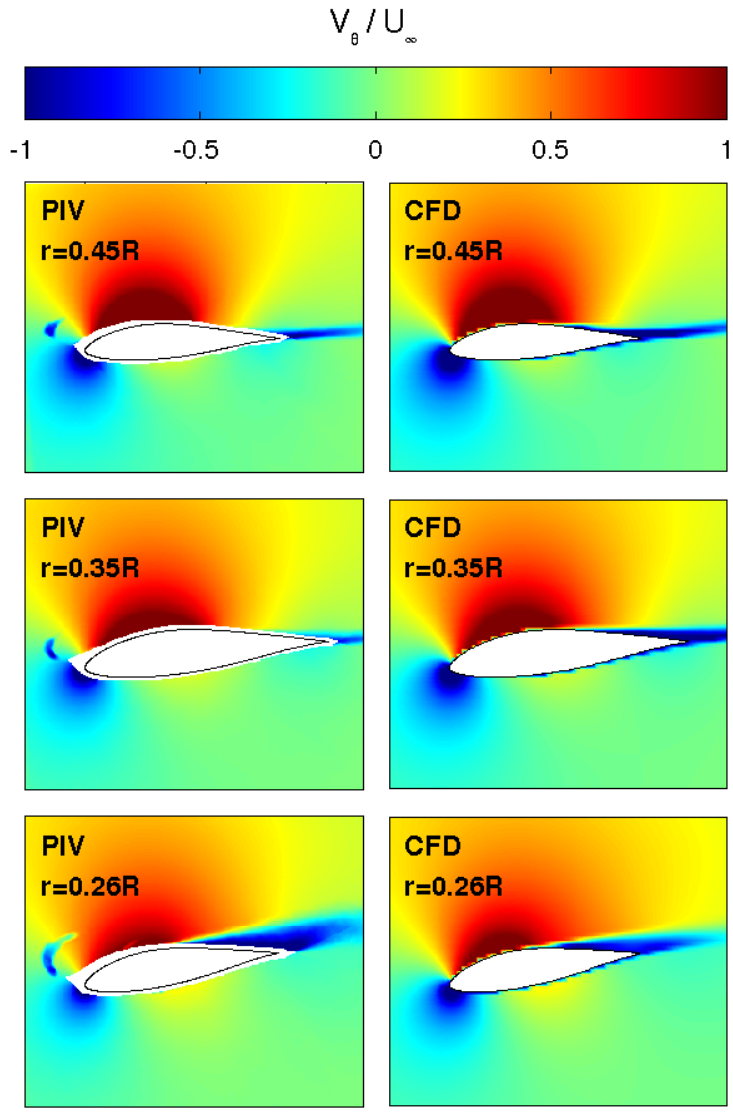

Figure 4.4: Experimental and numerical results of the azimuthal velocity component at different blade spanwise positions.

though, since the relative velocity might still remain positive along the whole suction side. Indeed, at that radial position the local circumferential velocity caused by the blade rotation is $1.82/U_\infty$, what implies that the flow remains attached up to $U_\theta = -1.82/U_\infty$. In Sect. 4.3.3 the lack of separation is demonstrated by means of the wall shear stress.

The axial flow component is shown in Fig. 4.5. The axial velocity over the second half of the suction side becomes smaller with increasing radial position. This is in fact just a geometrical effect that occurs as a consequence of the twist of the rotor blade. At r=0.45R the orientation of the second half of the suction side is slightly upstream, so the axial velocity becomes negative if the flow is attached. The effect is smaller for lower radial positions because of the larger twist

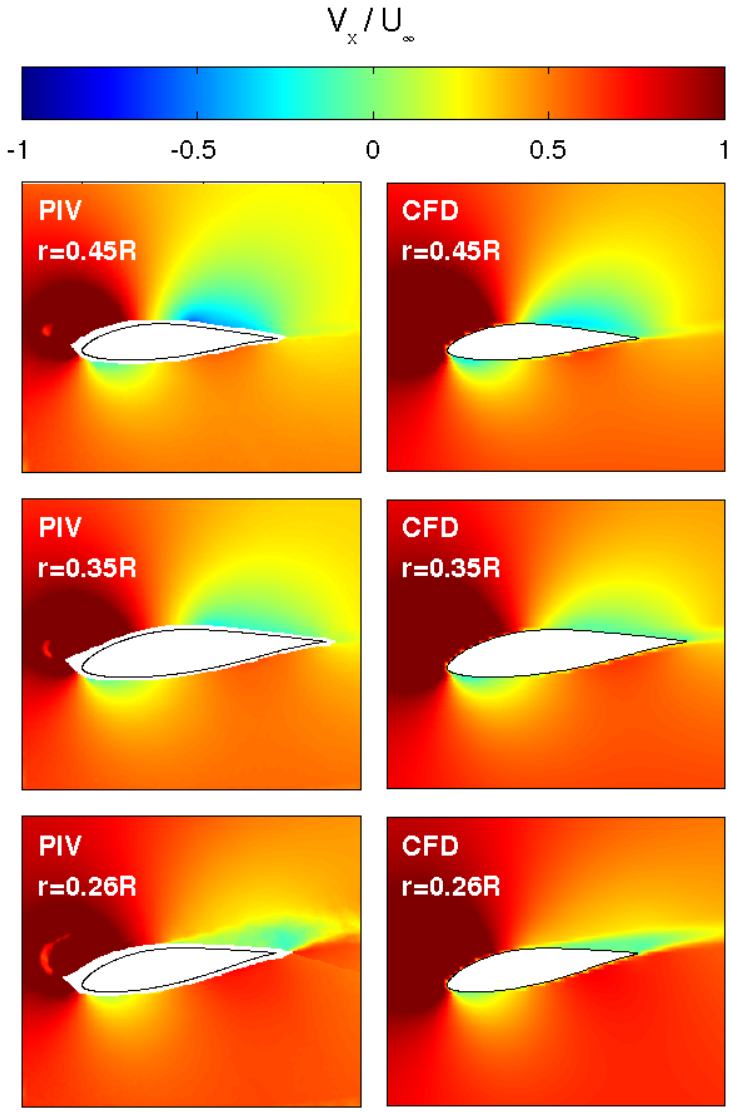

Figure 4.5: Experimental and numerical results of the axial velocity component at different blade spanwise positions.

angle, which neutralizes the mentioned geometrical effect. The numerical results are consistent with the experiments, although at r=0.45R the axial velocity over the suction side is slightly overpredicted.

Figure 4.6 displays the radial velocity component for the three considered spanwise positions. At r=0.26R, this velocity is very strong on the suction side. However, at r=0.35R and r=0.45R it becomes much weaker. Hence, the presence of spanwise flows seems to be limited to the innermost region of the blade. The agreement between experiments and simulations is again very good for all three stations.

The velocity field 10 mm off the suction side has been extracted from both the numerical

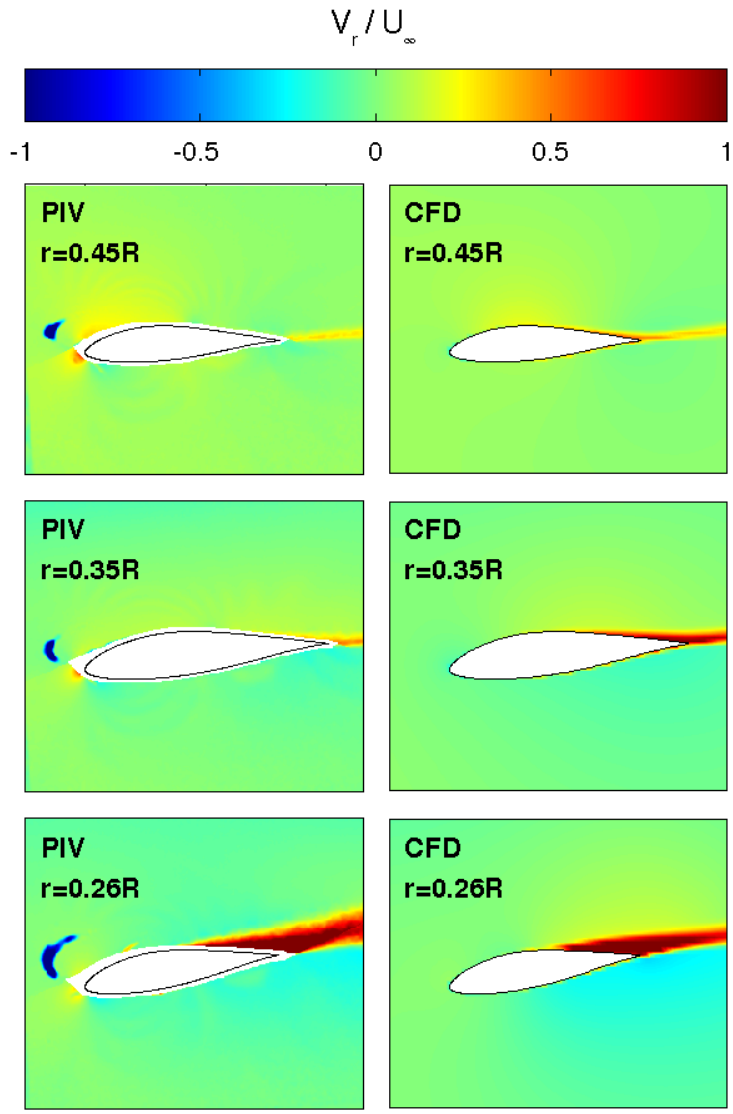

Figure 4.6: Experimental and numerical results of the radial velocity component at different blade spanwise positions.

results and the available PIV data (including 40 different radial positions between r=0.17R and r=0.65R) in order to study the flow in the proximity of the blade surface in more detail. Fig. 4.7 shows that the azimuthal component is always positive outboard of the position of maximum chord length (r=0.35R). Below that position, a significant region of the blade presents negative azimuthal velocities close to the trailing edge. At $r \approx 0.3R$, this effect is stronger in the PIV measurements than in the numerical results. Apart from this, the numerical results are in very good agreement with the experimental results.

The axial flow velocity component is displayed in Fig. 4.8. Outboard of the radial position of maximum chord length, the axial velocity becomes negative from the mid-chord towards the

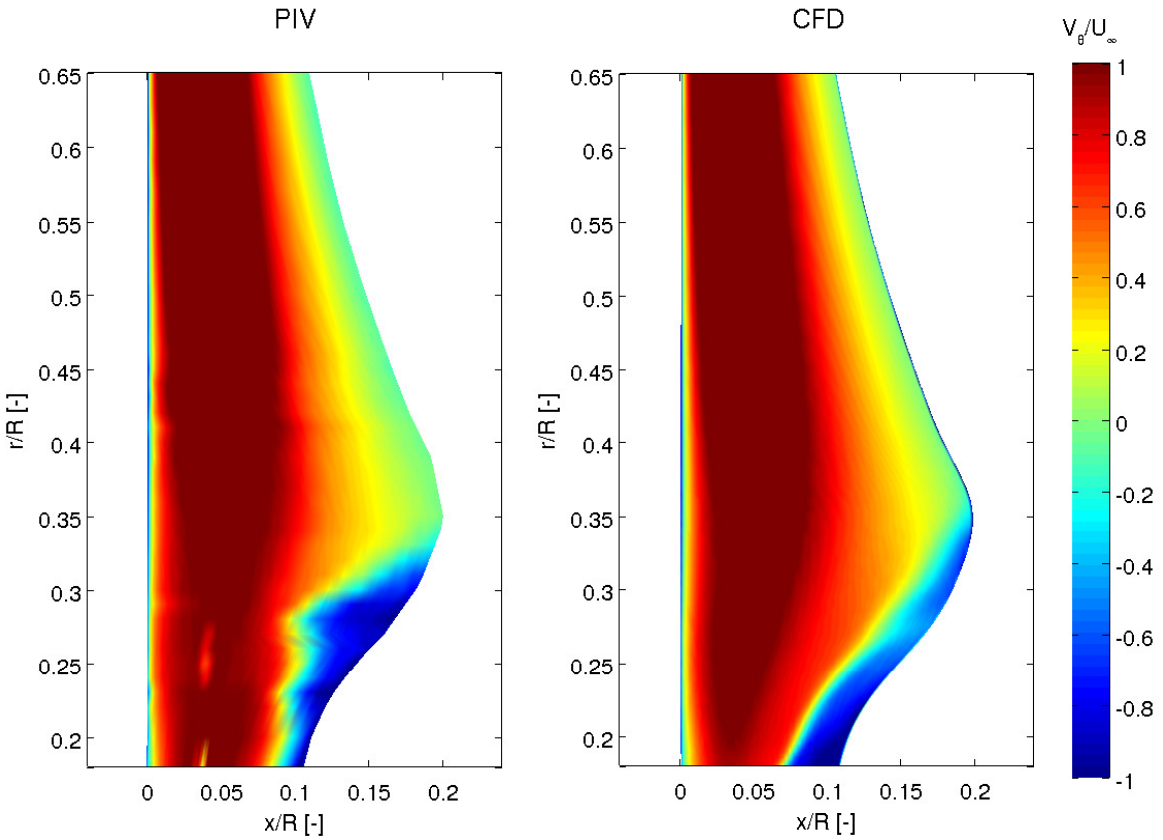

Figure 4.7: Experimental and numerical results of the azimuthal velocity component 10 mm off the blade suction side

trailing edge. The same effect was already discussed in relation to Fig. 4.5. The fact that the numerical results underpredict a bit this effect, which is caused by the relative position of the suction side to the rotor plane, might indicate a possible small deviation in the pitch angle. The agreement between PIV and CFD in the root region is very good, which is a clear indication that the wake and blade inductions are correctly predicted with the current CFD model.

Figure 4.6 presents the distribution of radial velocity along the blade suction side. The experimental results show a substantial spanwise flow in the leading edge region from r=0.45R outwards. This is rather surprising, since the flow in that region is fully attached (as shown for instance in Fig. 4.7) and it is far away from the tip and root, where spanwise flows are usually expected. The numerical results show much smaller radial velocities in that region. At present the authors do not have a solid explanation for this discrepancy. In the root region both PIV and CFD show evidence of strong spanwise flows in the proximity of the trailing edge, although the simulation tends to underpredict the spanwise flow in the region $0.3R < r < 0.35R$, as it also happened with the azimuthal velocity (Fig. 4.7). As stated earlier, this might be caused by a slight deviation of the pitch angle. Other than this, the consistency between PIV and CFD is again very good, what gives confidence in the reliability of the numerical model in predicting the complex flows of the root region.

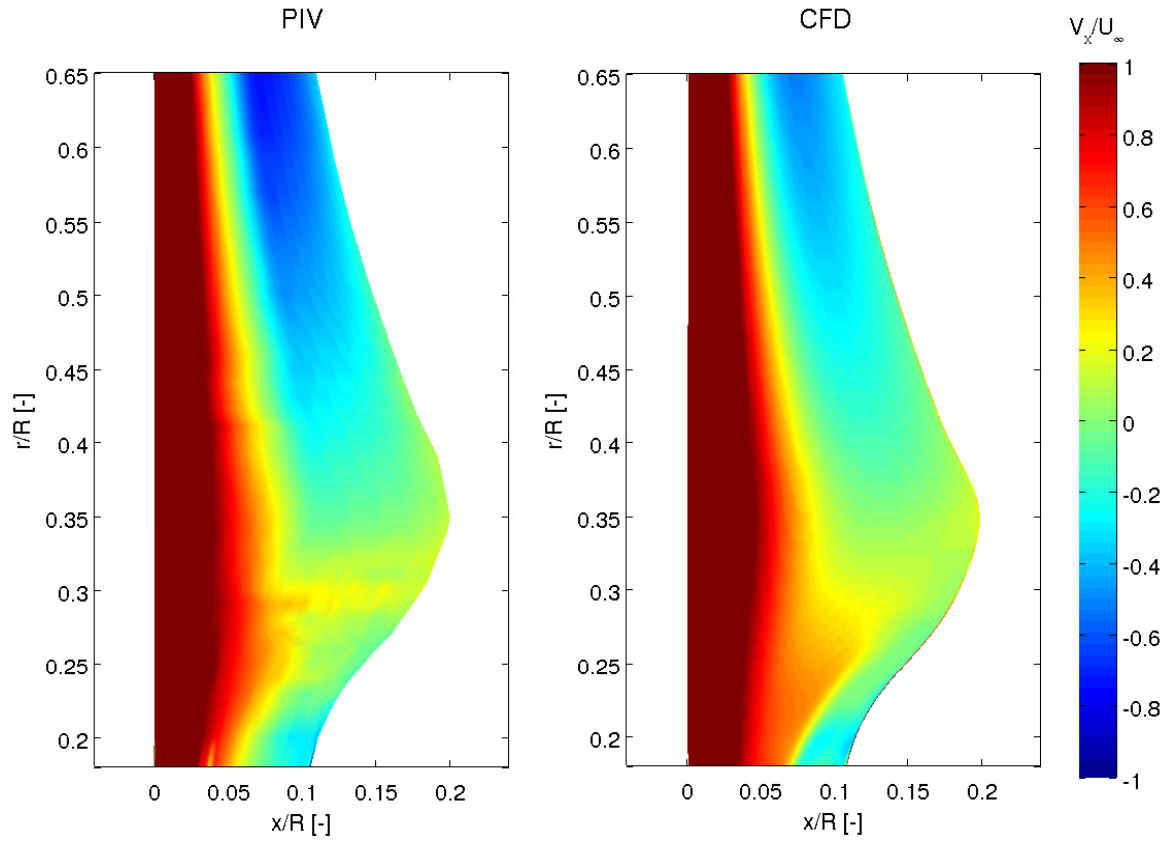

Figure 4.8: Experimental and numerical results of the axial velocity component 10 mm off the blade suction side

4.3.2 The source of the spanwise flows

Two different explanations have been proposed in the literature for explaining the origin of the spanwise flows:

1. *spanwise pressure gradients*: the dynamic pressure over the blade surface is inversely proportional to the radial position. Hence, the air is assumed to travel from the root towards outer positions as a consequence of spanwise pressure gradients (Schreck and Robinson, 2002; Schreck et al., 2010).

2. *centrifugal force*: the centrifugal force that acts on the bottom of the boundary layer (i.e. the region where the flow is not detached from the surface) pushes the flow towards the tip (Lindenburg, 2003; Guntur and Sørensen, 2014).

In order to elucidate which is the actual source of the spanwise flows, the computed isobars of the blade suction side are compared with the limiting streamlines (obtained from the wall shear stress) in Fig. 4.10. As it can be seen, the surface pressure does not present significant spanwise gradients. It is worth remarking that the same observation was made in the analysis

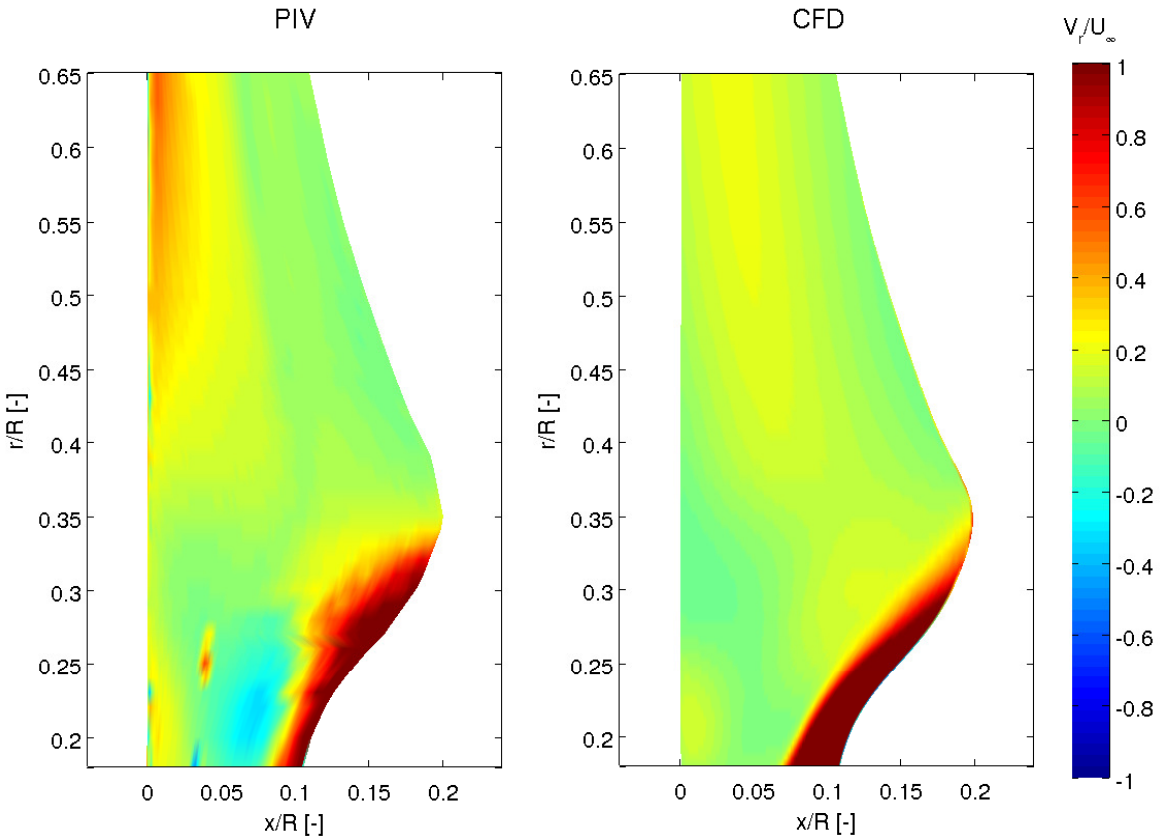

Figure 4.9: Experimental and numerical results of radial velocity component 10 mm off the blade suction side

of the MEXICO wind tunnel experiment (Herráez et al., 2014). Therefore, we conclude that the centrifugal force is the main source of spanwise flows.

Figure 4.10 also shows how the Coriolis force progressively redirects the spanwise flow coming from the root towards the trailing edge, what makes the flow to follow a curved trajectory.

4.3.3 Onset of the Himmelskamp effect

Figure 4.11 compares the pressure coefficient C_p distribution obtained from the blade at r=0.26R with the C_p distribution extracted from a 2D simulation at the same Reynolds number ($Re \approx 1 \times 10^5$) and same angle of attack (AoA$\approx 13^\circ$, computed using the method proposed by Shen et al., 2009). The 2D simulation is a RANS computation performed with the $k-\omega$ SST turbulence model. Also, the 2D mesh is equivalent to the 3D mesh except for the third dimension. Experimental results of the same 2D airfoil with $Re = 1 \times 10^6$ are displayed as well. The 2D experimental and numerical results present some disparity in the region of the suction peak, but apart from this they are very similar in spite of the difference of Reynolds number. However, the 3D results exhibit some important differences. The slope of the adverse pressure gradient is

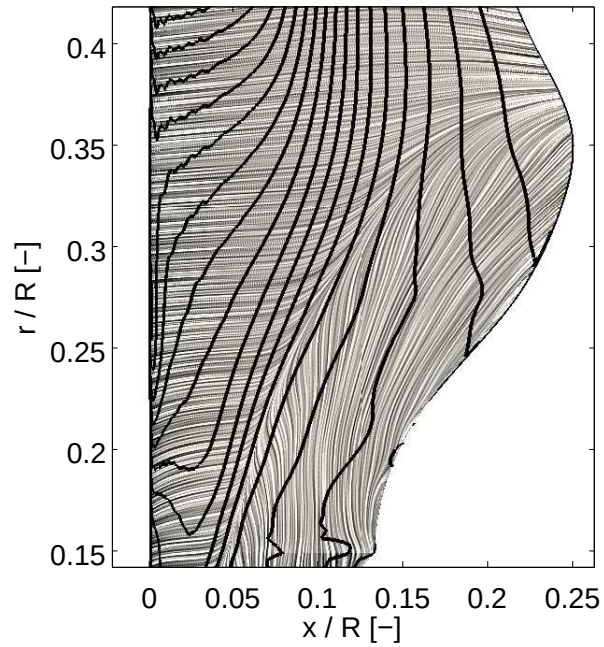

Figure 4.10: Isobars and limiting streamlines over the suction side of the blade root region.

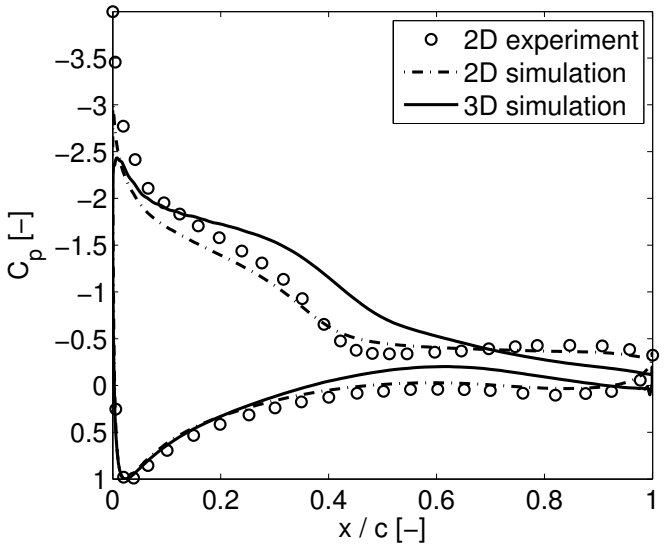

Figure 4.11: Cp distributions at AoA$\approx 13^\circ$. The corresponding Reynolds numbers are $Re \approx 1 \times 10^6$ for the 2D experimental results, $Re \approx 1 \times 10^5$ for the simulated 2D airfoil and $Re \approx 1 \times 10^5$ for the 3D blade (r=0.26R).

substantially reduced, what leads to a delay of the separation point. The separation point can be approximately identified as the point where the adverse pressure gradient meets the region with zero pressure gradient (i.e. the region where the flow is separated). In the 2D airfoils the separation point is located at $x/c \approx 0.4$. In the 3D case, the adverse pressure gradient presents a kink at $x/c \approx 0.5$, but it stays negative for the whole chord length, what seems to indicate that the flow remains attached. However, Sicot et al. (2008) concluded that rotating blades can present separation even in regions of adverse pressure gradient. In order to verify if there is separation in the 3D case, the skin friction coefficient C_{fx} on the suction side is displayed in Fig. 4.12 for both the 2D and 3D simulations. In the 2D case, C_{fx} becomes positive at $x/c = 0.39$, indicating that the flow separates exactly at that point (in good agreement with the estimation from the C_p distribution). In the 3D case, C_{fx} becomes zero at $x/c = 0.52$, but it recovers directly afterwards, remaining always negative. This confirms that the flow stays completely attached all along the chord. The point where C_{fx} becomes zero is actually the place where the chordwise flow direction is deflected into a spanwise flow direction. The same happens for all other radial positions at the root. Therefore, the transition between the chordwise and spanwise flows in Fig. 4.10 can be considered as an isoline of $C_{fx} = 0$.

Another remarkable feature of the 3D C_p distribution from Fig. 4.11 is that both the pressure and suction sides present approximately the same slope shortly after the kink in the adverse pressure gradient ($x/c \approx 0.5$) until the trailing edge. This resembles the behaviour of the 2D case in the region with zero pressure gradient. Finally, it is worth highlighting that the 3D case presents a smaller suction peak than the 2D case.

The resulting lift and drag coefficients (C_l and C_d, respectively) for the 2D and 3D cases are presented in Table 4.2. C_l is increased by approximately 9% as a consequence of the Himmelskamp effect, whereas C_d does not seem to be influenced at all. This is also in agreement with our observations from the MEXICO turbine, where the Himmelskamp effect had a very limited influence on the drag (Herráez et al., 2014).

Table 4.2: C_l and C_d for the simulated 2D airfoil and 3D blade at r=0.26R, AoA$\approx 13^\circ$

	Cl	Cd
2D	0.97	0.07
3D	1.06	0.07

4.3.4 The origin of the root vortex

The bound vorticity γ can be computed as the difference in the velocity outside the boundary layer of the pressure and suction sides. γ can then be decomposed into a radial γ_{radial} and a chordwise $\gamma_{chordwise}$ component. Figure 4.13 shows both components side by side.

γ_{radial} is concentrated around the $1/4$ chord position, as might be expected. The radial circulation Γ_{radial} can be computed from γ_{radial} as its integral along the chord: where ρ is the air density and U_{rel} is the relative velocity in the plane perpendicular to the blade axis. Owing to the γ_{radial} distribution from Fig. 4.13 and the strong link between γ_{radial} and the lift, it can be concluded that the lift force is generated almost exclusively in the first half of the chord all along the blade. The decay of γ_{radial}, and hence the decay of the lift force, is much more sudden at the

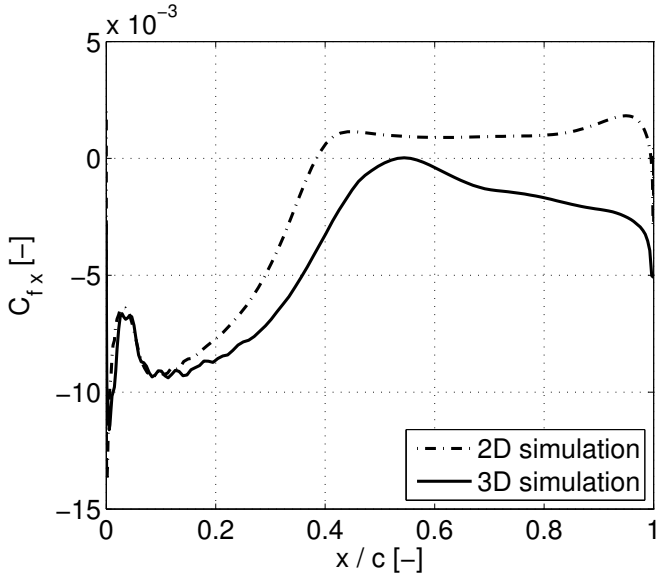

Figure 4.12: Wall shear stress in the chordwise direction over the suction side for the 2D and 3D ($r/R = 0.26$) cases.

tip than at the root. As a consequence, the root losses take place much more gradually than the tip losses. This should be taken into account by the correction models used e.g. in the BEM and actuator line methods. γ_{radial} is transformed into $\gamma_{chordwise}$ at the tip and root before becoming trailed free vorticity, what gives rise to the tip and root vortices. This is evidenced in Fig. 4.13-b, where it can be seen that the tip and root regions present substantial $\gamma_{chordwise}$ in the proximity of the trailing edge. $\gamma_{chordwise}$ is distributed over a larger spanwise range at the root than at the tip, what is in agreement with the gradual root losses earlier described. Van Kuik et al. (2014) obtained very similar results at the tip of a different rotor but the root was not studied. In the innermost region of the blade the sign of $\gamma_{chordwise}$ at the trailing edge is opposite to that of the tip (as one would expect from a horseshoe vortex model). However, in the region of maximum chord length, $\gamma_{chordwise}$ at the trailing edge presents the same sign as the tip vortex. The negative $\gamma_{chordwise}$ at the root implies an outward motion of the flow over the part of the suction side where the azimuthal velocity is slow (see Fig. 4.7). On the contrary, the positive $\gamma_{chordwise}$ in the region of maximum chord leads to an inward flow motion. Akay et al. (2014) studied the wake of the same wind turbine with PIV and indeed observed the presence of an outward flow for $r < 0.25R$ and the existence of an inward flow in the radial range $0.25R < r < 0.35R$. Furthermore, Medici and Alfredsson (2006) did similar observations in their experimental wake study of a different wind turbine. The present results not only confirm the mentioned experimental observations, but also explain the origin of this aerodynamic behaviour.

Figure 4.14 shows the bound vorticity vectors over the blade. From this figure it is evident how the direction of the bound vorticity γ changes at the root. As it can be seen, at the most inboard part of the blade ($r < 0.35R$), $\gamma_{chordwise}$ dominates the flow over the second half of the chord, indicating that vorticity is trailed along that region.

The fact that $\gamma_{chordwise}$ is distributed over such a large area of the root might explain that

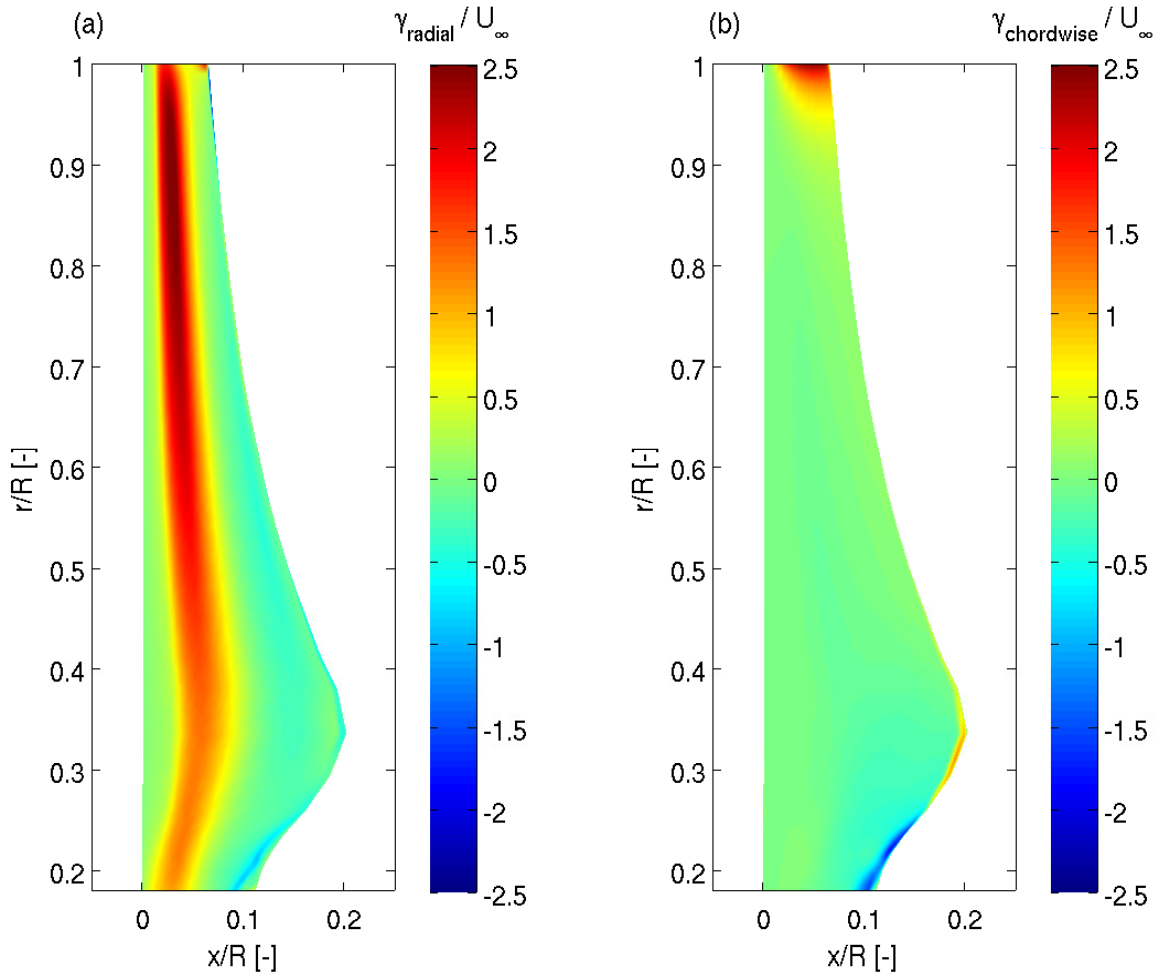

Figure 4.13: Radial and chordwise components of the bound vorticity

the root vortex does not present a well defined, distinctive structure, as Vermeer et al. (2003), Massouh and Dobrev (2007) and Haans et al. (2008) reported in their experimental wake studies of different wind turbines. Furthermore, the existence of two adjacent root regions with counter-rotating $\gamma_{chordwise}$ might also explain the fast diffusion of the root vortex reported by Ebert and Wood (2001) and Sherry et al. (2013).

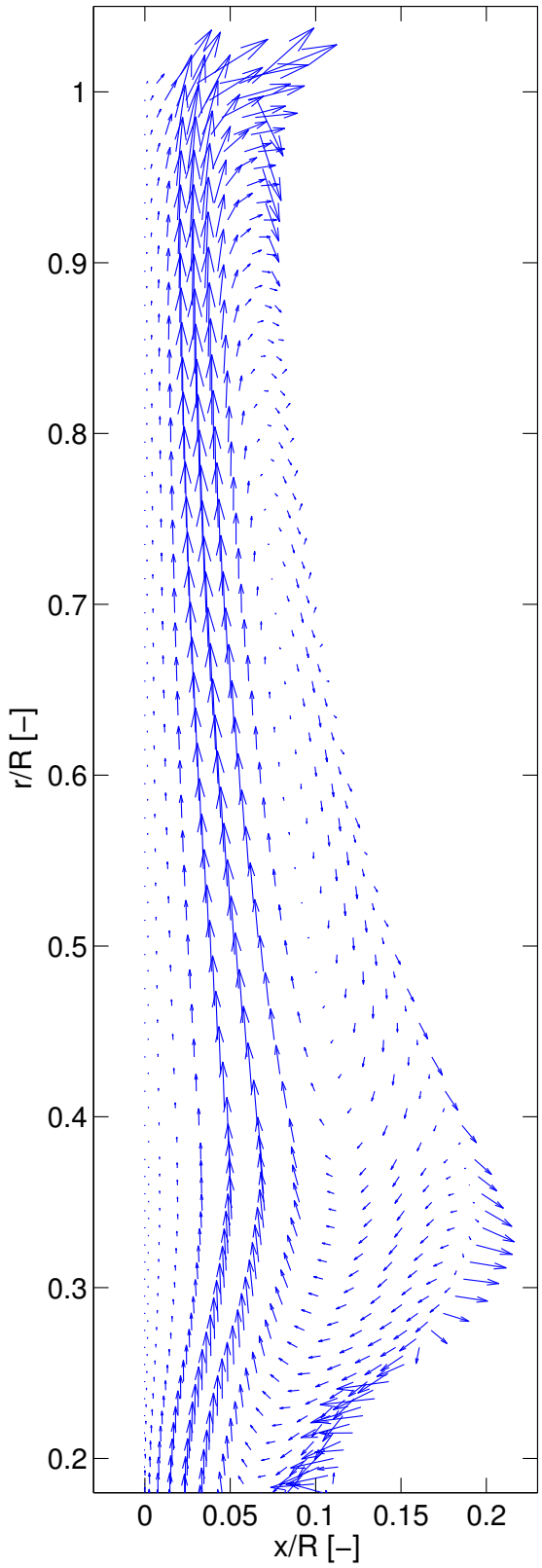

Figure 4.14: Bound vorticity vectors over the blade

4.4 Conclusions

The use of Particle Image Velocimetry (PIV) measurements and Reynolds-Averaged Navier-Stokes (RANS) simulations enabled the analysis of the flow in the root region of a wind turbine blade operating at design conditions with axisymmetric inflow. The following conclusions are drawn:

- The RANS method is capable of capturing accurately the main features of the root flow of wind turbine blades operating at design conditions.
- The spanwise flows in the root region are caused by the centrifugal force and not by radial pressure gradients, as some authors have suggested.
- Even at relatively moderate angles of attack (AoA $\approx 13^{\circ}$), the interaction of the centrifugal and Coriolis forces can give rise to the Himmelskamp effect.
- The influence of the Himmelskamp effect on the sectional C_p distribution is twofold: on one hand the suction peak is reduced, on the other hand the separation point is delayed (indeed in our case the separation is completely avoided). As a consequence of both counteracting effects, the influence of the Himmelskamp effect on the loads is weaker than in the C_p distribution.
- The reduction of the aerodynamic performance is more gradual at the root than at the tip. Tip/root loss correction models (as used e.g. in BEM simulations) should account for this effect.
- The trailing vorticity in the spanwise position of maximum chord length presents the opposite sign than at the blade root. This contributes to the diffusion of the root vortex.

We recommend to consider these points for a better characterization of the root flow of wind turbine blades. This can help to reduce the uncertainty of the blade design process, what in turn would contribute to make the turbines more cost-effective.

Chapter 5

Insight into the role of 3D rotational effects[1]

Abstract Rotational effects are known to influence severely the aerodynamic performance of the inboard region of rotor blades. The underlying physical mechanisms are however far from being well understood. The present work addresses this problem using Reynolds Averaged Navier-Stokes computations and experimental results of the MEXICO rotor. Four axisymmetric inflow cases with wind speeds ranging from pre-stall to post-stall conditions are computed and compared with pressure and PIV experimental data, obtaining in general consistent results. At low angles of attack, the aerodynamic behaviour of all the studied blade sections resembles the one from the corresponding 2D airfoils. However, at high angles of attack rotational effects lead to stall delay and/or lift enhancement at inboard positions. Such effects are shown to occur only in the presence of significant radial flows. Interestingly, the way in which rotational effects influence the aerodynamics of the MEXICO blades differs qualitatively in certain aspects from the descriptions found in the literature about this topic. The presented results provide new insights that are useful for the development of advanced and physically-sound correction models.

5.1 Introduction

The ever increasing size of wind turbine rotor blades requires accurate and efficient methods for the prediction of the aerodynamic loads and performance. Without a deep understanding of the flow phenomena governing the rotor aerodynamics, high levels of uncertainty must be expected within the design process, implying a reduction in cost-effectiveness and reliability of the whole machine. Numerous difficulties have been identified in modelling the aerodynamics of rotor blades (Leishman, 2002). Even stationary axial inflow conditions lead to complex flow phenomena, which are not yet well understood. Flow separation, secondary flows and stall delay are examples of such interrelated phenomena, which furthermore are known to play a key role in the aerodynamic behaviour of the rotor. Those effects, being highly three-dimensional (3D), limit substantially the applicability of two-dimensional (2D) airfoil polars for their use in

[1]Published as I. HERRÁEZ, B. STOEVENSADT and J. PEINKE: Insight into Rotational Effects on a Wind Turbine Blade using Navier-Stokes Computations, *Energies*, **7**, 6798–6822, 2014.

the design process. Therefore, 2D polars need to be corrected for rotational effects before using them in aeroelastic codes and other design tools.

Simms et al. (2001) reported the results of a blind test comparison in which different aerodynamic models were used for simulating the NREL Unsteady Aerodynamics Experiment (UAE) Phase VI turbine. The computed results, which were obtained with numerical tools ranging from Blade Element Momentum (BEM) theory to wake and Computational Fluid Dynamics (CFD) codes, showed a great level of uncertainty. The discrepancies observed between experiments and computations were attributed to the difficulty of predicting correctly the effect of rotation on rotor blades. This highlights the importance of improving the correction models for rotational effects and at the same time it stresses the necessity of gaining a deeper understanding of the underlying physical mechanisms.

The study of rotational effects dates back to the mid-20^{th} century. Himmelskamp (1947) studied experimentally rotational effects on aircraft propellers and observed lift enhancement and stall delay in rotating blades as compared to non-rotating blades. Banks and Gadd (1963) performed a theoretical analysis for steady boundary layers and inferred that rotation helps to delay stall, especially in the blade root region. McCroskey and Yaggy (1968) showed that crossflows contribute to the delay of separation on rotating helicopter blades. A rotating and a non-rotating wind turbine blade were compared experimentally by Ronsten (1992), concluding that rotational effects were significant only in the proximity of the hub. Wood (1991) described stall delay in terms of pressure changes to the external inviscid flow and observed that it depends on the local solidity of the blades. The use of 3D steady momentum integral boundary layer equations allowed Du and Selig (2000) to discern the importance of the Reynolds number for rotational effects on a wind turbine, deducing that for large wind turbines rotational effects would be of less importance than for small turbines. Schreck and Robinson (2002) investigated surface pressure measurements from the NREL UAE Phase VI experiment and observed that rotational augmentation is connected to radial surface pressure gradients. Tangler (2004) also studied the experimental data from the same wind turbine and highlighted the importance of the trailing vorticity and rotational effects for the aerodynamic performance. An experimental work by Sicot et al. (2008) on a small wind turbine, compared sectional surface pressure distributions from a rotating and a non-rotating blade operating in turbulent flow. The root region of the blade presented enhanced lift, but no evidence of stall delay was observed.

CFD simulations have also been commonly used since the last 15 years for the analysis of rotor aerodynamics. Different types of simulation codes have been validated against measurements since then. Duque et al. (1999) and Duque et al. (2003) obtained reasonable results (specially at attached flow conditions) simulating the NREL Combined Experiment Phase II and the NREL UAE Phase VI turbines with a RANS unsteady compressible code that made use of overset grids and the Baldwin-Lomax algebraic turbulence model. Le Pape and Lecanu (2004) used another unsteady compressible RANS code with the $k\omega$ and the $k\omega - SST$ turbulence models for simulating the NREL Phase VI turbine. The best results were obtained with the $k\omega - SST$ model, but the predictions at stall conditions were rather inaccurate with both models. Johansen et al. (2002) used Detached-Eddy Simulations based on the $k\omega - SST$ turbulence model for predicting the flow around the NREL Phase VI turbine under parked conditions with fixed pitch as well as with oscillating pitch. The DES results presented more three-dimensional flow structures than RANS simulations, but the global blade characteristics were not better predicted. Johansen and Sørensen (2004) simulated 3 different wind turbines with RANS using the

$k\omega - SST$ model and one turbine using DES. The authors highlighted the challenges associated to the prediction of highly separated rotor flows.Sørensen and Schreck (2012) obtained good results of the flow field upstream and downstream of the MEXICO turbine in axial and yawed conditions using the $k\omega$ turbulence model.
In general, most CFD codes obtained better results simulating the NREL UAE Phase VI turbine than the MEXICO turbine. Sørensen et al. (2002) explained that the NREL turbine was comparatively well suited for the computation with the RANS method because its blades are designed with the S809 airfoil, for which good results at high angles of attack (*AoA*) are obtained also with 2D simulations. Furthermore that airfoil type is apparently rather insensitive to the vortex interaction in the wake, what facilitates its prediction with RANS. The authors also studied rotational effects in that wind turbine, concluding that the enhancement of the aerodynamic forces at inboard radial positions was attributed to radial pumping of the separated flow in the inboard blade region. In a later work, Schreck et al. (2007) studied the same turbine using RANS with the $k\omega - SST$ turbulence model and ascribed the rotational effects to stationary vortical structures located on the upper blade surface. Very recently, Guntur and Sørensen (2014) studied the MEXICO turbine with RANS and the $k\omega$ model, observing that on rotating blades there is a postponement of the separation point. Furthermore it was concluded that the *AoA* at which separation is initiated is higher in 3D compared with 2D.

The knowledge gained from measurements, theoretical works and numerical computations has been used by several authors for developing correction models for 2D polars (Snel et al., 1993; Chaviaropoulos and Hansen, 2000; Raj, 2000; Bak et al., 2006; Lindenburg, 2003; Corrigan and Schillings, 1994; Tangler and Selig, 1997; Du and Selig, 1998). Breton *et al.* Breton et al. (2008) compared six different correction models for rotational effects using a lifting-line prescribed wake vortex code for simulating the NREL UAE phase VI turbine. None of the models was able to predict the measured data satisfactorily and the loads under stall conditions were generally overestimated. Guntur *et al.* Guntur et al. (2011) performed a similar test with experimental data from the MEXICO wind turbine, using an inverse BEM method for determining the *AoA*. Again, none of the correction models was successful at predicting the 3D aerodynamic characteristics.

As shown, current knowledge about rotational effects is still incomplete and requires further investigation if rotor blades are to be designed in a more reliable and cost-effective way.

The present work addresses this problem using a CFD model of the MEXICO wind turbine in conjunction with experimental data. The existence of rotational effects is verified by comparing 2D and 3D airfoil polars. Then, 2D and 3D C_p distributions are analysed for ascertaining the mechanisms that lead to an augmentation of the lift force at inboard positions. A deeper insight into the sources of the rotational effects is gained through the study of distinctive flow features in the near wake and the boundary layer of the rotor blades. The knowledge gained from these analyses is compared throughout the paper with the findings from other studies and the assumptions from well-known correction models. This provides important information for the development of improved and physically-sound correction models.

5.2 Methods

5.2.1 The MEXICO Experiment

The EU FP5 MEXICO (Model EXperiments In COntrolled COnditions) project involved the extensive measuring of loads, surface pressure and flow field data of a three bladed 4.5 m rotor diameter wind turbine placed in the Large Low-Speed Facility of the German-Dutch Wind tunnel DNW, which has an open Section of 9.5 x 9.5 m^2 (Schepers and Snel, 2007). The blockage ratio was 18% but the use of breathing slots behind the collector helped to reduce tunnel effects. Réthoré et al. (2011) and Shen et al. (2012) showed that tunnel effects have very limited influence on the rotor flow.

The design of the blades was based on 3 different aerodynamic profiles, as shown in Table 5.1.

Table 5.1: Airfoil type distribution along the span of the MEXICO blade

Radial position $[r/R]$	Airfoil type
0.09-0.17	Cylinder
0.17-0.20	Transition
0.20-0.50	DU91-W2-250
0.50-0.54	Transition
0.54-0.70	RISØ-A1-21
0.70-0.74	Transition
0.74-1.00	NACA 64-418

The blades were twisted and tapered, and a zig-zag tape at 5% of the chord was used both on the blade upper and lower surfaces to trigger the laminar to turbulent transition.

The tower was located 2.13 m downwind from the rotor and its diameter was only 0.5 m, so its influence on the rotor flow is believed to be negligible (Bechmann et al., 2011; Shen et al., 2012). The measurements were performed under different inflow conditions. In this work four wind speeds have been considered, namely 10, 15, 19 and 24 m/s. The rotational speed and the pitch angle were kept constant at 424.4 rpm and -2.3°, respectively. Only axial inflow conditions are considered in order to isolate the rotational effects from other influences like dynamic stall.

The pressure measurements were performed by means of pressure transducers placed at five different blade sections corresponding to the blade span positions 0.25R, 0.35R, 0.60R, 0.82R and 0.92R. Multiple PIV windows upstream and downstream of the turbine were used for measuring the flow field. Furthermore, the loads on the tower bottom were measured by means of a balance.

The tip speed was 100 m/s for all cases, meaning a tip speed ratio of 6.7 at design conditions (U_∞=15 m/s). The Mach number did not exceed 0.3, and compressibility effects are consequently disregarded in this work.

Table 5.2 shows the chord-based Reynolds and Rossby numbers of the MEXICO turbine at different radial positions. For comparison with a large turbine, the same parameters corresponding to the NREL 5 MW wind turbine (Jonkman et al., 2009) are shown. In both cases,

rated operating conditions have been assumed. The Reynolds number in the MEXICO turbine is one order of magnitude smaller than in the NREL 5 MW turbine, indicating that the viscous forces play a substantially stronger role in the MEXICO turbine. However, the Rossby number is similar for both machines (on average it is just about 17% smaller in the MEXICO turbine), what implies that the effect of rotation in both cases is probably comparable. Furthermore, the Rossby number decreases towards the blade root, what in turn means that the influence of the Coriolis force in that blade region is stronger.

Table 5.2: Reynolds and Rossby numbers for the MEXICO (subscript MX) and the NREL 5 MW (subscript NREL) wind turbines at different radial positions.

r/R	Re_{MX}	Ro_{MX}	Re_{NREL}	Ro_{NREL}
0.25	4.3×10^5	2.9	7.0×10^6	3.9
0.50	5.5×10^5	7.4	1.0×10^7	8.7
0.75	6.2×10^5	14.1	1.2×10^7	15.8
0.90	6.2×10^5	20.1	1.2×10^7	23.3

The MEXICO data set (Boorsma and Schepers, 2003) also includes wind tunnel measurements of the 2D airfoils shown in Table 5.1. The Reynolds numbers from the 2D experiments are approximately in the range corresponding to the blades. Furthermore, the 2D airfoils were fitted with a zig-zag tape in the same fashion like the blades for triggering the transition from laminar to turbulent flow. The 2D experiments include both lift and drag characteristics as well as C_p distributions (except for the RISØ-A1-21 airfoil, for which only aerodynamic force coefficients are available).

It would be very useful to count with blade section characteristics obtained from parked rotor experiments in order to isolate rotational effects from possible 3D effects caused by the blade geometry. Such experiments were also carried out within the MEXICO project, but the corresponding measurement results are unfortunately not reliable because of malfunctioning pressure sensors (Pascal, 2009). However, the main differences between 2D and 3D results are known to occur in the post-stall range, especially in the inboard region, where rotational effects clearly dominate over other influences (Sicot et al., 2008; Schreck et al., 2007). Therefore, we assume that comparing 2D and 3D characteristics is an acceptable method for assessing the role of the rotational effects. This is also the most common way to do it (Bechmann et al., 2011; Guntur and Sørensen, 2014; Johansen and Sørensen, 2004; Le Pape and Lecanu, 2004; Sørensen et al., 2002; Tangler, 2004; Troldborg et al., 2013; Breton et al., 2008; Guntur et al., 2011).

Further details about the experimental set-up can be found in Boorsma and Schepers (2003).

5.2.2 Numerical method and computational mesh

The numerical results presented in this work have been obtained from incompressible steady state Reynolds Averaged Navier-Stokes (RANS) simulations performed with the open source software OpenFOAM. OpenFOAM is a computational framework for numerical simulations of partial differential equations. The rotation of the system was accomplished using a non-inertial

reference frame and adding the Coriolis and centrifugal forces to the momentum equations. The SIMPLE algorithm was employed for the pressure-velocity coupling. The convective terms were discretized with a second order linear-upwind scheme. The discretization of the viscous terms was achieved by means of a second order central-differences linear scheme. The spatial discretization was performed with the finite volume method. No time discretization was used since only steady-state simulations were performed. The simulations were run fully turbulent and made use of the Spalart and Allmaras (1994) turbulence model. The use of a so called *adaptive* (also known as *continuous*) wall function allowed to maintain a comparatively low number of cells without compromising the accuracy of the simulations under separated flow conditions. The way in which the adaptive wall function works is simple: it switches automatically between a low-Re and a high-Re computation approach in dependence of the local Y+ value. In regions where the first grid point is within the viscous sublayer (small Y+), the low-Re approach is followed and the boundary layer is completely resolved. In areas where the first grid point is in the log-law region (high Y+), a wall function is used. A blending function is also implemented for the cases where the first grid point is within the buffer layer, i.e. between the viscous sublayer and the log-law region. When the flow is separated or close to the separation point, the flow velocity becomes very low, what implies that Y+ will be also very small. The boundary layer will be then fully resolved instead of modelled with a wall function. This is a substantial enhancement as compared to standard wall functions, since it allows a satisfactory prediction of complex flow conditions including stall (Spalding, 1961; Rung et al., 2001; de Villiers, 2006; Mockett, 2009; Schmidt et al., 2009).

In OpenFoam the velocity-pressure coupling is based on a collocated grid approach (both the velocity and the pressure are solved at the centre of the control volumes). This implies that both the velocity and the pressure conditions have to be defined at all boundaries. At the inlet, the wind speed was specified and the pressure was set to zero gradient. On the contrary, at the outlet the pressure was predefined and the velocity was set to zero gradient. Non-slip boundary conditions were set for the blades and the nacelle.

The parallelization of the simulations was accomplished by means of the Message Passing Interface (MPI).

The iterative convergence was ensured by achieving at least three orders of magnitude reduction in the residuals of each field variable. Furthermore, in order to guarantee that the numerical results are grid independent, a grid convergence study was performed prior to carrying out the simulations presented in this paper. The study was based on the Grid Convergence Index (GCI) method developed by Roache (Roache, 1994, 1998a), which is used for quantifying the numerical uncertainty. For this, the MEXICO rotor was simulated at design conditions (i.e. 15 m/s and axisymmetric flow) with three different meshes. After generating a coarse mesh (5.8×10^6 cells), it was systematically refined for creating the medium (8.5×10^6 cells) and fine (11.3×10^6 cells) meshes.

Table 5.3 summarizes the results of the study for the key variables torque and thrust. ϕ represents the corresponding key variable, whereas e_{ext} and GCI represent the extrapolated relative error and the numerical uncertainty, respectively, both referred to the fine grid. The low uncertainty level obtained for both the torque and the thrust (0.42% and 0.55%, respectively) is a clear indicator, that the results with the fine mesh are grid independent. That mesh was therefore used for all the simulations presented in this paper.

The mesh exploited the 120-degrees symmetry of the wind turbine rotor by modelling only

Table 5.3: Results of the grid convergence study

	ϕ=Torque	ϕ=Thrust
ϕ_{fine}	101.97 Nm	569.97 N
ϕ_{medium}	102.03 Nm	570.40 N
ϕ_{coarse}	102.25 Nm	576.76 N
e_{ext}	0.34%	0.44%
GCI	0.42%	0.55%

one blade. The domain consisted of 1/3 of a cylinder and employed periodic boundary conditions in order to account for the other two blades. Its length and radius were 52 and 16 m, respectively. The mesh was of type unstructured and hex-dominant (99% of the cells were hexaedra, the rest were split hexaedra). The boundary layer of the blades and the nacelle was resolved with 5 prism-layers. The use of the adaptive wall function allowed for a y+ value on the blades between 50 and 200 under attached flow conditions, which helped to limit the number of cells. The wake and the regions where high gradients were expected, were accordingly refined.

5.3 Results and discussion

5.3.1 3D aerodynamic characteristics

As mentioned in Section 5.1, the aerodynamic characteristics extracted from rotating blades commonly present evidence of rotational effects such as stall delay and lift enhancement (especially at radial positions close to the blade root). In order to verify the existence of such effects in the MEXICO turbine, the measured and computed lift coefficient (C_l) characteristics from different blade radial positions are compared with experimental 2D C_l characteristics in Fig. 5.1. The same comparison for the drag coefficient (C_d) is shown in Fig. 5.2. Every plot in those figures shows four points for the 3D experimental results. Every point corresponds to a different wind speed (U_∞ = 10, 15, 19 and 24 m/s). Owing to the constant pitch angle and rotational speed, increasing wind speed implies increasing AoA. The full lines representing the numerical results were also obtained from the above mentioned four free-stream wind speeds.

The 3D polars have been extracted from the numerical and experimental results following the method described in Johansen and Sørensen (2004). For this, the normal force coefficient (C_n) and tangential force coefficient (C_t) have been computed from the surface pressure coefficient (C_p) distributions and then transformed into C_l and C_d after calculating the AoA. The calculation of the AoA is based on the method proposed by Hansen et al. (1997), which relies on flow field data extracted from numerical simulations, and has proven to be reliable (Johansen and Sørensen, 2004; Sørensen et al., 2002; Guntur and Sørensen, 2012). In this method, the wind speed is sampled along multiple rings both upstream and downstream of the rotor. The radius of the rings corresponds to the spanwise positions for which the AoA should be obtained. Then, the average velocity for each ring is calculated. Afterwards, the velocity in the rotor plane for each radius is computed by interpolating along the axial direction the mean velocities ob-

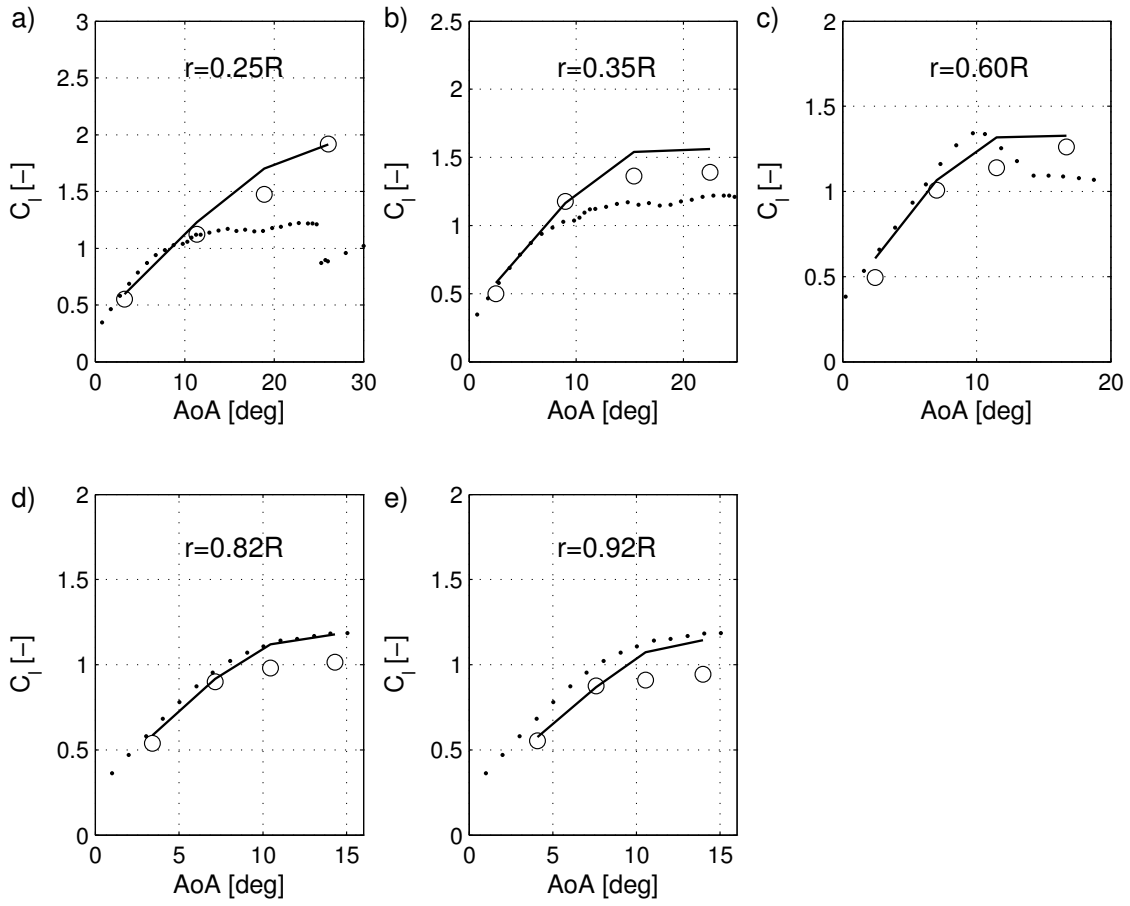

Figure 5.1: Comparison of C_l characteristics at five different spanwise positions. The dotted lines represent 2D experimental results, the circles indicate 3D experimental results and the full lines show 3D numerical results.

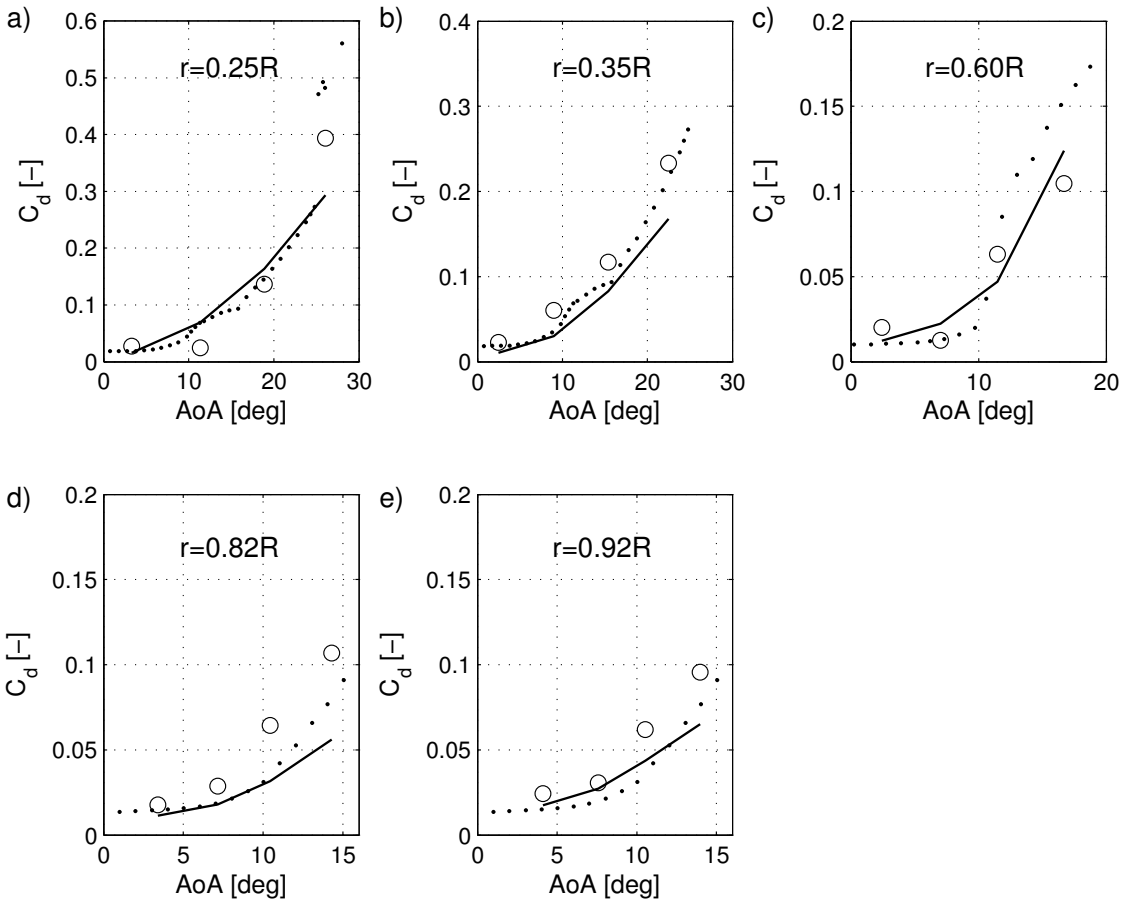

Figure 5.2: Comparison of C_d characteristics at 5 different spanwise positions. The dotted lines represent 2D experimental results, the circles indicate 3D experimental results and the full lines show 3D numerical results.

tained in the previous step. Finally, the effective angle of attack is estimated with the following equation:

$$AoA = \arctan\left(\frac{U_{rotor}}{r\omega}\right) - \phi, \tag{5.1}$$

where, U_{rotor} is the axial wind speed in the rotor plane, ω is the rotational speed, r is the local radius and ϕ is the local angle between the chord of the blade section and the rotor plane, considering both the pitch and the twist angles.

3D C_l characteristics

In the proximity of the blade root, i.e. at $r = 0.25R$ (Fig. 5.1-a), the experimental 3D C_l characteristics are almost identical to the 2D case until the 2D airfoil begins to stall (approximately at $AoA = 12°$). After having reached that angle, only the 3D C_l curve continues to rise. Indeed, that C_l curve does not present any evidence of stall for the whole range of available data, which goes until $AoA = 26°$. Taking into account that the AoA of stall onset for the 2D case is approximately 12°, the lack of stall in the 3D case implies a delay in the stall AoA of at least 14°, i.e. the stall onset is delayed by 117%. At $AoA = 26°$, the 3D C_l curve presents 115% more lift than the 2D case for the same AoA and 55% more lift than the maximum lift from the 2D case. The simulations agree quite well with the measurements and are able to predict satisfactorily the stall delay and lift enhancement.

A bit further outboard, at $r = 0.35R$ (Fig. 5.1-b), the experimental 3D C_l characteristics again resemble the 2D curve up to the 2D stall onset, although the slope of the 3D curve is slightly greater when the stall AoA is approached. At higher AoA, the 3D case presents lift enhancement as compared with the 2D curve. However, the slope of the 3D C_l characteristics becomes less steep after the 2D stall onset, meaning that rotational effects are less strong at this position than at $r = 0.25R$. In fact, the stall angle does not seem to be delayed, in spite of the maximum lift being enhanced by approximately 15%. At this radial station the numerical results are consistent with the 3D experimental results up to the 2D stall onset. For higher AoA, the simulations overpredict a bit the C_l values, although they offer a good qualitative agreement with the experiments.

In the proximity of the mid-span region, i.e. $r = 0.60R$ (Fig. 5.1-c), the experimental 2D and 3D C_l characteristics are similar until the stall onset. From the experimental results, it seems that at $AoA = 12°$, i.e. shortly after the 2D stall onset, the rotating blade produces less lift than the 2D airfoil. However, at $AoA = 17°$ (i.e. in the post-stall region), the blade maintains almost the same C_l as the maximum C_l from the 2D airfoil, indicating the existence of stall delay. Measurements and simulations present a good qualitative and quantitative agreement for the whole range of available AoA except for $AoA = 12°$, where the simulations overpredict the lift.

At $r = 0.82R$ (Fig. 5.1-d) and more markedly at $r = 0.92R$ (Fig. 5.1-e), the experimental 3D results display a lower C_l than the 2D airfoil for the whole range of AoA, although this effect is significantly stronger after the stall onset. At low AoA, the C_l reduction is attributed to the influence of the tip vortex on the local induction. At high AoA, it seems to exist an additional source of C_l reduction, which is discussed later in more detail. The simulations predict satisfactorily the linear range but overestimate C_l at high AoA. Here, it is worth to recall that other CFD investigations from the MEXICO turbine encountered the same difficulties in

the outboard region. As an example, the final report of the MexNext project (Schepers et al., 2012) shows a comparison of the C_p distributions obtained from different CFD models. At U_∞ = 24 m/s, the results for $r = 0.82R$ and $r = 0.92R$ from six different models out of seven present a good consistency between them. However, all the mentioned models overpredict the negative pressure on the attached flow region of the suction side, what implies an overestimation of C_l.

Breton et al. (2008), who used a lifting line prescribed wake vortex code for simulating the NREL UAE Phase VI turbine, documented that most correction models for rotational effects lead to an overprediction of the lift in the outermost region of the blade. Only two exceptions were identified: the model by Corrigan and Schillings (1994), who suggested not to apply any correction for rotational effects above $r = 0.75R$, and the model by Lindenburg (2003), who suggested not only not to apply any lift-enhancement correction above $r = 0.80R$, but also to introduce a special tip loss correction for accounting for radial flows above that radial position. The results from the MEXICO turbine confirm that it is a good idea to limit the enhancement of the lift force at outboard positions. The suitability of the special tip loss correction proposed by Lindenburg is discussed later in connection with the drag.

3D C_d characteristics

In opposition to the 3D C_l characteristics, the 3D C_d characteristics (Fig. 5.2) are more or less in good agreement with the 2D characteristics at $r = 0.25R$ and $r = 0.35R$ for the whole range of available AoA (even under stall conditions). The simulations are in general consistent with the experiments, except at the highest AoA, where C_d is underestimated. Furthermore, at $r = 0.35R$ the simulations tend to slightly underestimate C_d for the whole range of AoA.

At $r = 0.60R$ (Fig. 5.2-c) the experimental 3D C_d characteristics resemble again the 2D case, except at $AoA = 17^\circ$, where the 3D drag is reduced as compared with the 2D case. As it was seen in the C_l characteristics for the same radial position and AoA, rotational effects play a significant role at these conditions. The C_d reduction is therefore attributed to the mentioned effects. The numerical results are also reasonably consistent with the experiments at this station. At $AoA = 17^\circ$ the simulations overestimate C_d, though.

The way in which rotational effects influence the C_d characteristics of the MEXICO rotor blades differs from the descriptions found in the literature about this topic: as an example, in the NREL UAE Phase VI wind turbine, rotational effects were accompanied by a significant drag increase (Sørensen et al., 2002; Breton et al., 2008; Johansen and Sørensen, 2004). Additionally, Lindenburg (2003) describes rotational effects to increase the drag as a consequence of the radial flows existing in rotating blades under stall conditions, arguing that energy is required for pumping air from the root region towards outer radial positions. Furthermore, most correction models for rotational effects predict a C_d increase (Bak et al., 2006; Raj, 2000; Lindenburg, 2003), while others describe a C_d reduction (Du and Selig, 2000; Corrigan and Schillings, 1994) or no influence at all on C_d (Snel et al., 1993). Owing to the fact that in the MEXICO turbine rotational effects do not affect substantially C_d, except at $r = 0.60R$, it is not surprising that in the study by Guntur et al. (2011), who tested different correction models with the MEXICO turbine, it is concluded that correcting for C_d might be unnecessary (their study was limited to the radial stations $r = 0.25R$ and $r = 0.35R$). That conclusion, which our results confirm for the same turbine, can however not been generalized for other wind turbines (as explained above). Furthermore, the fact that in the MEXICO turbine rotational effects influence C_d at $r = 0.60R$,

but do not do it at $r = 0.25R$ and $r = 0.35R$, is an indication that such effects might be airfoil type-dependent (at $r = 0.25R$ and $r = 0.35R$, the DU91-W2-250 airfoil was used, whereas at $r = 0.60R$ the RISØ-A1-21 airfoil was utilized).

At $r = 0.82R$ as well as at $r = 0.92R$ (Fig. 5.2-d and Fig. 5.2-e, respectively), the experimental C_d from the 3D case is increased as compared with the 2D airfoil, especially at high AoA. The influence of the tip vortex and the subsequent downwash at radial positions $r < R$ imply a reduction of the AoA, what also leads to a reduction of C_l and C_d. The C_d rise observed in the MEXICO turbine indicates that other influences must be taken into account. Lindenburg (2003) suggested that the influence of the radial flows coming from inboard positions should be considered for modelling the airfoil characteristics at outboard positions. Therefore, his model for rotational effects includes a special correction for $r > 0.8R$, which is based on the idea that the spanwise flows acting on the separated volume of air can not be driven further outboard than the blade tip itself, what causes a pressure rise on the suction side of the tip region. As a consequence, he expected C_l and C_d to drop. This is in conflict with the C_d rise observed at high AoA in Fig. 5.2-d and Fig. 5.2-e, so Lindenburg's suggestion does not seem adequate for the MEXICO wind turbine.

The CFD results for $r = 0.82R$ and $r = 0.92R$ present the problem that the drag is underpredicted at high AoA. Even for 2D airfoils, the prediction of the aerodynamic loads under stall conditions is known to be a challenge for RANS computations (Bertagnolio et al., 2001), so the mismatch with the experiments are probably due to the limitations of the RANS method. These limitations for the prediction of separated flows mainly arise from two issues: First, turbulence is not resolved, but modelled. The turbulence models are usually designed and calibrated for certain applications and conditions, and they are by no means universally reliable. Complex flow situations like flow separation are certainly a major challenge for any turbulence model. Secondly, RANS is not able to resolve the unsteadiness associated to separated flows because it only provides an averaged solution, what of course can lead to poor predictions in the stall region. However, this problem is expected to be of less importance in the blade root region, where separation is known to be a rather stationary process because of the stabilizing standing vortex that characterizes stall in that part of the blade (Schreck and Robinson, 2002; Robinson et al., 1999).

However, it remains unclear why under stall conditions the experimental results for $r = 0.82R$ and $r = 0.92R$ show that the lift reduction is accompanied by a drag increase as compared with the 2D airfoil. This problem is further discussed in the Sections 5.3.3 and 5.3.4.

5.3.2 Influence of rotational effects on the C_p distributions

The 3D airfoil characteristics have shown that, under stall conditions, stall delay and/or lift enhancement influence the aerodynamic performance of the blade at the radial positions $r = 0.25R$, $r = 0.35R$ and $r = 0.60R$. In order to study in more detail the origin of those effects, the computed and measured C_p distributions of the mentioned radial positions are presented in Fig. 5.3-5.5 for $U_\infty = 24$ m/s (corresponding to the wind speed at which the strongest rotational effects occur). In Fig. 5.3 and Fig. 5.4 ($r = 0.25R$ and $r = 0.35R$, respectively), the experimental C_p distributions from the corresponding 2D airfoil (DU91-W2-250) are also shown. Unfortunately, for the station $r = 0.60R$, which uses the airfoil RISØ-A1-21, no experimental C_p distribution of the 2D airfoil is available.

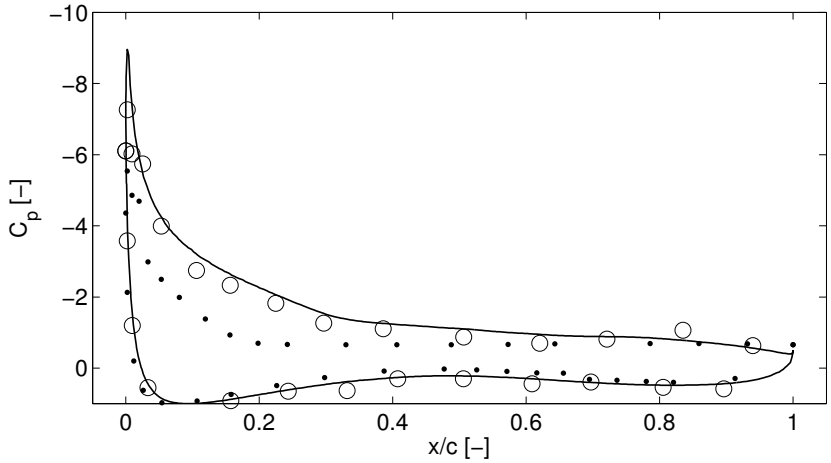

Figure 5.3: C_p distribution from $r = 0.25R$ for $U_\infty = 24m/s$, corresponding to $AoA = 26°$. The dotted line represents 2D experimental results, the circles indicate 3D experimental results and the full line shows 3D numerical results.

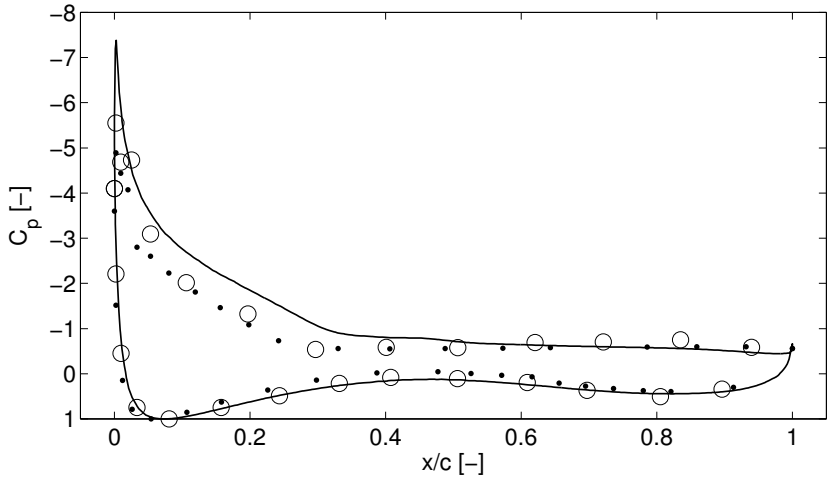

Figure 5.4: C_p distribution from $r = 0.35R$ for $U_\infty = 24m/s$, corresponding to $AoA = 23°$. The dotted line represents 2D experimental results, the circles indicate 3D experimental results and the full line shows 3D numerical results.

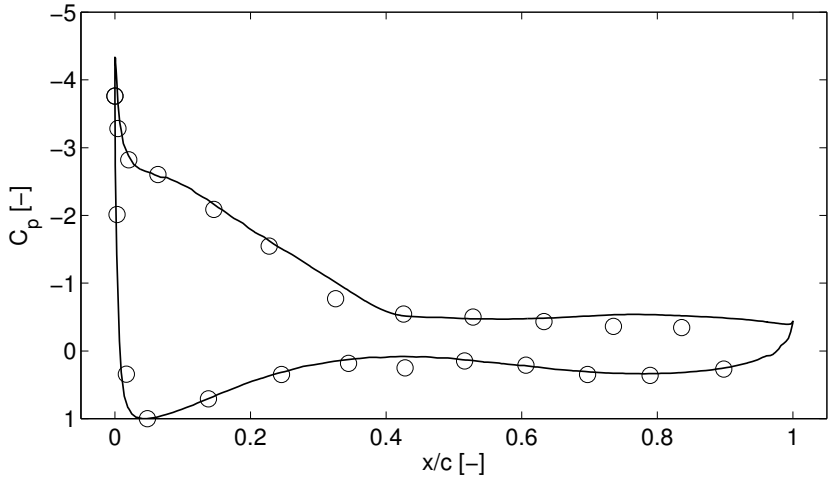

Figure 5.5: C_p distribution from $r = 0.60R$ for $U_\infty = 24m/s$, corresponding to $AoA = 17°$. The circles indicate 3D experimental results and the full line shows 3D numerical results.

At $r = 0.25R$ (Fig. 5.3), the blade rotation induces two important effects on the suction side: the suction peak is enhanced and the slope of the adverse pressure gradient is reduced. Both effects lead to a delay of the point of separation, which is the point where the adverse pressure gradient and the region with constant, nearly zero pressure gradient meet (Schreck et al., 2007). In the 2D case the separation point is located at $x \approx 0.2c$, whereas in the 3D experimental case it seems to be at $x \approx 0.3c$, although in this case the change in slope, i.e. pressure gradient, is more gradual, what complicates the exact determination of the separation point. Consequently, the lift in the 3D case is greatly enhanced (see also Fig. 5.1-a). The numerical results predict very well these phenomena, showing an excellent agreement with the 3D experimental results.

At $r = 0.35R$ (Fig. 5.4), evidence of rotational effects is present both in the experimental and numerical results, although their intensity is much lower than at $r = 0.25R$. The simulations clearly overpredict the stall delay effect, which according to the 3D experiments seems to be nearly negligible. Ultimately, this results in the overprediction of the computed C_l seen in Fig. 5.1-b. The C_l enhancement of the 3D experimental results with respect to the 2D experiments is caused by the magnified suction peak. Sicot et al. (2008), who studied experimentally a 1.34 m rotor diameter wind turbine, also observed lift enhancement without evidence of stall delay at two radial positions ($r = 0.26R$ and $r = 0.50R$). The lack of stall delay was attributed to the high turbulence level of their experimental setup (TI= 9%). However, in the MEXICO experiment the turbulence intensity was only TI=0.8%, what contradicts their assumption. This leads to the conclusion that stall delay and C_l enhancement can exist independently from each other (although they are often observed together) no matter what the flow regime is.

At $r = 0.60R$ (Fig. 5.5), the agreement between experimental and numerical results is again excellent, and the C_p distribution resembles qualitatively those from $r = 0.25R$ and $r = 0.35R$: a strong suction peak in the proximity of the leading edge is followed by an adverse pressure gradient and a region with nearly constant pressure, which extends until the trailing edge. This type of C_p distribution is characteristic for 2D airfoils with trailing edge separation. Having

such distributions in regions where rotational effects do not play any role, is not surprising. However, in regions influenced by rotational effects, other C_p distribution shapes are usually expected. For instance, in the NREL UAE Phase VI turbine the C_p curves from regions influenced by rotational effects exhibited no suction peak and no (or very weak) adverse pressure gradient (Schreck and Robinson, 2002). In a more recent work, Schreck et al. (2010) have highlighted that the MEXICO rotor blades do not exhibit those features. Ronsten (1992) performed experiments on a 2.375 m rotor blade, and his results show that in regions affected by rotational effects, the C_p curves displayed a very reduced adverse pressure gradient extending uniformly from a broad suction peak until the trailing edge. Sicot et al. (2008) also obtained similar C_p curves in their experimental study of rotational effects on a 1.34 m wind turbine rotor. On the other hand, the experimental and numerical study by Troldborg et al. (2013) on the 3D airfoil characteristics of a multimegawatt wind turbine, showed C_p distributions from radial positions affected by rotational effects that resemble the results from the MEXICO turbine: the suction side exhibited a suction peak in the proximity of the leading edge, then the pressure was increased by an adverse pressure gradient and finally the pressure was kept nearly constant until the trailing edge.

One more interesting feature of the C_p distributions from Fig. 5.3-5.5, is the fact that the pressure level in areas with separated flow, i.e. regions from the suction side with nearly constant pressure, is very similar for the 2D and 3D cases. This is in conflict with the observations done by Schreck and Robinson (2002) in the NREL Phase VI wind turbine, who observed that the pressure in the separated region was substantially reduced as compared with the 2D airfoil. Lindenburg (2003) also analysed the same measurements and concluded that radial flows in the separated flow region cause an important additional negative pressure, which contributes to the lift enhancement.

The lack of such a strong additional negative pressure in the separated regions of the MEXICO blades could be interpreted as a lack of substantial radial flows. However, as it will be shown in Section 5.3.3 and Section 5.3.4, this assumption does not hold true.

All these observations show that there is not a unique shape of C_p distribution that can be considered as representative for rotational effects. This hinders the development of generalized correction models that perform well for any kind of wind turbine.

5.3.3 Flow field in the wake after the blade passage

The study of the Particle Image Velocimetry (PIV) experimental data in conjunction with the numerical results allows to gain a better insight into relevant flow features which are important for the analysis of the rotational effects.

Fig. 5.6 shows schematically the area where the flow field was experimentally captured by means of PIV measurements. The PIV sheets cover the range of radial positions $0.52R < r < 1.21R$, and the range of axial positions $-0.13R < x < 0.13R$, where $x = 0R$ is the rotor plane (upstream of the rotor plane the axial coordinates are negative, whereas downstream of it they are positive). For radial positions lower than 0.52R, only numerical data are available.

All the presented results were acquired 10 degrees after the blade passage. The experimental data, which are available for the wind speeds 10, 15 and 24 m/s, are compared with the numerical results in Fig. 5.7, Fig. 5.8 and Fig. 5.9, respectively. The white regions observed in the numerical results correspond to the intersection of the nacelle and the blade inboard region

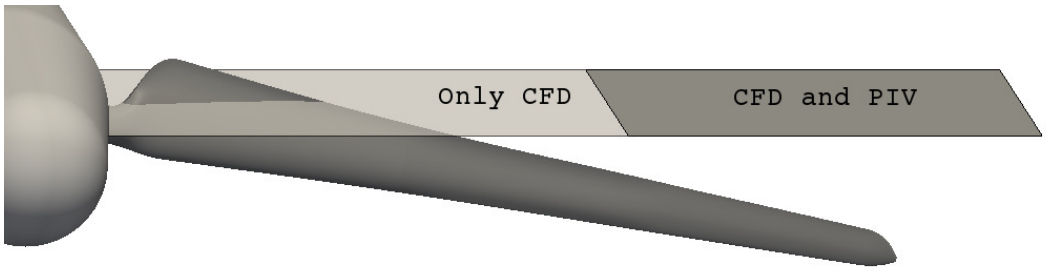

Figure 5.6: Schematic view of the plane where the flow field was measured 10° after the blade passage. The PIV windows only cover the outboard region, whereas the CFD results encompass the whole blade span.

with the plane where the flow field is studied (the intersection is also displayed in Fig. 5.6). All the velocity fields shown in this analysis have been normalized with the free stream wind speed in order to make the comparison between the three different cases easier.

Fig. 5.7-a and 5.7-c show respectively the measured and simulated axial wind speed for U_∞ = 10 m/s. As it can be seen, the axial wind speed in the rotor plane is about one third of the freestream velocity, indicating a high induction. The high induction leads to a strong wake expansion, which in turn is responsible for a significant radial component in the wind speed, especially in the blade outboard region, as presented in Fig. 5.7-b for the experiment and Fig. 5.7-d for the simulation. However, as it can be seen in the wake, the passage of the blade does not trigger additional radial flows. This is an indication that at this wind speed, at which rotational effects are non-existent, the flow in the blade boundary layer is attached and 2D. The experimental and numerical results compare fairly well for both the axial and radial velocity components, although the simulation underpredicts a bit the strength of the tip vortex and the radial velocity component for $r > R$. Interestingly, the numerical results show the existence of a substantial radial velocity component in the blade root region, which seems to suggest that the flow in that area is separated.

At $U_\infty = 15$ m/s, the outboard region of the rotor plane presents an axial wind speed which almost reaches two thirds of the free-stream wind speed, indicating optimum induction (Fig. 5.8-a for the experiment and Fig. 5.8-c for the simulation). At inboard positions the axial wind speed is lower, i.e. the induction is higher, but it should be noted that at those spanwise positions the influence of the blade body on the studied plane is much stronger because of its proximity (Fig. 5.6). The reduced induction as compared to the case with U_∞ = 10 m/s implies less wake expansion, what also means that the radial velocity component in the outboard region becomes weaker (Fig. 5.8-b and Fig. 5.8-d for the experimental and numerical results, respectively). The blade passage does not contribute to increase significantly the radial velocity component in the wake, but the experimental results suggest that it triggers a very weak vortex sheet, which does not exist in the numerical results. These results imply that the flow in the boundary layer is basically attached and 2D, although incipient separation might exist close to the trailing edge. Apart from this, the agreement between numerical and experimental results is excellent in spite of some rather artificial effects in the experimental results in the range $0.52R < r < 0.7R$. Micallef et al. (2013) attributed those effects to the laser sheet reflection on

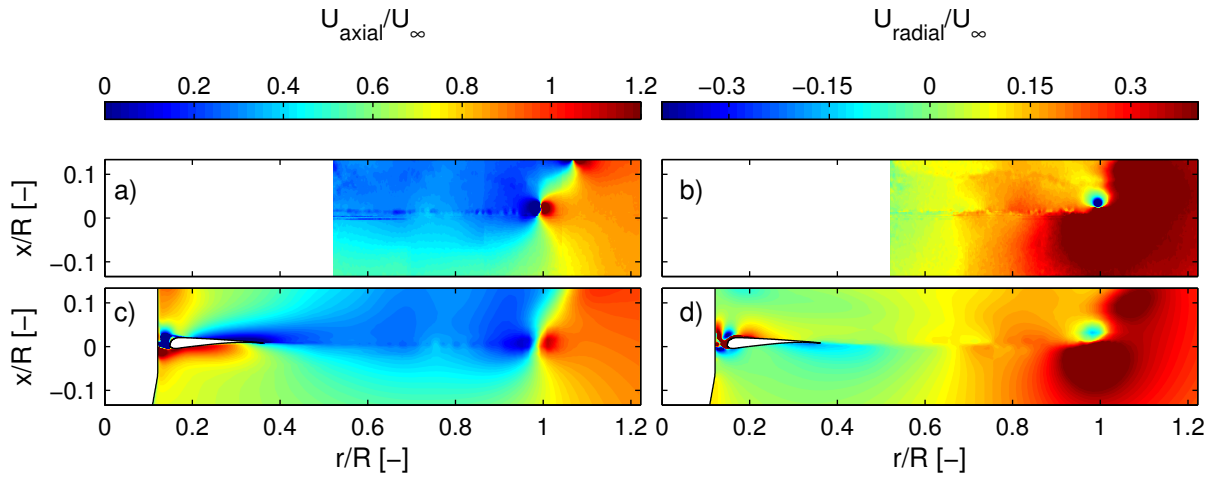

Figure 5.7: Measured and computed flow field at $U_\infty = 10$ m/s. Upper row: experimental results, lower row: numerical results, left column: axial wind speed, right column: radial wind speed.

the blade. The root vortex is also easily recognizable in the radial component of the numerical results.

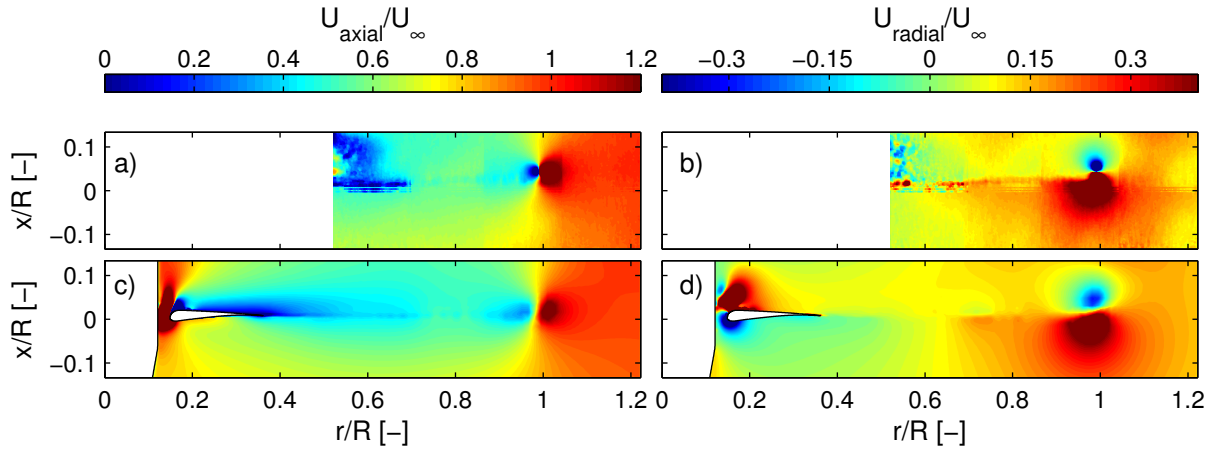

Figure 5.8: Measured and computed flow field at $U_\infty = 15$ m/s. Upper row: experimental results, lower row: numerical results, left column: axial wind speed, right column: radial wind speed.

From Fig. 5.9-a and Fig.5.9-c (experimental and numerical results, respectively), it is clear that at U_∞=24 m/s, the axial induction is weaker than at U_∞=15m/s. This circumstance reduces the wake expansion and consequently also the radial velocity component promoted by the expansion itself (Fig. 5.9-b and Fig. 5.9-d). However, the blade passage increases the radial velocity due to the trailed vorticity. This effect is visible in the experimental as well as in the numerical results, in spite of some inconsistencies between both of them. Here it is worth to recall that under these conditions (stall) the flow is non-stationary and the experimental re-

sults, which are phase-locked, are averaged over 30 frames, where a frame is the result of two subsequent photographs, i.e. an image pair (Boorsma and Schepers, 2003). Therefore, after averaging the measured frames the radial velocities appear as a smeared blob of spanwise flow along the blade radius. This poses a challenge for the comparison with the numerical results because the simulations are steady-state, so only one solution is obtained and no averaging over time is possible. This problem is accentuated by the flapwise oscillations: as it can be seen in the experimental results (Fig. 5.9-a and Fig. 5.9-b), the axial position of the tip vortex is located further downstream than in the simulation (Fig. 5.9-c and Fig. 5.9-d). In fact, the same happens at U_∞=10 m/s and U_∞=15 m/s, although the discrepancy increases with the wind speed. This seems to indicate that the blade presents a certain deflection in the flapwise direction when it is loaded. The experimental results (especially those corresponding to the axial velocity component, Fig. 5.9-a) also show that the vortex sheet located along the blade span is a bit bended towards the downstream direction, what confirms the blade deflection. Carrion et al. (2012) performed a fluid-structure interaction study of the MEXICO turbine and estimated that the blade tip deflection was approximately 5 cm for U_∞ = 15 m/s. For U_∞ = 24 m/s it should be even more. Under stall conditions, where the flow is highly unstationary, the deflection is expected to be subjected to substantial flapwise oscillations. The corresponding oscillations in the wake, when averaged, contribute to the blurred distribution of radial velocities seen in the experimental results, complicating the comparison with the steady-state, rigid blade CFD simulation.

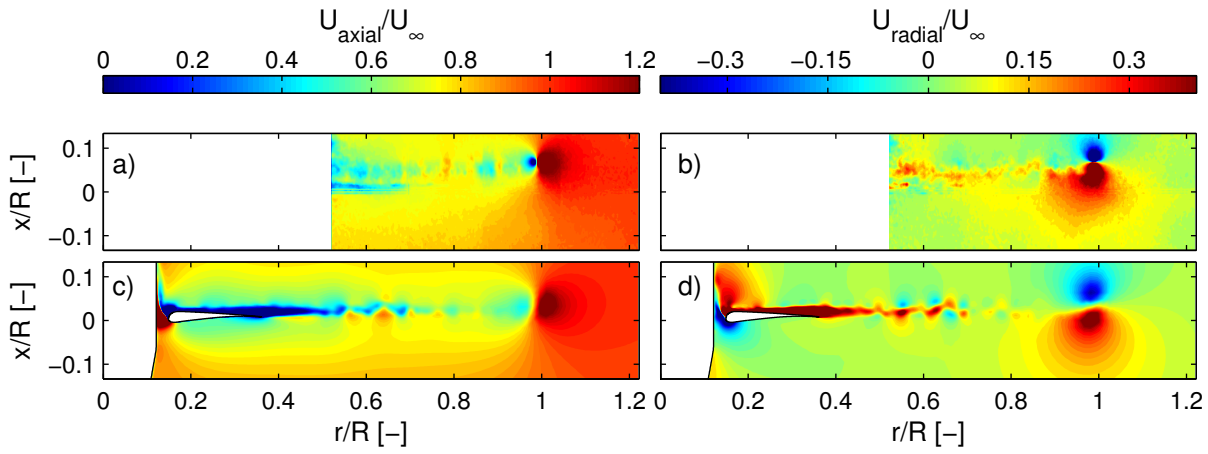

Figure 5.9: Measured and computed flow field at $U_\infty = 24$ m/s. Upper row: experimental results, lower row: numerical results, left column: axial wind speed, right column: radial wind speed.

In the range $0.70R < r < 0.90R$ the numerical results seem to underpredict the (weak) radial flow component. This is approximately the region where the experimental 3D airfoil characteristics are not consistent with the simulations and display a lift reduction and a drag increase with respect to the 2D case (Fig. 5.1 and Fig. 5.2). The experimental radial velocity field seems to suggest that the reason for the underperformance of the blade in that region is connected to the increased trailed vorticity. However, it is not clear which is the source of the increased trailed vorticity: the NACA 64-418 airfoil is used in the range $0.74R < r < R$. Since there is no

transition between different airfoil types in that region, no abrupt change in the bound circulation is expected there, meaning that no increased trailed vorticity is expected either. A possible torsional deflection caused by the pitching moment would act in the nose-down direction, what would reduce the AoA, decreasing at the same time the trailed vorticity. The effect can therefore not been explained by a torsional deflection. Furthermore, as described in Section 5.3.1, the influence of the tip vortex and the radial flows is not believed to be the cause for this aerodynamic behaviour. Further insight is gained in the next section.

At lower radial positions the numerical results are in better agreement with the measurements. In the inboard region, the analysed plane intersects the blade and the numerical results provide valuable information about the flow in the boundary layer. Fig. 5.9-d shows that the flow in this region, in which rotational effects play an important role, is dominated by a strong radial component (in contrast to the cases in which rotational effects were negligible). The fact that the rotational effects only exist in the presence of radial flows in the boundary layer suggests that most probably there is a connection between both phenomena. This is in conflict with the work of Wood (1991), who concluded that rotational effects can be explained in terms of changes on the pressure gradient in the external inviscid flow. In other words, Wood suggested that inertial forces in the boundary layer (causing e.g. radial flows) can be disregarded because boundary layers respond to the pressure gradients imposed on them. On the contrary, other authors like Dumitrescu and Cardos (2004) have highlighted the importance of the blade boundary layer and the forces acting on it for the study of rotational effects.

5.3.4 Wall-bounded flow field

In order to analyse in more detail the wall-bounded flow field on the suction side, the simulated wall shear stress on the suction side is visualized as oil flow in Fig. 5.10 for all the computed wind speeds. Under stall conditions, the separation line is clearly recognizable along the span as the location where the flow coming from the leading edge ceases to be oriented in the chordwise direction. Furthermore, the figure shows with circles the separation point obtained from the experimental C_p distributions at five radial positions (in the cases where separation occurs) . Here, it has been assumed that the location of the separation point corresponds to the point where the adverse pressure gradient meets the region with a constant, nearly zero pressure gradient (Schreck et al., 2007; Sicot et al., 2008).

At U_∞ = 10 m/s and U_∞ = 15 m/s (Fig. 5.10-a and Fig. 5.10-b, respectively), the flow is almost fully attached and 2D. However, evidence of separation exists in the root region (around the area of maximum chord) in both cases. Furthermore, incipient flow separation is present in the inboard-aft region at 15 m/s. From the experimental results it was not possible to determine clearly if there was separation at inboard positions, so no experimental separation point is shown for these wind speeds.

At U_∞ = 19 m/s and U_∞ = 24 m/s (Fig. 5.10-c and Fig. 5.10-d, respectively), the blade is stalled to a great extent. At inboard and mid-span positions ($r = 0.25R$, $r = 0.35R$ and $r = 0.60R$) the location of the computed separation line is consistent with the experimental separation point. However, at U_∞ = 24 m/s the experimental separation point from outboard radial positions ($r = 0.82R$ and $r = 0.92R$), is closer to the leading edge than in the simulations. As it was seen in Fig. 5.1-d and Fig. 5.1-e, the numerical results at these stations resemble approximately the 2D case for high AoA, so the measured underperformance of the blade with

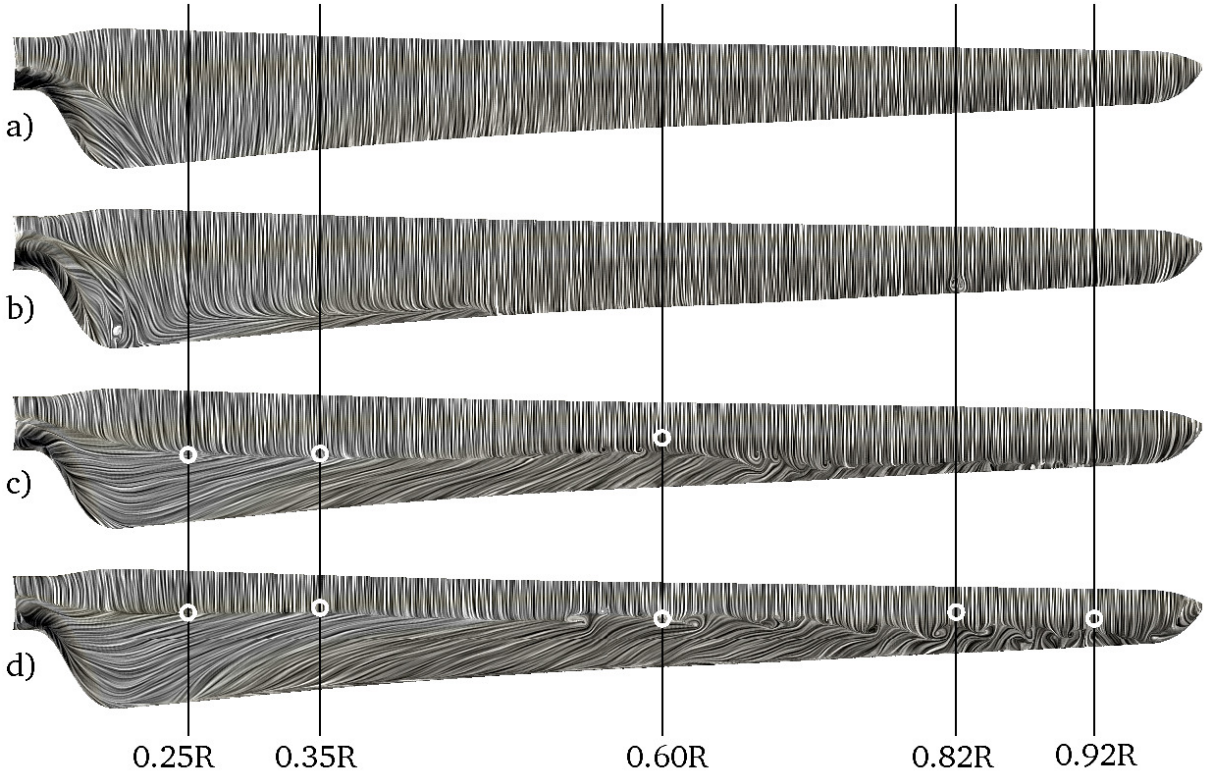

Figure 5.10: Oil-flow representation of the computed wall shear stress on the suction side at different wind speeds: a) U_∞=10 m/s, b) U_∞=15 m/s, c) U_∞=19 m/s and d) U_∞=24 m/s. The white dots indicate the point of separation extracted from the experimental C_p distributions.

respect to the 2D airfoil (Section 5.3.1) should be ascribed to the advancement of the separation point. Furthermore, this is also consistent with the C_d rise observed in Fig. 5.2-d and Fig. 5.2-e and with the increased trailed vorticity described in Section 5.3.3. However, it is still not clear what exactly is causing this effect. Further research is therefore needed for explaining it.

From Fig. 5.10-c and Fig. 5.10-d it is also evident that under stall conditions large regions of the suction side are dominated by radial flows, which additionally contain a recirculation component towards the leading edge. The combination of the recirculation and the radial flow in the inboard region creates a standing vortex on the separated area, which "pumps" the air radially from the root region outwards. This effect, which is commonly refered to as "radial pumping", has been observed both experimentally (Robinson et al., 1999; Corten, 2001; McCroskey and Yaggy, 1968) and numerically (Sørensen et al., 2002; Schreck et al., 2007) in other turbines operating under stall conditions, and it is usually considered to be intrinsically related to the existence of rotational effects.

Two main causes have been identified in the literature for explaining the origin of the radial flows in the boundary layer. The first explanation attributes the radial flows to the difference in dynamic pressure along the blade span. This pressure difference occurs because for a given rotational speed, the local tangential speed is directly proportional to the local radius. Consequently, the air is supposed to travel from regions of high pressure (blade root) to regions of low pressure (blade tip). This explanation was supported by the observations done in the NREL UAE Phase VI wind turbine by Schreck and Robinson (2002), who concluded that strong spanwise pressure gradients were responsible for the radial flows. The second explanation considers that the spanwise pressure gradients found on the separated flow regions are too small for causing any radial flow, so it attributes the radial flows to the centrifugal force acting on the separated flow (Lindenburg, 2003).

In Fig. 5.11, the isobars obtained from the simulation with $U_\infty = 24$ m/s are plotted together with arrows indicating the flow direction (extracted from the computed wall shear stress after inverting the sign).

From this figure, it is evident that the flow direction in the separated region is mostly unrelated to the pressure gradients. Consequently, in the MEXICO turbine the radial flow in the boundary layer must be mainly attributed to the centrifugal force and not to spanwise pressure gradients. The fact that larger wind turbines rotate slower may lead to thinking that this effect could be much less pronounced in utility-scale wind turbines, since the centrifugal force is proportional to the square of the rotational speed and only linearly proportional to the radius. However, it must be kept in mind that the tip speed ratio for both small and large wind turbines is comparable, what should lead to similar effects of rotation (as it was also explained in Section 5.2.1 with the Rossby number).

As often described in the literature about rotational effects (Breton et al., 2008; Lindenburg, 2003), the Coriolis force acting on the separated radial flow apparently pushes that volume of air towards the trailing edge, what contributes to delay the separation. Perhaps more importantly, the centrifugal force, which of course also acts on the attached flow region, gives the attached flow a radial velocity component in regions close to the end of adverse pressure gradient, where the chordwise velocity component is very weak. The Coriolis force acting on that radial velocity component is also oriented towards the trailing edge, so it partially counteracts the adverse pressure gradient, and consequently helps to delay separation before it happens at all. The fact that the Rossby number decreases towards the blade root (as seen in 5.2), suggests that Coriolis

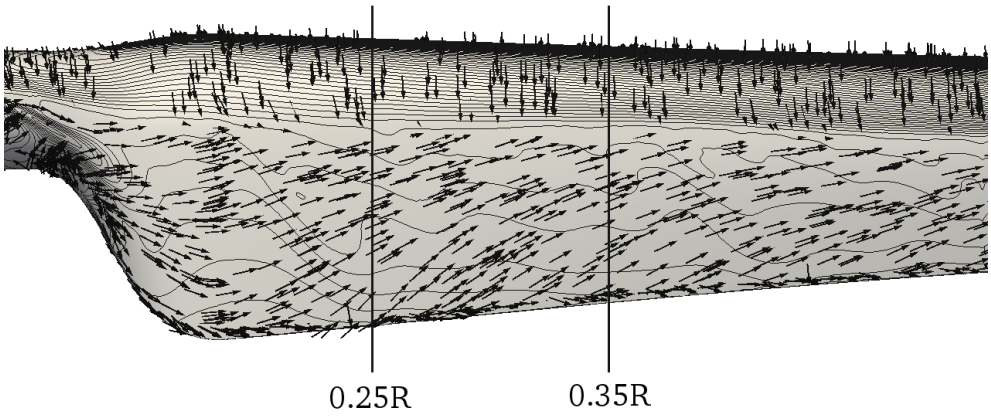

Figure 5.11: Computed isobars of surface pressure and arrows indicating the flow direction at U_∞ = 24 m/s. The isobars go from 0 Pa to 8000 Pa with an interval of 80 Pa. The radial flow in the separated region is mostly unrelated to the pressure gradients.

.

force plays a decisive role in the stall delay effect.

5.4 Conclusions

In the current work, a CFD model of the MEXICO turbine based on the open source toolbox OpenFOAM has been used in conjunction with experimental results for the study of rotational effects. The closer to the blade root, the stronger was their influence on the aerodynamic performance. The evidence shows, that the subsequent phenomena of stall delay and lift enhancement can exist independently from each other, although they tend to manifest themselves together. Furthermore, their influence on the drag seems to be airfoil-type dependent: the drag is not affected at positions where the DU91-W2-250 airfoil is used, but it is reduced at the radial position with the RISØ-A1-21 airfoil. It must be noticed, that most correction models for rotational effects assume a drag increase, what is in conflict with our observations. In fact, the influence of rotational effects on the C_p distributions differs qualitatively very strongly from one turbine to the other, implying that no single shape of C_p distribution can be considered as representative for rotational effects. This is a major issue for the development of generalized correction models.

The use of flow field data from PIV experiments and numerical simulations allowed to observe that the presence of a strong radial velocity component in the rotor plane does not lead to lift enhancement or stall delay as long as its origin is not in the blade boundary layer. On the other hand, the radial flows dominating the aft region of the boundary layer under stall conditions seem to be intrinsically connected to the existence of rotational effects. According to our results, these radial flows are due to the centrifugal force acting on the separated air volume, whereas in the literature of the NREL UAE Phase VI wind turbine, spanwise pressure gradients are mentioned to be responsible for the effect. Furthermore, the Coriolis force acting on the

radial flow seems to play a crucial role in the stall delay effect.

These findings show the lack of generality of the state of the art knowledge about rotational effects and stress the necessity for more research in this field.

Chapter 6

Insight into the blade tip flow[1]

6.1 Introduction

Akay et al. (2012a), Micallef (2012) and Micallef et al. (2012, 2013) report experiments on two two-bladed rotors (TUD-A and -B) of 2 m diameter in the 3 m diameter Open Jet Facility of TU-Delft, with emphasis on the root and tip region. Schepers and Snel (2007) and Schepers et al. (2012) report experiments on a 4.5 m diameter three-bladed rotor called Mexico (Measurements and EXperiments In COntrolled conditions) in the 9.5×9.5 m^2 open test section of the German-Dutch Wind Tunnel. Xiao et al. (2011) report detailed tip vortex experiments on a 1.25 m diameter model of the NREL UAE phase VI wind turbine described by Hand et al. (2011), in an open test section of 3.2 m diameter. The flow near the blade tip of these rotors shows the tip vortex, when leaving the tip, moving inboard after which the wake expansion moves the vortex to a larger radius. Micallef et al. (2013) provide a detailed description of this phenomenon, Micallef (2012) and Micallef et al. (2012) give the experimental data of the TUD and Mexico rotor experiments and the analyses, as Xiao et al. (2011) does for the NREL model rotor. The first mention of this effect was by van Kuik (1991), where the physical mechanism is explained. The tendency of any tip vortex to first move inboard may be stronger than the wake expansion, depending on tip shape and tip load. For a propeller, both effects sum up, and the tip vortex always travels to a smaller radius. The TUD-A rotor shows some inboard motion of the tip vortex, but this effect is better quantified for the other rotors. At 10° azimuth angle behind the blade quarter chord position, the radial position of the tip vortex of the Mexico rotor is $0.99R$, and of the TUD-B rotor $0.995R$ with the expansion to values $r > R$ starting only after 30° azimuth angle. The tip vortex of NREL-model rotor reaches 0.98R at 30° azimuth angle after which expansion starts. The inboard induction is caused by the chordwise vorticity at the tip (see Sect. 6.3.1), since all other blade bound or free wake vorticity components cannot induce such an inboard velocity, as becomes clear by qualitative considerations based on the Biot-Savart induction rules. Although the effect is least visible for the TUD-B rotor, it is most suited for detailed tip flow analysis because of its geometry and because the tip flow is measured

[1]This chapter is an extract of the numerical work included in the article published as G.A.M. VAN KUIK, D. MICALLEF, I. HERRÁEZ, A. H. VAN ZUIJLEN and D. RAGNI: The role of conservative forces in rotor aerodynamics, *Journal of Fluid Mechanics*, **750**:284–315
Minor changes of the original document have been performed for the sake of clarity. See authors contributions in the section "List of publications".

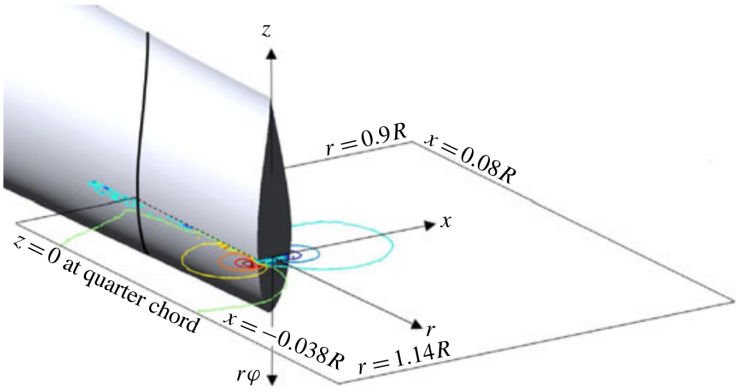

Figure 6.1: The geometry of the tip of the TUD-B rotor, the coordinate system and the plane at $z = 0$ coinciding with the quarter-chord position, used for the measurements and calculations. The iso-lines indicate the radial velocity. The square contour is used to determine the chordwise bound circulation.

in all required details. Fig. 6.1 shows its almost cylindrical blade shape with a blunt tip surface having a zero pitch angle at $r = R$. All results concern the rotor operating at its optimal tip speed ratio seven at a wind speed of 6 m/s.

6.2 Numerical method

The CFD results were computed with the open-source C++ object-oriented numerical toolbox OpenFOAM (2015) using a Reynolds-averaged Navier–Stokes simulation approach. OpenFOAM is a finite-volume software for solving numerically partial differential equations. The computation was run in parallel in the FLOW (2015) computer cluster of the University of Oldenburg using 180 cores. An unstructured and hexa-dominant mesh design was chosen for its high adaptability (in comparison to structured meshes) to complex geometries. The computational mesh includes both blades and the nacelle. The tower is omitted, since it is assumed that it does not significantly influence the aerodynamic phenomena studied in this work. More than 99 % of the mesh elements are hexahedra, the rest being polyhedra. The total number of cells is 20 million. For the actuator line simulations, the same kind of grid was used, but the number of cells could be reduced to 4 million owing to the fact that no turbine components were meshed. The whole mesh generation process has been carried out with tools available in OpenFOAM. The comparatively low computational cost of the actuator line model allowed a time-accurate computation to be performed, whereas a steady-state simulation was used for the full rotor approach. In that case, the rotation of the rotor was accounted for by adding the Coriolis and centrifugal forces to the momentum equations in the regions subjected to rotation. This avoided the use of computationally expensive moving grids. The pressure–velocity coupling was accomplished by means of the SIMPLE algorithm in the full rotor case and by the PIMPLE algorithm in the actuator line case. The Prandtl/Glauert tip loss correction (see Glauert, 1935, chapter VII) has been applied to the computation with the actuator line to obtain a more realistic

	$T_{\varphi,blade}$	$T_{x,blade}$	$T_{\varphi,tip}$	$T_{x,tip}$	$R_{x,tip}$
GCI	0.75	1.16	0.35	0.02	0.13

Table 6.1: Discretization error of the CFD simulations.

loading both at the blade tip and root. The actuator line library from SOWFA (2015) was used for implementing an in-house solver for that kind of computation. In both types of simulations, a second-order linear upwind discretization scheme has been used for the convective terms. The simulations were run fully turbulent using the turbulence model by Spalart and Allmaras (1994). This turbulence model has been chosen for its robustness and satisfactory performance for wall-bounded and adverse-pressure-gradient flows, as well as for its comparatively low sensitivity to grid resolution. In spite of its limitations for separated and wake flows, it is well suited for the research presented here considering blade loads at attached flow conditions. The calculation of the forces has been accomplished in two different ways: integrating the surface pressure along the blade walls, and applying the Kutta–Joukowsky theorem o the circulation obtained after "probing" the wind speed field at a distance of 5 mm around the blade surface. The velocity component tangential to the blade surface was used to derive the radial vorticity, whereas the chordwise vorticity was derived from the radial velocity component. The radial circulation was obtained by integrating the radial vorticity from the leading to the trailing edge. The chordwise circulation was computed by integrating the chordwise vorticity from inboard radial positions towards the blade tip. The uncertainty of the CFD simulations has been assessed by means of the GCI (Roache, 1998b). Simulations with a coarse, medium and fine grid have been performed using $10 \cdot 10^6$, $15 \cdot 10^6$ and $20 \cdot 10^6$ cells, respectively. In order to achieve convergence, the residuals for all the field variables were monitored to ensure a residual decrease of at least three orders of magnitude. Furthermore, the integral quantities torque and thrust were also monitored during the simulation for convergence. Starting with the $10 \cdot 10^6$ cells grid, the mesh has been systematically refined, i.e. the refinement itself was structured in spite of the mesh being of type unstructured. The results presented in this work refer to the finest mesh. The study of the numerical uncertainty has been done focusing first on the azimuthal load per blade, $T_{\varphi,blade}$, and thrust per blade, $T_{x,blade}$. The corresponding levels of uncertainty presented in Table 6.2 are sufficiently low to consider this general verification of the simulation model as satisfactory. Further, the uncertainty in the tip region of the blade, which is the main region of interest for the research, is analysed in more detail. Table 6.2 gives the uncertainty for the thrust force $T_{x,tip}$ associated with the outer 10 % of the blade span, the radial force $\mathscr{R}$ as well as the ratio $\mathscr{R}/T_{x,tip}$. This force ratio $T_{x,blade}$ is ≈ 10 %, i.e. ≈ 80 times higher than its corresponding uncertainty, so the uncertainty of the simulation model is considered to be low enough for the scope of our study.

6.3 Results

6.3.1 Bound vorticity

Fig. 6.2 shows the most simple rotor blade with a constant cross-section C, being a symmetric aerofoil without pitch or twist angle. This is not an optimal rotor design, but although not self-starting, it acts as a wind turbine rotor once the tip speed ratio is sufficiently high. In general, a tip aerofoil is cambered or has an inclination with respect to the disc plane, so the chordwise vorticity also has an axial component. By the chosen simple configuration, the blade can carry only radial and azimuthal vorticity components, which suffices for the present analysis. Both components of the vorticity are sketched in Fig. 6.2, where it is represented as a vortex sheet with strength γ resulting from the integration of the vorticity across the blade thickness.

The relation between the two components will be now expressed in terms of the circulation Γ . For any lifting surface, the well-known relation between the change of spanwise circulation and trailing vorticity is $\gamma_{chordwise} = -\partial\Gamma_{spanwise}/\partial r$, where r is the spanwise coordinate. Expressed in the coordinate system of Fig. 6.2 this becomes $\gamma_\varphi = \partial\Gamma_r/\partial r$, where the minus sign has vanished since the direction of the chordwise and azimuthal coordinates is opposite (see Fig. 6.1). The subscript r indicates that Γ is defined in a plane normal to a radius. Similarly, the circulation Γ_φ is defined in a plane normal to the chordwise direction. When measured from the tip to a local value of r then $\Gamma_\varphi(r) = -\int_R^r \gamma_\varphi d\rho$ or $\gamma_\varphi = -\partial\Gamma_\varphi/\partial r$. Combining the two expressions for γ_φ gives

$\gamma_\varphi = \partial\Gamma_r/\partial r = -\partial\Gamma_\varphi/\partial r$ or

$$\frac{\partial(\Gamma_r+\Gamma_\varphi)}{\partial r} = 0$$

This gives the relation between the circulation around a radius and the circulation around an azimuthal line, at any position of the blade. It provides a coupling between the radial vorticity and the azimuthal vorticity. For rotor blades having the circulation distributed along the span as constant as possible, the azimuthal vorticity will be located near the blade root and tip, so the conservative load will then be concentrated near the root and tip.

6.3.2 Bound circulation

CFD codes as used by Herráez et al. (2014) as well as vortex panel codes as used by Micallef et al. (2013) are able to capture the tip flow in detail. Fig. 6.2 shows the plane of observation with the coordinate systems. Besides the (x,r,ϕ) system defined in Fig. 6.1, also the local (x,z,r) system is used since it is convenient to express local flow properties in the chordwise coordinate z. The measured and calculated radial flow are shown in Fig. 6.3. At the tip, a large difference in radial velocity at the pressure side of the blade tip ($x < 0$) and suction side is visible, indicating chordwise vorticity bounded at the tip. This vorticity component is shown in Fig. 6.4, indicating high values for $r/R > 0.97$. This chordwise vorticity may be considered as the beginning of the tip vortex. Fig. 6.5 gives the pressure distribution at the suction side of the tip, showing for $r/R > 0.98$ the low-pressure region due to this vortex. Ferrer and Munduate (2007) show similar pressure distributions for other rotor lay-outs. Fig. 6.6 shows how the blade bound radial vorticity γ_{radial} is connected to the bound chordwise vorticity γ_{chord} expressed in

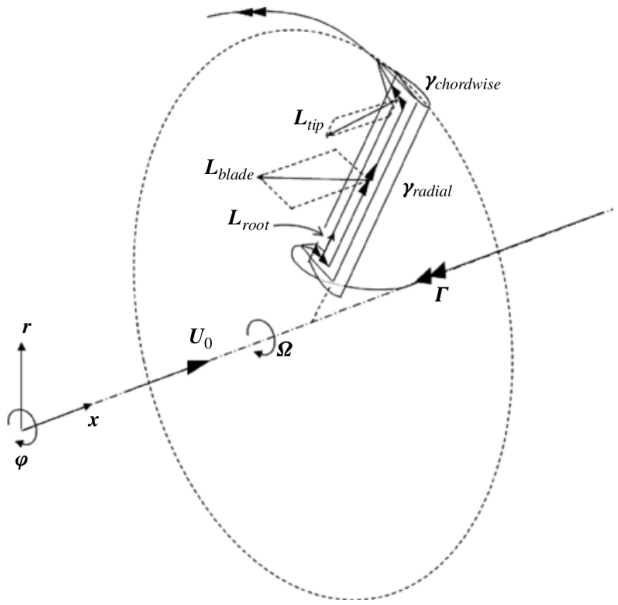

Figure 6.2: Rotor blade bound vorticity, with loads acting on the flow. The loads are drawn assuming $v_x > 0$, $v_{\varphi,rot} < 0$, $v_r = 0$ near the root and $v_r < 0$ near the tip

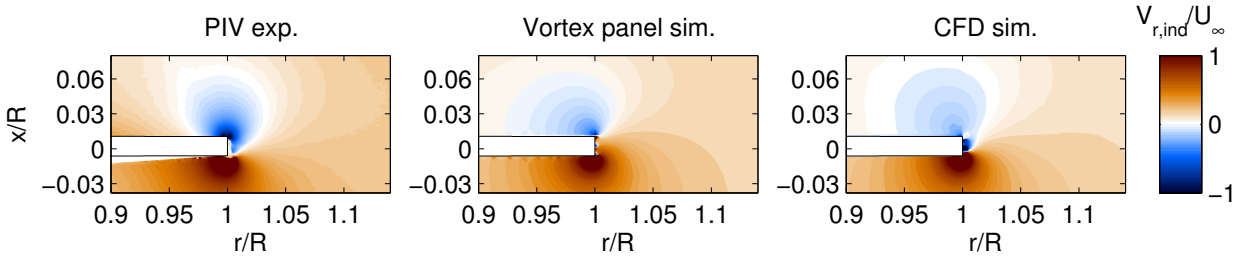

Figure 6.3: Comparison of the radial velocities in the meridional plane through the quarter-chord tip position; U_∞ is aligned with the rotor axis, and the tip speed ratio $\omega R/U_\infty = 7$.

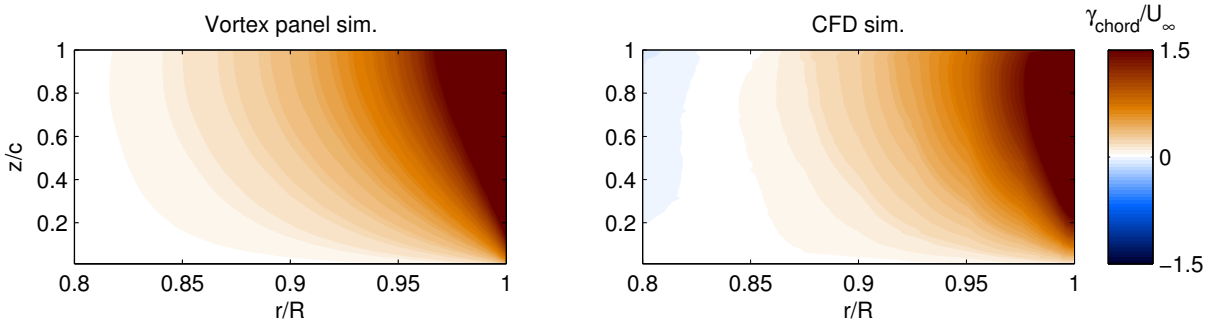

Figure 6.4: The chordwise vorticity determined by difference in radial velocities.

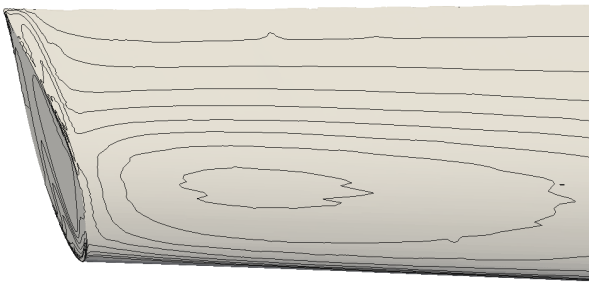

Figure 6.5: The pressure at the blade tip shown only qualitatively by isobars.

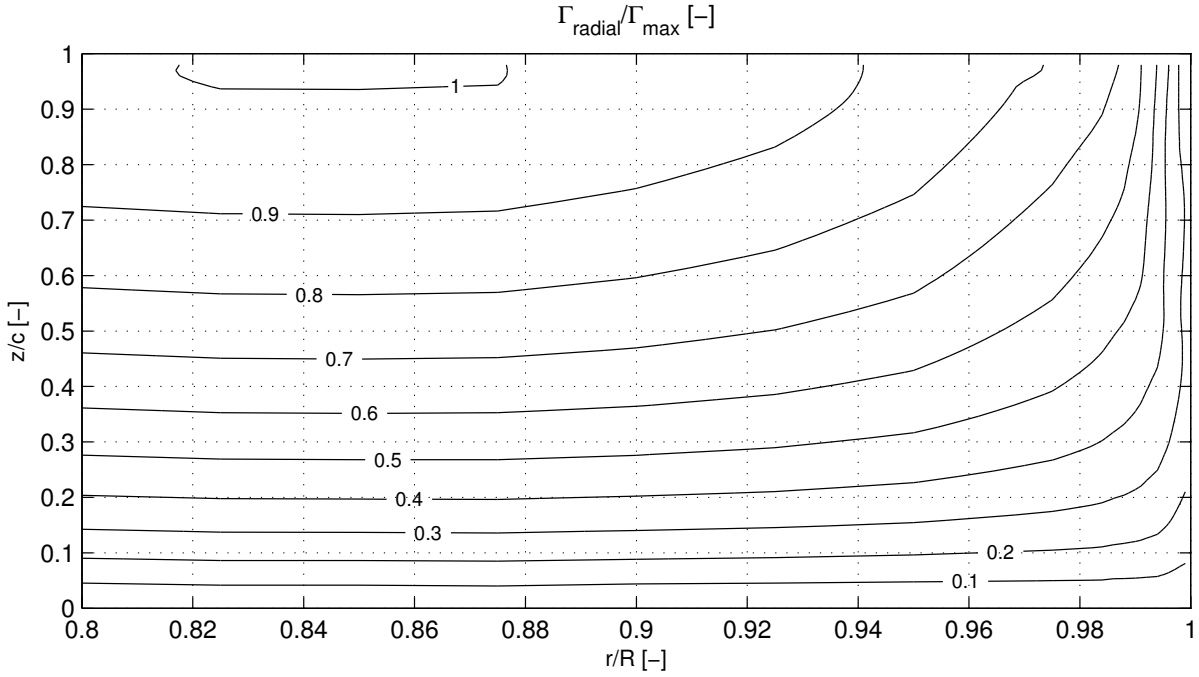

Figure 6.6: Iso-lines of constant percentage of the local circulation $\Gamma_r(r,z)/\Gamma_{r,max}(r)$ around the TUD-B rotor blade, determined by the CFD method; Γ_r is integrated from the leading edge to $\Gamma_r = \int_{le}^{z} \gamma_r d\zeta$

the circulation Γ . The value of the isocirculation lines gives the local circulation, measured from the leading edge le, so $\Gamma_r(r,z) = \int_{le}^{z} \gamma_{radial} d\zeta$, divided by the maximum blade circulation. This maximum occurs at the trailing edge at $r/R = 0.825$. With Γ_φ replaced by $-\Gamma_z$, gives $\Gamma_r - \Gamma_z = 0$ for a fixed chordwise position z when Γ_z is integrated inboard: $\Gamma_z(r,z) = \int_{R}^{r} \gamma_{chord} d\rho$. Consequently the iso-lines give the value for Γ_r, measured along the chord from the leading edge, as well as Γ_z, measured along the radius from the tip to inboard. As an example at the trailing edge the spanwise circulation increases from 0 at $r = R$ to $\approx 0.9\Gamma_{r,max}$ at $r = 0.94R$. In other words, 90% of the radial circulation leaves the blade as chordwise circulation in the outer 6 % of the blade. The figure shows that a small amount of the circulation leaves the tip – see the iso-lines 0.1 and 0.2. This missing part is not analysed further, but it is unbound vorticity or the contribution of the flat tip surface to the bound circulation. Fig. 6.6 is similar to figure 5 of Wald (2006) .

6.3.3 The conservative tip load

The chordwise circulation between $r = 0.9R$ and $r = R$, the normal force $\mathscr{N}$ and radial force $\mathscr{R}$ are determined by several means. The measured and CFD-calculated velocity field is integrated along the contour displayed in Fig. 6.1 to obtain the circulation $\Gamma(z)$ around the chordwise vorticity. The choice of the contour edges is such that no vorticity other than chordwise vorticity is contained within the integrated zone. On the contour side that cuts the blade, a linear jump

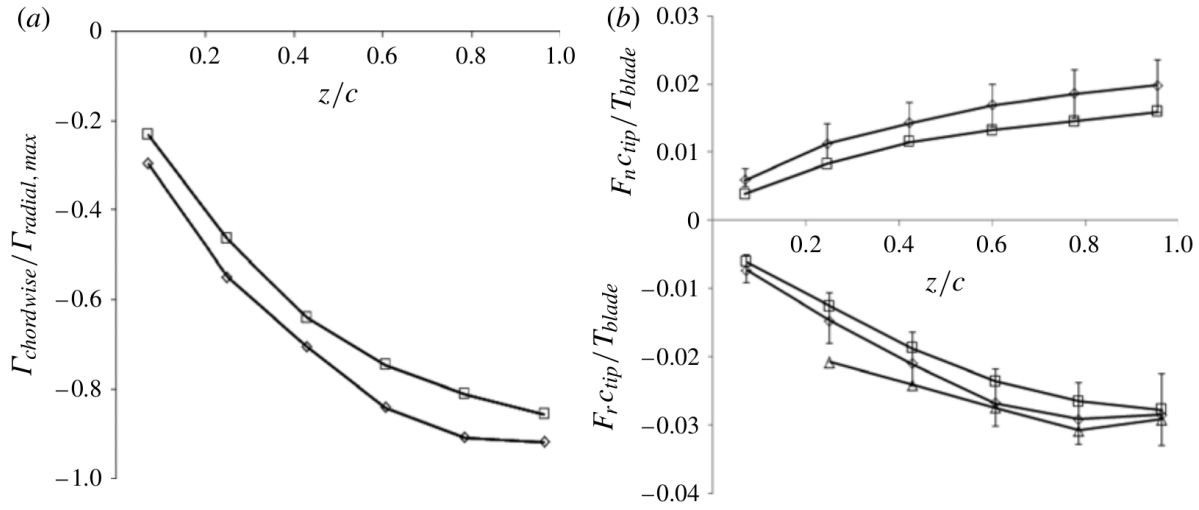

Figure 6.7: (a) Chordwise circulation, and (b) normal and radial loads. The squares show the K–J method applied to the CFD data. The diamonds indicate the same applied to the experimental data. The triangles present the experimental momentum method. The error bars for the K–J experimental load show the sensitivity for the position to determine $\boldsymbol{v}_{ref}$ .The sensitivity of the radial load for variations of the contour in the momentum method is 5 % of the values indicated.

in velocities is assumed, but this was found to have practically no influence on the calculated circulation. This procedure is repeated for six chordwise positions, with the results shown in Fig. 6.7. The two curves agree reasonably, with a maximum chordwise circulation of $\approx 0.9\Gamma_{radial,max}$. According to Fig. 6.6 the spanwise circulation at the trailing edge at $r/R = 0.9$ is $\approx 0.95\Gamma_{radial,max}$, which confirms the contour method.

The force is calculated by chordwise integration of the Kutta–Joukowsky load $-\rho\boldsymbol{v}_{ref} \times \boldsymbol{\Gamma}$, where the equivalent velocity $\boldsymbol{v}_{ref}$ is the velocity in the (x, r) plane at a position close to the tip. The choice of this position is not straightforward, so when using the experimental data the sensitivity of the choice is assessed by determining vref at five positions: (x/R, r/R) = (-0.04, 1.0), two positions with $\Delta r = \pm 0.02R$ and two with $\Delta x = -0.01R$ and $+0.015R$. The variation in the results is shown by the error bars in Fig. 6.1. When using the CFD data, for the same procedure, the position (-0.04, 1.0) is used. Furthermore, the radial load is found by applying a radial momentum balance using the measured velocity field based on a contour as shown in Fig. 6.1, but with $r = R$ as inboard boundary instead of $r = 0.9R$. By doing so, the pressure at the flat tip surface is the source term in the balance giving the radial load. The sensitivity for the choice of the contour is checked by varying the position of the other contour sides. The momentum method is described in del Campo et al. (2014), where it is applied to determine the load on the radial circulation. The results of Fig. 6.7 are integrated along the chord to obtain the normal and radial load given in Table 6.2. Furthermore, the loads as obtained by direct integration of the CFD-calculated pressure are given. The results agree reasonably well, with the pressure integrated radial load deviating most. The ratio of the radial force to the thrust of the blade is 1-2 %, so the contribution of the conservative tip loads to the overall rotor load

	CFD		Experiment	
	P	K–J	K–J	MOM
$\mathscr{N}$	1.2	1.0	1.3 ± 0.3	–
$\mathscr{R}$	1.2	1.8	1.9 ± 0.4	2.2 ± 0.1

Table 6.2: The normal load $\mathscr{N}$ and the radial load $\mathscr{R}$ at the tip, as a percentage of T_{blade}. Here P, K–J and MOM refer to the pressure, Kutta–Joukowsky and momentum methods.

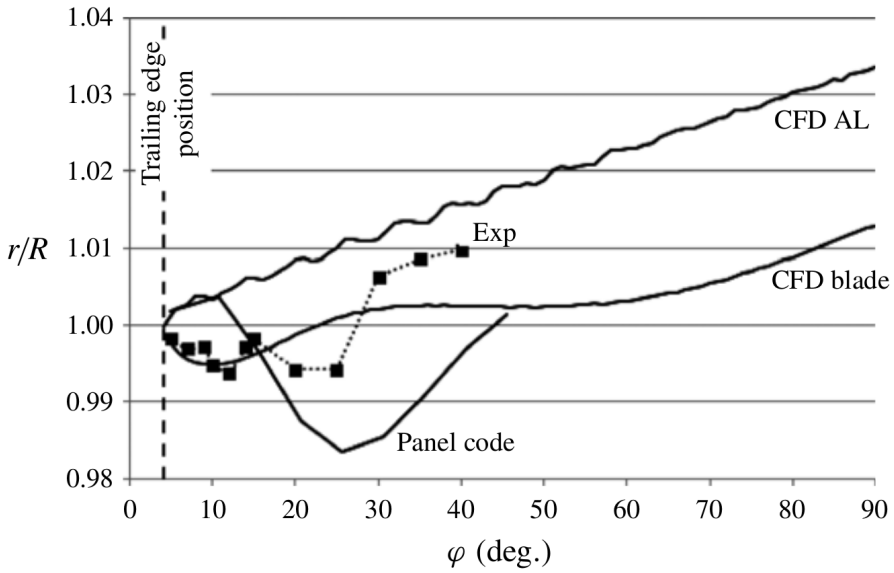

Figure 6.8: The radial coordinate of the tip vortex as a function of the azimuth angle measured from the c/4 position.

is very small. However, when $\mathscr{N}$ and $\mathscr{R}$ are normalized by the thrust acting within the area of this research as defined in Fig. 6.7, the order of magnitude changes to 10 % of the thrust T_{tip} at the blade for $r > 0.9R$. Besides the loads, also the tip vortex trajectories are compared. Figure 6.8 shows the calculated trajectories in comparison with the measured values. The CFD blade results corresponds to the CFD analysis discussed so far; the actuator line (CFD AL) results are presented in the following section. Both CFD results are obtained by taking the average position of 100 streamlines forming the tip vortex. For the panel code, the trajectory is the vorticity filament that leaves the blade at the trailing edge of the tip. Although there are differences between the experimental data and calculated trajectories, the CFD blade and panel code results confirm that the tip vortex moves somewhat inboard before expansion starts after approximately 30° azimuth angle after the c/4 position.

6.3.4 Simulations without chordwise vorticity

Up to now, we have analysed the impact of the conservative radial load on the flow by comparing numerical flow field solutions with and without the radial load. A similar comparison is done here, by comparing the previous CFD results with results obtained by an actuator line analysis using the same code. In an actuator line simulation, the blade is modelled as a line, so all chordwise information is lost like in a lifting line approach. A lifting line models the bound vortex representing the blade bound radial vorticity, whereas the actuator line carries the axial and azimuthal loads of the blade, concentrated at this line. The actuator line is the force field equivalent of the lifting line, and is used often in rotor aerodynamics. The actuator line analysis of this paper uses the same method as explained in Shen et al. (2012). Since all chordwise information is discarded, the bound chordwise vorticity and the loads acting on it are absent. Figure 6.8 shows the comparison of the actuator line simulation (CFD AL) and the simulation for the blade (CFD blade), revealing a clear difference: the wake expansion in CFD AL starts immediately after the tip vortex is released, while this is delayed in CFD blade. The slope of the expansion is the same. When the expansion part of CFD blade is interpolated to $r = R$ keeping the same slope, the equivalent delay in wake expansion compared to CFD AL is 50° azimuth angle.

6.4 Interpretation of the results and conclusions

The conservative forces change the pressure field locally, as they do not influence the boundary conditions at large distances from where they act. The non-conservative forces do so as they perform work and create vorticity. However, conservative forces have an indirect effect on the far field since the modification of the pressure field changes the action of the non-conservative forces. Conservative and non-conservative forces depend in essentially different ways on the geometry of the surface or volume carrying them. The non-conservative forces, like those contributing to thrust and torque, are determined by the radial bound circulation, which can be modelled by lifting line analyses. In such analyses, no geometrical information is necessary once the circulation is defined. In contrast to this, conservative forces do depend on geometry since they vanish for vanishing disc thickness or blade cross-section. Unlike non-conservative forces, they do not behave as a delta function for vanishing thickness or cross-section. This implies that the effect of the conservative forces is of higher order compared to the effect of non-conservative forces.

Since the conservative force field does not convert power nor produce vorticity, it may be discarded from the force field that induces the flow, without violating conservation laws or far-field boundary conditions. The physical origin of the conservative force field is the same as of the non-conservative one, which is the pressure distribution at the rotor blade. When expressed as the load on bound vorticity, there is a clear distinction: in the flow cases studied here, the non-conservative load acts on radial bound vorticity, whereas the conservative load acts on axial disc bound vorticity or azimuthal blade bound vorticity.

The following conclusions can be drawn from this work:

- Force fields representing the action of lifting surfaces having non-zero thickness or chord can be distinguished by non-conservative forces creating vorticity and performing work,

and conservative forces only changing the pressure field.

- A conservative force acts on the chordwise bound vorticity of rotor blades, with a normal and radial component. This force is conservative, unlike the thrust and torque. For a model wind turbine rotor, the chordwise vorticity and the load have been identified by experimental and numerical analyses. The magnitude of the load is 1-2 % of the axial force per blade or ≈ 10 % of the axial force at the tip defined by $r > 0.9R$.

- The CFD and panel code analyses confirm the experimentally observed initial inboard motion of the tip vortex before wake expansion moves it to a larger radius. This happens $\approx 30^\circ$ azimuth angle after the quarter-chord position of the blade tip. An actuator line analysis, which does not account for the conservative load, does not reproduce the inboard motion.

- The conservative component of the force field is taken into account by vortex lattice and CFD methods that model the rotor blade as a surface with dimensions.

- For lifting/actuator line models and analyses based on infinitely thin discs, like the exact solutions of Conway (1998), conservative forces play no role. These models/analyses are unaffected by the results presented here.

Chapter 7

Insight into the role of conservative forces[1]

Abstract The presence of conservative forces on rotor blades is neglected in the blade element theory and all the methods derived from it (like e.g. the blade element momentum theory and the actuator line technique). This might seem a reasonable simplification of the real flow of propellers, helicopters and wind turbine rotors, since conservative loads, by definition, do not contribute to the power conversion. However, as we suggested in a previous work, conservative loads might affect the tip vortex trajectory, which in turn could influence the rotor performance. In the current work we confirm that hypothesis by means of an enhanced actuator line model that is capable of considering the conservative blade loads acting on the chordwise vorticity. We demonstrate that the tip vortex trajectory of a wind turbine rotor is better predicted when the conservative loads are taken into account. Furthermore, the power output seems to be also slightly affected. These results can be relevant for the development of physically-sound blade tip correction models.

7.1 Introduction

The study of the fluid mechanics of propellers dates back to the 19^{th} century. Rankine (1865) and Froude (1889) settled the basis of the momentum theory explaining the origin of propeller thrust and torque from the momentum change in the fluid. This theory defines a limit to the efficiency of an ideal propeller but, due to the fact that this theory is one-dimensional, it does not provide any information about the required propeller geometry. On the contrary, the blade element theory, which is attributed to Froude (1878) and Drzewiecki (1892), takes the rotor geometry into account by dividing each blade into a finite number of independent lifting surfaces (blade elements), although it does not define any limit to the propeller efficiency. This limitation is owed to the lack of consideration of the velocity induction of the propeller itself. In order to overcome the above mentioned drawbacks of both theories, Glauert (1935) introduced the Blade Element Momentum (BEM) theory combining the momentum and the blade element theories. This theory has been successively improved over the years with many corrections that make it an essential tool for rotor design (Hansen and Aagaard Madsen, 2011). It is worth remark-

[1]Submitted for publication as I. HERRÁEZ, D. MICALLEF, G.A.M. VAN KUIK and J. PEINKE: Numerical evidence of the influence of conservative forces on the performance of rotor blades, *Wind Energy Science*, in review.

ing that only fluid loads contributing to the power conversion (i.e. non-conservative loads) are considered in BEM codes (van Kuik et al., 2015; Okulov et al., 2015). The same applies to all other methods relying on the blade element theory. For example, the actuator line method (introduced by Sørensen and Shen, 2002), replaces the momentum theory from the BEM method with the 3D Navier-Stokes equations for obtaining the induced velocities in the rotor plane. However, it also uses the blade element theory for computing the blade loads. Consequently, the actuator line (AL) method, which is gaining much attention in the field of wind farm simulations (Troldborg, 2008; Shives and Crawford, 2013; Nilsson et al., 2015a), disregards the conservative loads. Conservative loads do not contribute to the power conversion and they do not generate vorticity. Gravitational loads are a well known example of that type of load, but part of the load on lifting surfaces might be considered conservative, too (van Kuik et al., 2014). At the root and tip of the blade, the radially oriented bound circulation is deflected towards the chordwise direction before becoming free vorticity. This gives rise to another conservative load, namely the Kutta-Joukowsky force acting on the chordwise bound circulation (van Kuik et al., 2014). This load is contained in a plane normal to the chord, so that it can not contribute to the power conversion. However, it can affect the surface pressure. This article discusses the adequacy of neglecting this type of loads in numerical models making use of the blade element theory.

Currently, rotor models that do not rely on the blade element theory are also widely-used. For instance, Navier-Stokes models based on body-fitted grids have demonstrated to be very useful for the study of rotor aerodynamics (Sørensen et al., 2002; Bechmann et al., 2011; Herráez et al., 2014; Sørensen et al., 2014). Also vortex lattice models have proven to be reliable under attached flow conditions (Micallef et al., 2013). It is worth to recall that these types of models obtain the loads from the pressure field, which makes them capable of considering the conservative loads (in opposition to the AL technique).

In van Kuik et al. (2014) we used an AL, a vortex lattice and body-fitted grid Navier-Stokes model for simulating the same wind turbine like in the present article. The models not relying on the blade element theory predicted a short inboard motion of the tip vortex after release before expansion drives it outboard. This was in agreement with our experimental observations. Further experimental evidence of the same tip vortex behaviour is also available for other wind turbines (Xiao et al., 2011; Micallef, 2012). However, the AL model was unable to predict that behaviour. These results suggest that the conservative radial load acting on the chordwise bound vorticity is responsible for the inboard motion of the tip vortex. Furthermore, as we hypothesized, the change in the tip vortex trajectory might influence the rotor performance. In order to clarify if these hypothesis hold true, in the current work we have extended an AL model for computing and applying automatically the conservative load at the tip. Hence, we aim at answering the following questions by comparing the baseline case (which only considers the non-conservative loads) with the extended model (which also considers the conservative load):

1. Is the conservative load that acts on the chordwise bound circulation truly responsible for the inboard motion of the tip vortex after release?

2. If the previous question is answered affirmatively, is the influence of the mentioned effect on the rotor performance appreciable?

3. Is there any potential to improve the accuracy of AL and BEM models by accounting for

the conservative loads?

Section 7.2 introduces the numerical models that we use in our study. In §7.3 we first verify the reliability of the models and then compare the results of the simulations with and without conservative loads. This allows us to clarify what is the effect of the conservative loads. Finally, in §7.4 we present the main conclusions of this work in relation to our initial research questions.

7.2 Methods

7.2.1 Modelled wind turbine rotor

In this work we use the same experimental results as in van Kuik et al. (2014) for verification purposes. Correspondingly, our study is based on the so called TUDelft-B wind turbine. The two-bladed rotor has a diameter of 2 meters. The blades are twisted and tapered. They make use of the DU96-W-180 airfoil type along the whole span except at the connection to the hub, where the blade section becomes cylindrical. The blade tip is not pointed but rectangular. The wind turbine is operated at its nominal conditions (tip speed ratio $\lambda = 7$). In the experiment the tip vortex trajectory was tracked by means of particle image velocimetry (PIV). Further details about the wind turbine and the experimental set-up can be found in Micallef et al. (2012); Micallef (2012); del Campo et al. (2014).

7.2.2 Numerical model

Navier-Stokes solver

The simulations have been carried out with the open source toolbox OpenFOAM, which consists of a set of C++ libraries for solving partial differential equations (OpenFOAM, 2015). All the computations are of the type Large Eddy Simulation (LES) and make use of a standard Smagorinsky sub-grid scale eddy viscosity model (Smagorinsky, 1963) for modelling the eddies of smaller size than the grid elements. The standard Smagorinky constant was set to $C_s = 0.168$, in accordance to the recommendations for isotropic turbulence (Lilly, 1967; Pope, 2000). The discretization of the governing equations was based on the finite volume method. The time was discretized with a second order backward scheme. For the convective and diffusive terms we used second order linear upwind and linear limited differencing schemes, respectively. The pressure-velocity coupling was accomplished by means of the so called PIMPLE algorithm (OpenFOAM, 2015), which merges the PISO (Issa, 1985) and SIMPLE (Patankar, 1980) algorithms.

Baseline actuator line model

Our implementation of an actuator line (AL) model in OpenFOAM is based on the AL from the SOWFA package (SOWFA, 2015), which in turn is based on the original formulation proposed by Sørensen and Shen (2002). In this kind of model the actual geometry of each blade is substituted by a body force distributed along a line. In order to compute the body force, the actuator line is discretized into a finite number of blade elements. The user must predefine

the blade geometry (spanwise distributions of chord and twist) as well as the aerodynamic characteristics of each blade element as a function of the angle of attack (AoA). Then, the AoA and the local lift $\boldsymbol{F_l}$ and drag $\boldsymbol{F_d}$ forces can be obtained iteratively from the above mentioned predefined data and the velocity field computed by the Navier-Stokes solver. In order to avoid numerical instabilities when applying the actuator line loading to the fluid, a gaussian smearing function is used for converting the point loads of each blade element into volumetric loads. The load applied to the fluid $\boldsymbol{f}$ was computed as:

$$\boldsymbol{f} = \frac{(\boldsymbol{F_l} + \boldsymbol{F_d})}{\varepsilon^3 \pi^{3/2}} exp[-(r/\varepsilon)^2] \tag{7.1}$$

where r is the distance between grid points and blade elements and ε represents a regularization parameter. Previous studies have shown a high dependency of the predicted power on the ε parameter. Therefore, in §7.3.1 we assess the sensitivity of our model to this parameter.
The hub is usually neglected in simulations based on the AL. As a consequence, an unrealistic jet along the centerline of the rotor results. In order to overcome this issue, we modelled the nacelle as a permeable disk area, as described in Wu and Porte-Agél (2010). The force applied by the hub to the fluid is:

$$\boldsymbol{F}_{hub} = -\frac{1}{2}\rho \boldsymbol{u}_\infty^2 A_{hub} C_{D_{hub}} \tag{7.2}$$

where u_∞ is the undisturbed velocity upstream of the hub, A_{hub} is the hub area and $C_{D_{hub}}$ is the hub drag coefficient. In our simulations we assumed $C_{D_{hub}} = 0.85$, as Wu and Porte-Agél (2010) suggested.

The wake induction on the rotor plane is automatically taken into account by the AL and there is no need for considering any correction for the finite number of blades (like e.g. the one proposed by Prandtl, see Glauert, 1935). However, the AL disregards the pressure equalization between the pressure and suction sides of the blade. In order to overcome this limitation, we used the correction model developed by Shen et al. (2005) for accounting for this effect on actuator models (in accordance to the recommendations of Sørensen, 2015, Chapt. 8.7). The correction model applies the following function to the 2D airfoil data:

$$F_1 = \frac{2}{\pi} cos^{-1}\left[exp\left(-g\frac{B(R-r)}{2rsin\phi}\right)\right] \tag{7.3}$$

where B is the number of blades, R is the blade radius, r is the local radial position, ϕ is the flow angle and g is the function

$$g = exp\left(-0.125\left(\frac{B\Omega R}{U_\infty} - 21\right)\right) + 0.1 \tag{7.4}$$

where Ω is the rotational speed and U_∞ is the freestream velocity.

The numerical domain consisted of a square cylinder with a length of 22R and a width of 20R, in accordance to the recommendations of Troldborg (2008). The rotor was placed at a distance of 10R from the inlet. The greatest cell density was concentrated around the rotor. In that region, which has the width 1.6R and the length 4R, the cell size is R/50. Outside that region the grid is progressively stretched towards the outer boundaries. It is worth to recall that a grid resolution with the cell size R/30 in the rotor region is usually considered to be enough for AL

simulations (Shen et al., 2012; Sørensen and Shen, 2002). The reason why a finer resolution was used in our case was to capture the tip vortex trajectory as accurately as possible. For the same reason, 60 blade elements were used for modelling the blade in spite of the fact that 20 elements are usually considered to be enough (Jha et al., 2014). Ivanell et al. (2009) documented that in actuator line simulations the tip vortex is released slightly inboard of the tip. In our experience, this problem is related to the size of the blade elements in that region. Therefore, apart from having a relatively large number of elements, the spacing between elements in our simulation follows a stretching function that allows the element density to increase from the hub towards the blade tip. Jin (2013) also showed that increasing the blade element density at the tip is a computationally efficient manner of improving the simulation accuracy.

A Dirichlet boundary condition was used for the wind speed at the inlet and for the pressure at the outlet. A Neumann condition was set for the pressure at the inlet and for the wind speed at the outlet. At the lateral boundaries of the domain, both the wind speed and the pressure were set to Neumann conditions.

Enhanced actuator line model

The enhanced AL model only differs from the baseline model in the consideration of the conservative load at the blade tip. As we described in van Kuik et al. (2014), the origin of the conservative force is the Kutta-Joukowski load acting on the chordwise bound circulation Γ_{chord}, which is defined as the circulation around a contour normal to the blade chord (see e.g. van Kuik et al., 2014, Fig. 5). Hence, the normal $\mathscr{N}$ and radial $\mathscr{R}$ components of the conservative load are computed as:

$$\mathscr{N} = \rho \cdot V_{radial} \cdot \Gamma_{chord} \cdot c \tag{7.5}$$

$$\mathscr{R} = \rho \cdot V_{axial} \cdot \Gamma_{chord} \cdot c \tag{7.6}$$

where ρ is the fluid density, V_{radial} and V_{axial} are the axial and radial components of the relative velocity, respectively, and c is the chord length. Γ_{chord} is concentrated at the tip (see Fig. 7 and 9 from van Kuik et al., 2014, where the chordwise vorticity and circulation are shown), so it is assumed that $\mathscr{N}$ and $\mathscr{R}$ act only at the last blade element, which has the size $3 \cdot 10^{-4}$R .

In order to obtain Γ_{chord} we need to compute first the radial bound circulation along the span as

$$\Gamma_{radial}(r) = \frac{F_l(r)}{\rho \cdot V_{rel}(r)} \tag{7.7}$$

where F_l and V_{rel} are the sectional lift force the relative wind speed, respectively. Γ_{chord} at the tip can then be easily obtained from the maximum Γ_{radial} assuming conservation of circulation:

$$\Gamma_{chord} = z \cdot max(\Gamma_{radial}(r)) \tag{7.8}$$

where z is a factor between 0 and 1 accounting for the fact, that a fraction of the maximum circulation is released as trailing circulation along the blade span (see van Kuik et al., 2014, Fig. 9). We assume $z = 0.75$, since as Fig. 9 from van Kuik et al. (2014) shows, only about 25% of the bound circulation is radially oriented at the quarter chord position of the blade tip. We expect this value to be highly dependent on the blade geometry and the operating tip speed ratio.

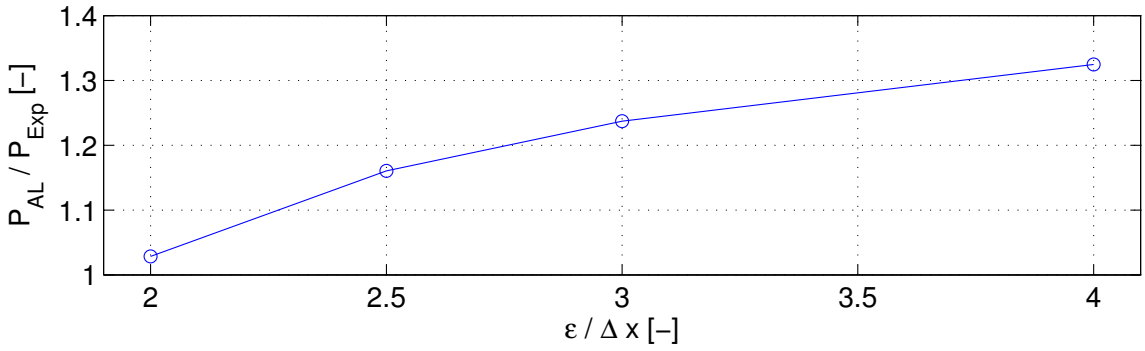

Figure 7.1: Sensitivity of the computed power (normalized with the experimental results) to the ratio between the regularization parameter ε and the cell length Δx.

7.3 Results

7.3.1 Verification of the baseline numerical model

It is well known that the accuracy of AL models highly depends on the regularization parameter ε. As Ivanell et al. (2009) reported, ε must be as small as possible in order to avoid influencing the wake structure with the Gaussian smearing of the body force. However, the ratio $\varepsilon/\Delta x$ (where Δx is the cell size in the rotor plane) can not be too small if numerical instabilities are to be avoided. Therefore, in order to achieve a small ε and resolve accurately the tip vortex, we chose in the first place a mesh that clearly exceeds the usual requirements of actuator line simulations (see §7.2.2). The power obtained from the simulations is used for analysing the sensitivity of the numerical model to the the ratio $\varepsilon/\Delta x$. The best consistency with the experiment (power overprediction of just 3%) is achieved with $\varepsilon/\Delta x = 2$ (i.e. $\varepsilon = R/25$). Troldborg (2008) also suggested the same ratio as the best compromise between simulation accuracy and stability. For smaller values of $\varepsilon/\Delta x$ the simulation was too unstable. Therefore we selected $\varepsilon/\Delta x = 2$ as baseline for our study.

As we explained in §7.2.2, the axial and radial velocity components are required for computing the conservative load that acts on the chordwise vorticity. Figure 7.2 shows those velocity components at the rotor plane as predicted by two different models: the current AL model and the RANS model with body-fitted mesh that was validated in van Kuik et al. (2014).

In spite of the fact that modelling a 3D blade by means of a 1D line is a strong simplification, the agreement between the AL and the body-fitted RANS model is in general very satisfactory for both the axial and radial velocity components. However, a shift can be seen in the azimuthal position of the region with high radial velocity close to the blade tip. This implies that the radial velocity at the tip of the actuator line is strongly underpredicted. As a consequence, the normal component of the conservative load $\mathscr{N}$ is also completely underestimated (see table 7.1). However, the radial component $\mathscr{R}$ is very accurately predicted.

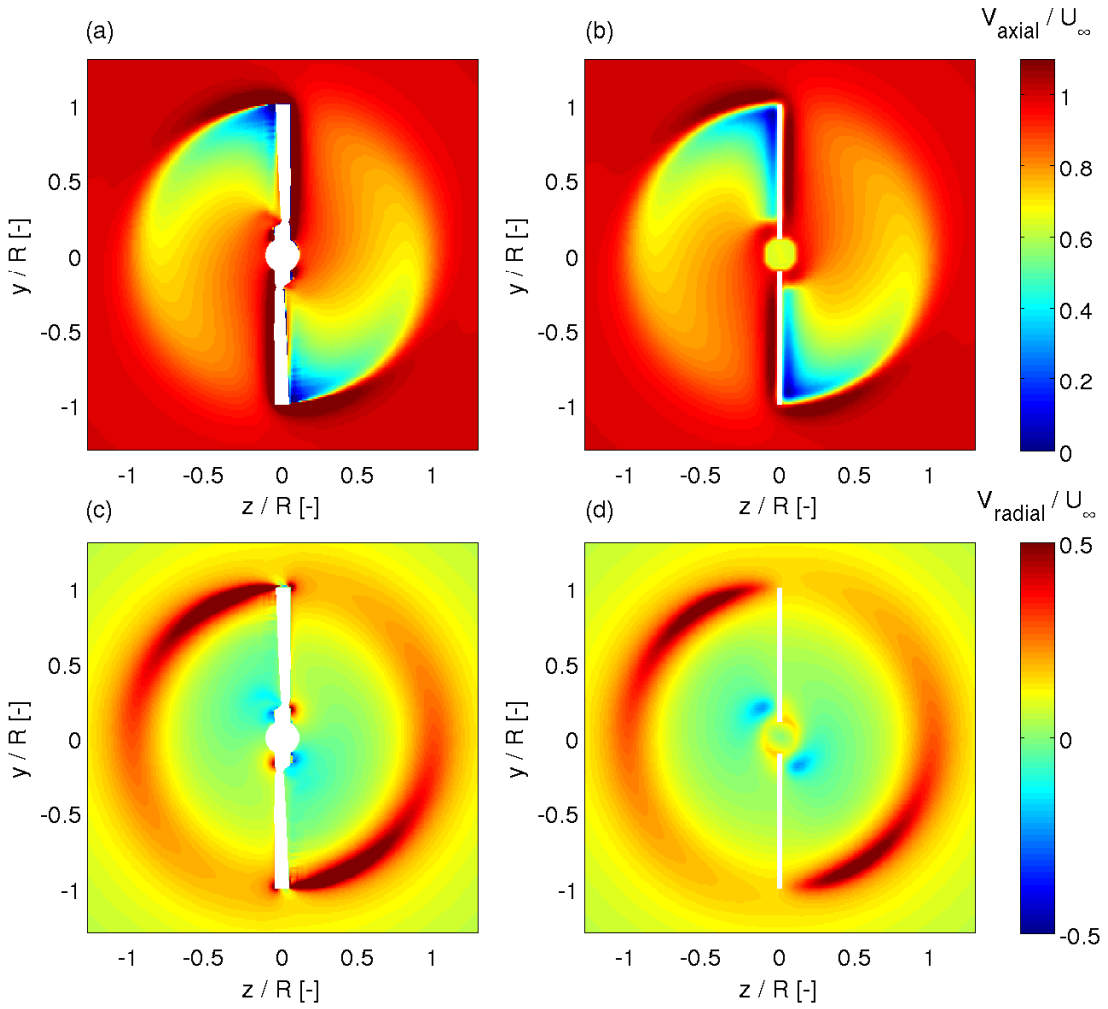

Figure 7.2: Velocity at the rotor plane: (a) V_{axial} from the body-fitted RANS simulation, (b) V_{axial} from the AL-LES simulation, c) V_{radial} from the body-fitted RANS simulation and (d) V_{radial} from the AL-LES simulation. The white surface in the results from the body-fitted RANS simulation represents the intersection of the rotor plane with the blades and nacelle. The white lines in the results from the AL-LES simulation represent the actuator lines.

	Body-fitted RANS	$AL_{baseline}$	$AL_{enhanced}$
$\mathscr{N}$	1.2	0	0.03
$\mathscr{R}$	1.2	0	1.2

Table 7.1: Normal and radial loads ($\mathscr{N}$ and $\mathscr{R}$, respectively) at the tip, as a percentage of the blade thrust. The body-fitted RANS results were obtained from the model presented in van Kuik et al. (2014) and they were calculated by surface pressure integration.

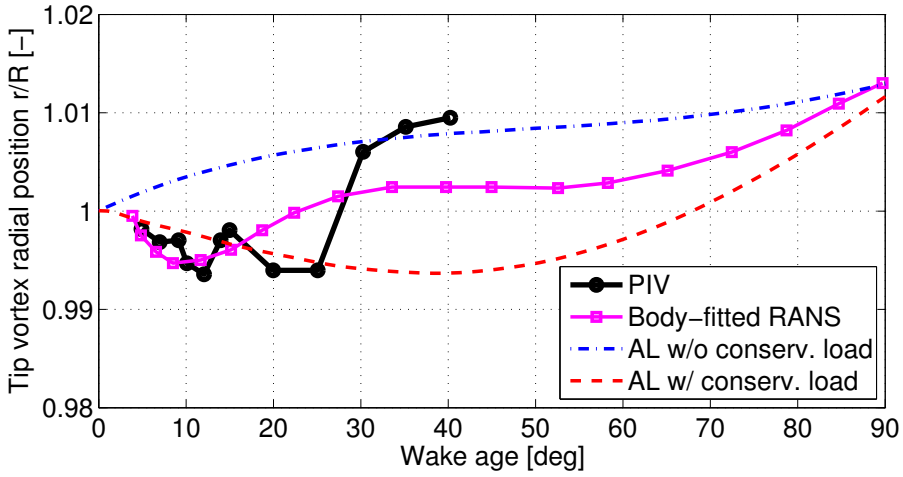

Figure 7.3: Radial position of the tip vortex as a function of the wake age. Experimental and different types of numerical results are compared.

7.3.2 Influence of the conservative load on the tip vortex trajectory

The λ_2 criteria (Jeong and Hussain, 1995) has been used for identifying the location of the vortex core at each azimuthal position. Figure 7.3 shows the vortex trajectory obtained from the experiment and different numerical models. Our analysis focuses on the AL-LES simulations, since the other results were already analysed in van Kuik et al. (2014). The AL-LES simulations without conservative load (labelled as *AL w/o conserv. load*) lead to the wake beginning to expand directly after the tip vortex release. On the contrary, the AL-LES simulations with conservative load (labelled as *AL w/ conserv. load*) present an inboard motion of the tip vortex prior to the wake expansion (as it also occurs in the experiment, the body-fitted RANS and panel lattice simulations). Furthermore, the computed radial position of the tip vortex at its innermost location agrees very well with the experiment and the body-fitted RANS simulations. This behaviour confirms that the conservative load $\mathscr{R}$ is responsible for the inboard motion of the tip vortex, as was hypothesized in van Kuik et al. (2014). However, the azimuthal angle at which the wake expansion begins is clearly delayed in the AL-LES simulation. The reason for this seems to be related to the strong underestimation of $\mathscr{N}$ (see table 7.1).

7.3.3 Influence of the conservative load on the rotor performance

In this section we aim at analysing if the influence of the conservative force on the tip vortex trajectory plays a role on the rotor performance. Figure 7.4-a shows the AoA in the tip region. No significant difference between the results with and without conservative force can be seen. This implies that the lift and drag force coefficients (C_l and C_d) are not changed. However, the relative wind speed (Figure 7.4-b), which is defined as $V_{rel} = \sqrt{V_x^2 + V_\theta^2}$, is slightly affected by the change in the vortex trajectory. Correspondingly, the lift and drag forces F_l and F_d are also influenced (Figures 7.4-c and 7.4-d, respectively). This, in turn has a small but distinguishable

effect on the driving torque and the thrust (Figures 7.4-e and 7.4-f, respectively). Integrating the torque over the last 10% of the blade gives a difference of the torque at the tip with and without conservative load of approx. 2%. The total power of the turbine is reduced by approx. 1%. This contributes to mitigate the slight power overprediction of the simulation as compared to the experiment (see Figure 7.1). This confirms that the conservative loads play an indirect role on the rotor performance that should not be neglected if high order effects are to be considered.

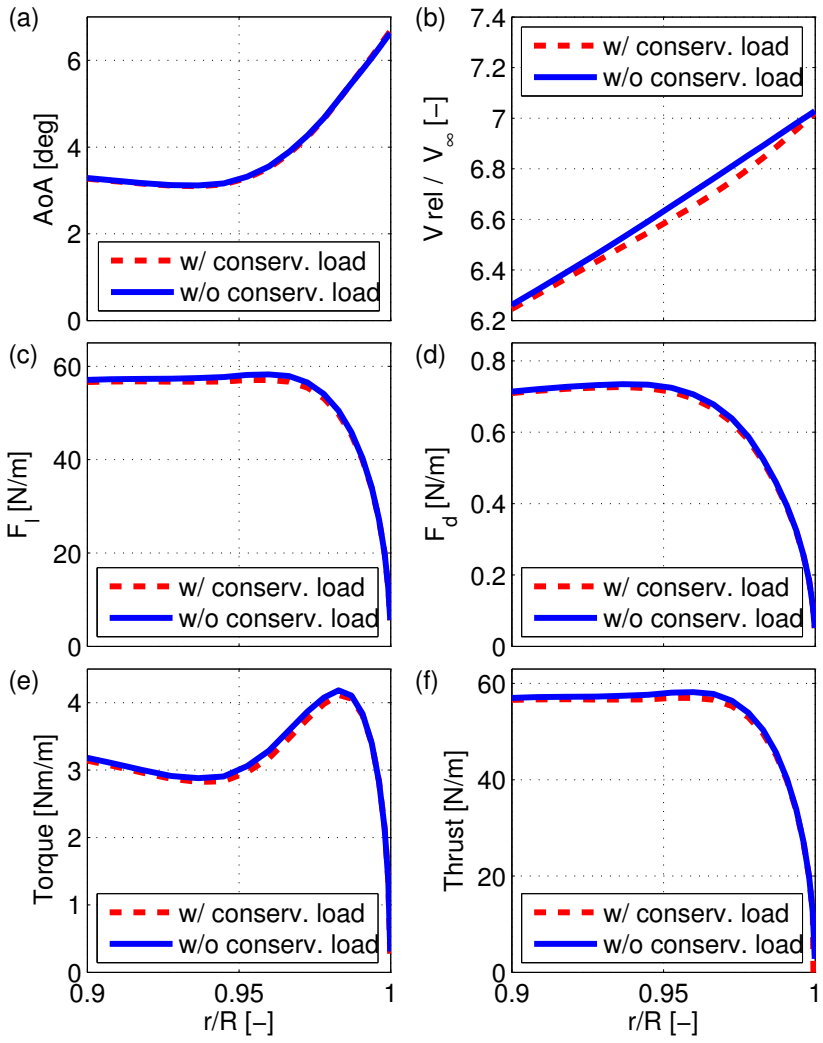

Figure 7.4: Influence of the conservative force on the spanwise distribution of (a) angle of attack AoA, (b) relative velocity V_{rel}, (c) sectional lift force F_l, (d) sectional drag force F_d, (e) sectional torque and (f) sectional thrust.

7.4 Conclusions

The use of an enhanced actuator line model capable of applying conservative loads to the fluid allowed us to gain insight into the role of those loads on the rotor performance. The agreement of the model with experimental results and other numerical models representing the true geometry of the blade was in general satisfactory. However, the prediction of the radial wind velocity component should be improved for obtaining a realistic normal component of the conservative force. The initial research questions have been successfully addressed:

- The conservative load acting on the chordwise bound circulation of a wind turbine blade is confirmed to cause an inboard motion of the tip vortex after release and prior to the wake expansion.
- The influence of the conservative load on the tip vortex trajectory seems to play a small but noticeable role on the power output. Its consideration helped to improve the consistency with the experimental results. However, it must be kept in mind that this is a higher order effect and correspondingly the numerical uncertainty might play a substantial role. Furthermore, the effect is assumed to be very dependent on the blade geometry.
- The consideration of conservative loads on tip loss correction models is recommended if high order effects are to be considered.

Chapter 8

Conclusions

This work has addressed the study of the aerodynamics of wind turbines by means of Computational Fluid Dynamics (CFD) simulations. Special attention has been paid to the aerodynamics of the blade root and tip regions, where the flow is highly three-dimensional and strongly influenced by the trailing vortices. The simulations of several wind turbines have been extensively validated against experimental results from model turbines operating under controlled conditions in a wind tunnel. The Reynolds Averaged Navier-Stokes (RANS) models were proven to be suitable for the prediction of the flow around the blades and in the near wake. However, the accuracy of this method was found to be reduced at stall conditions, since the models tended to underpredict the flow separation. Large Eddy Simulations (LES) have also been performed within this thesis. However, their use was restricted to actuator line simulations, since the required number of cells for solving the true blade geometry with boundary layer would be far too large for the available computational resources. The actuator line LES simulations were especially useful for the study of the tip vortex trajectory and evolution.

It has been shown that the blade inboard region is very prone to the presence of strong spanwise flows, especially in areas where the chordwise velocity is low. Furthermore, both attached and separated flows can present significant radial flows. According to our results, the origin of these flows is not the existence of spanwise pressure gradients, as some authors have suggested, but the centrifugal force acting on the boundary layer. The radial flows are also affected by the Coriolis force, which "pushes" the flow towards the trailing edge. As a consequence, the adverse pressure gradient on the suction side is reduced, what leads to the delay of stall and the enhancement of lift. This phenomenon, which is known as Himmelskamp effect, did not play any significant role on the drag of the turbines studied in this thesis. This is in contrast to other wind turbines documented in the literature, where the drag was increased or even reduced under the influence of the mentioned effect. The impact of the Himmelskamp effect on the C_p distribution seems to be very dependant on the airfoil geometry. The resulting C_p distribution disparities between different airfoil types are not only quantitative, but also qualitative. This can be a major issue for the development of generalized correction models.

Another achievement of this thesis has been the correct prediction of trailing vortices in the transition regions between airfoils of substantially different aerodynamic characteristics. As it has been shown, those trailing vortices can disrupt the radial flows and correspondingly also the Himmelskamp effect. This is also a serious challenge for the development of reliable correction models for this effect.

It has also been shown that the bound vorticity is oriented radially along most of the blade span except at the tip and the root, where it is deflected towards the chordwise direction. Indeed, the chordwise bound vorticity is the origin of the tip and root trailing vortices. The change from spawise to chordwise bound vorticity is much more gradual at the root than at the tip and so are also the aerodynamic losses. This effect is most probably very dependant on the root and tip geometry and it should be accounted for in the engineering correction models for aerodynamic losses. Another consequence of this effect is that the root vortex does not present a well defined, distinctive structure. Furthermore, it has also been shown that the vortex trailed from the spanwise position of maximum chord length rotates in the opposite direction of the root vortex. This explains the fast diffusion of the root vortex reported in many experiments.

The physical origin of the loads acting on the chordwise and the radial bound vorticity is the same in both cases: pressure distributions on the blade surface. However, the load acting on the radial vorticity is orthogonal to the blade radius and the load acting on the chordwise vorticity is orthogonal to the blade chord. Hence, the load from the radial vorticity can produce work (i.e. contribute to the power conversion) and the load from the chordwise vorticity can not do it. The former is therefore a non-conservative load and the latter is a conservative load. Conservative forces are always disregarded in the calculation methods based on the blade element theory (e.g. in blade element momentum and actuator line models). However, in this work an actuator line model capable of computing and applying automatically the conservative load has been developed. The comparison between simulations with and without conservative load allowed to conclude that the conservative load can modify the blade tip trajectory. Indeed, the existence of that force explains the observations from several experiments, where the tip vortex presents an inboard motion just after release from the blade tip and before the wake expansion drives it outboard. The change in the tip vortex trajectory has been shown to influence slightly the power conversion. Therefore, engineering models can be improved if the conservative tip load is included. A similar effect is expected at the root. However, the relevance of this root effect is probably negligible owing to the much stronger Himmelskamp effect and to the comparatively low impact of the root forces on the power conversion.

These results show the great potential of CFD for the study of wind turbine aerodynamics. Furthermore, they pave the way for a better characterization of the blade flow. Ultimately, this should contribute to reduce the uncertainty in the design process of wind turbines and hence to improve the cost-effectiveness of wind energy.

Chapter 9

Future work

This work has given insight into several aerodynamic phenomena affecting the blade tip and root of wind turbines by means of CFD simulations. Many of the limitations of the current results could be addressed in a future work:

- *Use of Reynolds Stress Models (RSM) for modelling the turbulence*: The turbulence models used in this thesis are based on the Boussinesq approximation. One of the drawbacks of this method is the assumption of isotropic turbulence in the boundary layer. This is a strong simplification and in the case of highly three-dimensional flows it can affect the simulation accuracy. Therefore, the use of more advanced Reynolds Stress Models is recommended.

- *Development of correction models*: The final goal of the flow characterization is the implementation of reliable models. Hints and advices have been given for the development of correction models. This is however by no means a finished task and it should be continued. There is still a long way to go until the physical mechanisms of the blade flow are sufficiently well understood for developing reliable corrections.

- *Determination of the angle of attack*: The determination of the angle of attack is one of the main sources of uncertainty in the characterization of the blade aerodynamics. Further efforts should be performed for the development of reliable methods to compute and measure it.

- *Sensitivity to blade geometry and airfoil type*: the geometry of the tip and root as well as the used airfoil type are expected to play a decisive role in the aerodynamic effects studied in this thesis. The sensitivity to both factors should therefore be analysed in detail.

- *Sensitivity to Reynolds number*: the range of Reynolds number considered in this work is one order of magnitude lower than in full scale wind turbines. Therefore, its influence on the studied effects should be analysed.

- *Sensitivity to turbulence*: all the results presented in this work were based on laminar inflow. This assumption was necessary for isolating the studied effects from other influences and for validating the simulations against available wind tunnel measurements. However, full scale wind turbines operate under the influence of turbulence. Therefore, its role should be analysed.

- *Other aspects of the root and tip flow*: Many aspects of the tip and root flow deserve more attention. As an example, the effect of the finite number of blades, the tip losses caused by the pressure equalization between the blade upper and lower sides, the interaction between root losses and Himmelskamp effect, the transition from laminar to turbulent flow, etc. should be studied in more depth.

- *Transient aerodynamic effects*: The study of transient aerodynamic effects was out of the scope of this thesis. However, they could be addressed in a future work. Examples of such effects include dynamic stall, dynamic inflow, tower shadow, etc.

Bibliography

Akay, B., C. J. Ferreira, G. J. van Bussel, and I. Herráez
2012a. Experimental and numerical quantification of radial flow in the root region of a hawt. In *50th AIAA Aerospace Sciences Meeting*, Nashville, TN.

Akay, B., D. Micallef, C. J. Ferreira, and G. van Bussel
2012b. Effects of geometry and tip speed ratio on the HAWT blade's root flow. In *Proceedings of the Science of Making Torque from Wind 2012*, Oldenburg, Germany.

Akay, B., D. Ragni, C. Simão Ferreira, and G. van Bussel
2014. Experimental investigation of the root flow in a horizontal axis wind turbine. *Wind Energy*, 17(7):1093–1109.

Bak, C., J. Johansen, and P. Andersen
2006. Three–dimensional corrections of airfoil characteristics based on pressure distributions. In *2006 European Wind Energy Conference Scientific Proceedings*, Athens, Greece.

Banks, W. and G. Gadd
1963. Delaying effect of rotation on laminar separation. *AIAA Journal*, 1(4):941–942.

Bechmann, A., N. N. Sørensen, and F. Zahle
2011. CFD simulations of the MEXICO rotor. *Wind Energy*, 14(5):677–689.

Bertagnolio, F., N. Sørensen, J. Johansen, and P. Fuglsang
2001. Wind turbine airfoil catalogue. Technical Report Risø–R–1280, Risø, Risø National Laboratory, Roskilde, Denmark.

Boorsma, K. and J. Schepers
2003. Description of experimental setup. MEXICO measurements. Technical Report ECN–X–09–0XX, ECN, Petten, Netherlands.

Breton, S.-P., F. N. Coton, and G. Moe
2008. A study on rotational effects and different stall delay models using a prescribed wake vortex scheme and NREL phase VI experiment data. *Wind Energy*, 11(5):459–482.

Carrion, M., M. Woodgate, R. Steijl, G. Barakos, S. Gomez-Iradi, and X.Munduate
2012. Cfd and aeroelastic analysis of the mexico wind turbine. In *Proceedings of the Science of Making Torque from Wind 2012*, Oldenburg, Germany.

Chaviaropoulos, P. K. and M. O. L. Hansen
2000. Investigating three–dimensional and rotational effects on wind turbine blades by means of a quasi–3D Navier-Stokes solver. *Journal of Fluids Engineering*, 122(2):330–336.

Constantinides, Y. and O. Oakley
2006. Numerical prediction of bare and straked cylinder VIV. In *Proceedings from 25th International Conference on Offshore Mechanics and Arctic Engineering, OMAE2006*, Hamburg, Germany.

Conway, J. T.
1998. Exact actuator disc solutions for non-uniform heavy loading and slipstream contraction. *Journal Fluid Mechanics*, 365:235–267.

Corrigan, J. and H. Schillings
1994. Empirical model for stall delay due to rotation. In *Proceedings of the American Helicopter Society Aeromechanics Specialists Conference 1994*, San Francisco, CA.

Corten, G.
2001. *Flow Separation on Wind Turbine Blades*. PhD thesis, University of Utrecht.

de Villiers, E.
2006. *The Potential of Large Eddy Simulation for the Modelling of Wall Bounded Flows*. PhD thesis, Imperial College London.

del Campo, V., D. Ragni, D. Micallef, B. Akay, F. J. Diez, and C. S. Ferreira
2014. 3D load estimation on a horizontal axis wind turbine using SPIV. *Wind Energy*, 17(11):1645–1657.

Drzewiecki, S.
1892. *Bulletin de L'Association Technique Maritime, Paris*.

Du, Z. and M. Selig
1998. A 3D stall-delay model for horizontal axis wind turbine prediction. In *Proceedings of 1998 ASME Wind Energy Symposium*, number AIAA-98-0021, Reno, NV, USA.

Du, Z. and M. Selig
2000. The effect of rotation on the boundary layer of a wind turbine blade. *Renewable Energy*, 20(2):167 – 181.

Dumitrescu, H. and V. Cardos
2004. Rotational effects on the boundary-layer flow in wind turbines. *AIAA Journal*, 42(2):408–411.

Duque, E. P. N., M. D. Burklund, and W. Johnson
2003. Navier-Stokes and comprehensive analysis performance predictions of the NREL Phase VI experiment. *Journal of Solar Energy Engineering*, 125(4):457–467.

Duque, E. P. N., C. van Dam, and S. Hughes
1999. Navier-Stokes simulations of the NREL combined experiment Phase II rotor. In *Proceedings 1999 ASME Wind Energy Symposium*, number AIAA-99-0037, Pp. 143–153, Reno, NV.

Ebert, P. and D. Wood
2001. The near wake of a model horizontal–axis wind turbine: Part 3: properties of the tip and hub vortices. *Renewable Energy*, 22(4):461 – 472.

Ferrer, E. and X. Munduate
2007. Wind turbine blade tip comparison using cfd. *Journal of Physics: Conference Series*, 75(012005).

Ferziger, J. and M. Peric
2002. *Computational methods for fluid dynamics*. Springer.

FLOW
2015. Facility for Large-scale COmputations in Wind Energy Research. http://www.fk5.uni-oldenburg.de/57249.html. Accessed: October 2015.

Froude, R.
1889. On the part played in propulsion by differences of fluid pressure. *Transactions Institute of Naval Architects*, 30:390–405.

Froude, W.
1878. *Transactions Institute of Naval Architects*, 19:47.

Germano, M., U. Piomelli, and P. W. Cabot
1991. A dynamic subgrid-scale eddy viscosity model. *Physics of Fluids A*, 3(7):1760–1765.

Glauert, H.
1935. The general momentum theory. In *Aerodynamic Theory*, W. Durand, ed., volume IV. Division L. Springer. Reprinted 1963 Dover.

Guntur, S., C. Bak, and N. Sørensen
2011. Analysis of 3D stall models for wind turbine blades using data from the MEXICO experiment. In *Proceedings of 13th International Conference on Wind Engineering*, Amsterdam, The Netherlands.

Guntur, S. and N. Sørensen
2012. An evaluation of several methods of determining the local angle of attack on wind turbine blades. In *Proceedings of the Science of Making Torque from Wind 2012*, Oldenburg, Germany.

Guntur, S. and N. N. Sørensen
2014. A study on rotational augmentation using cfd analysis of flow in the inboard region of the mexico rotor blades. *Wind Energy*.

Haans, W., G. van Kuik, and G. van Bussel
2008. The inverse vortex wake model:a measurement analysis tool. *Journal of Solar Energy Engineering*, 130(3):031009–031009–14.

Hand, M., D. Simms, L. Fingersh, D. Jager, J. Cotrell, S. Schreck, and S. Larwood
2011. Unsteady aerodynamics experiment phase vi: wind tunnel test configurations and available data campaigns. Technical Report NREL/TP-500-29955, Risø, National Renewable Laboratory.

Hansen, M., N. Sørensen, J. Sørensen, and J. Michelsen
1997. Extraction of lift, drag and angle of attack from computed 3D viscous flow around a rotating blade. In *Scientific Proceedings from European Wind Energy Conference, EWEC'97*, Pp. 499–501, Dublin, Ireland.

Hansen, M. L. and H. Aagaard Madsen
2011. Review paper on wind turbine aerodynamics. *Journal of Fluids Engineering*, 133(11):114001–114001–12.

Herráez, I., B. Stoevesandt, and J. Peinke
2014. Insight into rotational effects on a wind turbine blade using Navier–Stokes computations. *Energies*, 7(10):6798–6822.

Himmelskamp, H.
1947. *Profile investigations on a rotating airscrew*, Reports and translations. Völkenrode MAP.

Issa, R. I.
1985. Solution of the implicitly discretized fluid flow equations by operator-splitting. *Journal of Computational Physics*, 62:40–65.

Ivanell, S., J. Sørensen, R. Mikkelsen, and D. Henningson
2007. Numerical analysis of the tip and root vortex position in the wake of a wind turbine. *Journal of Physics: Conference Series*, 75(012035).

Ivanell, S., J. N. Sørensen, R. Mikkelsen, and D. Henningson
2009. Analysis of numerically generated wake structures. *Wind Energy*, 12(1):63–80.

Jeong, J. and F. Hussain
1995. On the identification of a vortex. *Journal of Fluid Mechanics*, 285:69–94.

Jha, P. K., M. J. Churchfield, P. J. Moriarty, and S. Schmitz
2014. Guidelines for volume force distributions within actuator line modeling of wind turbines on Large-Eddy Simulation-type grids. *J. Sol. Energy Eng.*, 136(3):031003–031003–11.

Jin, W.
2013. Numerical simulation of wind turbine wakes based on actuator line method in NEK5000. Master's thesis, KTH, Sweden.

Johansen, J. and N. N. Sørensen
2004. Aerofoil characteristics from 3D CFD rotor computations. *Wind Energy*, 7(4):283–294.

Johansen, J., N. N. Sørensen, J. A. Michelsen, and S. Schreck
2002. Detached-eddy simulation of flow around the NREL Phase VI blade. *Wind Energy*, 5(2-3):185–197.

Jonkman, J., S. Butterfield, W. Musial, and G. Scott
2009. Definition of a 5 mw reference wind turbine for offshore system development. Technical Report NREL/TP-500-38060, NREL, Golden, CO, USA.

Kwon, S., J. Cho, J. Park, and H. Choi
2002. The effects of drag reduction by ribbons attached to cylindrical pipes. *Ocean Engineering*, 29(15):1945–1958.

Laizet, S. and J. C. Vassilicos
2011. Dns of fractal generated turbulence. *Flow, turbulence and combustion*, 87:673–705.

Launder, B., G. Reece, and W. Rodi
1975. Progress in the development of a Reynolds stress turbulence closure. *Journal of Fluid Mechanics*, 68:537–566.

Launder, B. and D. Spalding
1974. The numerical computation of turbulent flows. *Computer Methods in Applied Mechanics and Engineering*, 3:269–289.

Le Pape, A. and J. Lecanu
2004. 3D Navier–Stokes computations of a stall–regulated wind turbine. *Wind Energy*, 7(4):309–324.

Leishman, J. G.
2002. Challenges in modelling the unsteady aerodynamics of wind turbines. *Wind Energy*, 5(2-3):85–132.

Lilly, D. K.
1967. The representation of small–scale turbulence in numerical simulation experiments. In *Proc. IBM Scientific Computing Symposium on Environmental Sciences*.

Lindenburg, C.
2003. Investigation into rotor blade aerodynamics. Technical Report ECN-C03-025, ECN, Petten, Netherlands.

Massouh, F. and I. Dobrev
2007. Exploration of the vortex wake behind of wind turbine rotor. *Journal of Physics: Conference Series*, 75(012036).

McCroskey, W. and P. Yaggy
1968. Laminar boundary layers on helicopter rotors in forward flight. *AIAA Journal*, 6(10):1919–1926.

Medici, D. and P. H. Alfredsson
2006. Measurements on a wind turbine wake: 3D effects and bluff body vortex shedding. *Wind Energy*, 9(3):219–236.

Menter, F.
1993. Zonal two equation k–ω turbulence models for aerodynamic flows. *AIAA Journal*, 93(2906).

Menter, F.
1994. Two–equation eddy-viscosity turbulence models for engineering applications. *AIAA Journal*, 32(8):1598–1605.

Micallef, D.
2012. *3D flows near a HAWT rotor: A dissection of blade and wake contributions*. PhD thesis, Delft University of Technology.

Micallef, D., B. Akay, C. S. ao Ferreira, T. Sant, and G. van Bussel
2012. The origins of a wind turbine tip vortex. In *Proceedings of the Science of Making Torque from Wind 2012*, Oldenburg, Germany.

Micallef, D., G. van Bussel, C. S. a. Ferreira, and T. Sant
2013. An investigation of radial velocities for a horizontal axis wind turbine in axial and yawed flows. *Wind Energy*, 16(4):529–544.

Mockett, C.
2009. *A comprehensive study of detached-eddy simulation*. PhD thesis, Technical University of Berlin.

Nilsson, K., W. Z. Shen, J. N. Sørensen, S. P. Breton, and S. Ivanell
2015a. Validation of the actuator line method using near wake measurements of the MEXICO rotor. *Wind Energy*, 18(3):499–514.

Nilsson, K., W. Z. Shen, J. N. Sørensen, S.-P. Breton, and S. Ivanell
2015b. Validation of the actuator line method using near wake measurements of the mexico rotor. *Wind Energy*, 18(9):1683–1683.

Okulov, V. L., J. N. Sørensen, and D. H. Wood
2015. The rotor theories by Professor Joukowsky: Vortex theories. *Progress in Aerospace Sciences*, Pp. 19–46.

OpenFOAM
2015. OpenFOAM: the open source CFD toolbox. www.openfoam.com. Accessed: October 2015.

Pascal, L.
2009. Analysis of MEXICO Measurements. Technical Report ECN-Wind Memo-09-010, ECN, Petten, Netherlands.

Patankar, S. V.
1980. *Numerical Heat Transfer and Fluid Flow*. Taylor & Francis.

Pointwise
2015. Pointwise. www.pointwise.com. Accessed: October 2015.

Pope, S. B.
2000. *Turbulent flows*. Cambridge University Press.

Raj, N.
2000. An improved semi–empirical model for 3D post–stall effects in horizontal axis wind turbines. Master's thesis, University of Illinois, Urbana–Champaign.

Rankine, W. J. M.
1865. On the mechanical principles of the action of propellers. *Transactions Institute of Naval Architects*, 6:13–39.

Réthoré, M., F. Zahle, N. Sørensen, and A. Bechmann
2011. CFD simulations of the mexico wind tunnel and wind turbine. In *Proceedings of EWEA 2011*, Brussels, Belgium.

Roache, P. J.
1994. Perspective: A method for uniform reporting of grid refinement studies. *Journal of Fluids Engineering*, 116(3):405.

Roache, P. J.
1998a. *Perspective: A Method for Uniform Reporting of Grid Refinement Studies*, Pp. 8–9. Hermosa Publishers.

Roache, P. J.
1998b. *Perspective: A Method for Uniform Reporting of Grid Refinement Studies*, Pp. 8–9. Hermosa Publishers.

Robinson, M., M. Hand, S. Simms, and S. Schreck
1999. Horizontal axis wind turbine aerodynamics: Three–dimensional, unsteady, and separated flow influences. In *Proceedings of FEDSM99*, number FEDSM99-S295-01, San Francisco, CA.

Ronsten, G.
1992. Static pressure measurements on a rotating and a non-rotating 2.375 m wind turbine blade. comparison with 2D calculations. *Journal of Wind Engineering and Industrial Aerodynamics*, 39(1–3):105–118.

Rung, T., H. Lübcke, and F. Thiele
2001. Universal wall-boundary conditions for turbulence-transport models. *ZAMM - Journal of Applied Mathematics and Mechanics / Zeitschrift für Angewandte Mathematik und Mechanik*, 81(S3):481–482.

Schepers, J.
2012. *Engineering models in wind energy aerodynamics*. PhD thesis, TU-Delft.

Schepers, J., K. Boorsma, T. Cho, S. Gomez-Iradi, A. Schaffarczyk, A. Jeromin, W. Shen, T. Lutz, K. Meister, B. Stoevesandt, S. Schreck, D. Micallef, R. Pereira, T. Sant, H. Madsen, and N. Sørensen
2012. Final report of iea task 29, mexnext (phase 1): Analysis of mexico wind tunnel measurements. Technical Report ECN–E–12–004, ECN, KARI, CENER, CEWind EG, DTU, University of Stuttgart, ForWind, NREL, TUDelft, RISØ.

Schepers, J., K. Boorsma, C. Kim, and T. Cho
2011. Analysis of detailed aerodynamic measurements on a 4.5 m diameter rotor placed in the large german dutch wind tunnel DNW. In *Proceedings of EWEA 2011*, Brussels, Belgium.

Schepers, J. and H. Snel
2007. Model experiments in controlled conditions, final report. Technical Report ECN-E-07-042, ECN, Petten, Netherlands.

Schmidt, T., C. Mockett, and F. Thiele
2009. Adaptive wall function for the prediction of turbulent flows. In *MEGADESIGN and MegaOpt - German Initiatives for Aerodynamic Simulation and Optimization in Aircraft Design*, N. Kroll, D. Schwamborn, K. Becker, H. Rieger, and F. Thiele, eds., volume 107 of *Notes on Numerical Fluid Mechanics and Multidisciplinary Design*, Pp. 21–33. Springer Berlin Heidelberg.

Schreck, S. and M. Robinson
2002. Rotational augmentation of horizontal axis wind turbine blade aerodynamic response. *Wind Energy*, 5(2-3):133–150.

Schreck, S., T. Sant, and D. Micallef
2010. Rotational augmentation disparities in the mexico and UAE phase vi experiments. In *Proceedings of the Science of Making Torque from Wind 2010*, Heraklion, Crete, Greece.

Schreck, S. J., N. N. Sørensen, and M. C. Robinson
2007. Aerodynamic structures and processes in rotationally augmented flow fields. *Wind Energy*, 10(2):159–178.

Shen, W. Z., M. O. L. Hansen, and J. N. Sørensen
2009. Determination of the angle of attack on rotor blades. *Wind Energy*, 12(1):91–98.

Shen, W. Z., J. N. Sørensen, and R. Mikkelsen
2005. Tip loss correction for actuator/Navier–Stokes computations. *Journal of Solar Engineering*, 127:209–213.

Shen, W. Z., W. J. Zhu, and J. N. Sørensen
2012. Actuator line/Navier–Stokes computations for the MEXICO rotor: comparison with detailed measurements. *Wind Energy*, 15(5):811–825.

Sherry, M., J. Sheridan, and D. Jacono
2013. Characterisation of a horizontal axis wind turbine's tip and root vortices. *Experiments in Fluids*, 54(3).

Shives, M. and C. Crawford
2013. Mesh and load distribution requirements for actuator line CFD simulations. *Wind Energy*, 16(8):1183–1196.

Sicot, C., P. Devinant, S. Loyer, and J. Hureau
2008. Rotational and turbulence effects on a wind turbine blade. investigation of the stall mechanisms. *Journal of Wind Engineering and Industrial Aerodynamics*, 96(8–9):1320–1331.

Simms, D., S. Schreck, and L. Fingeresh
2001. NREL unsteady aerodynamics experiment in the NASA–Ames wind tunnel: a comparison of predictions to measurements. Technical Report NREL/TP–500–29494, National Renewable Energy Laboratory, Golden, CO, USA.

Smagorinsky, J.
1963. General circulation experiments with the primitive equations. *Monthly Weather Review*, 91:99–164.

Snel, H., R. Houwink, G. van Bussel, and A. Bruining
1993. Sectional prediction of 3D effects for stalled flow on rotating blades and comparison with measurements. In *1993 European Community Wind Energy Conference Proceedings*, Pp. 395–399, Travemünde, Germany.

Sørensen, J. and W. Shen
2002. Numerical modelling of wind turbine wakes. *Journal of Fluids Engineering*, 124(2):393–399.

Sørensen, J. N.
2015. *General Momentum Theory for Horizontal Axis Wind Turbines*. Springer.

Sørensen, N. and S. Schreck
2012. Computation of the National Renewable Energy Laboratory Phase–VI rotor in pitch motion during standstill. *Wind Energy*, 15(3):425–442.

Sørensen, N. N., A. Bechmann, P. E. Réthoré, and F. Zahle
2014. Near wake Reynolds-averaged Navier—Stokes predictions of the wake behind the MEXICO rotor in axial and yawed flow conditions. *Wind Energy*, 17(1):75–86.

Sørensen, N. N., J. A. Michelsen, and S. Schreck
2002. Navier–Stokes predictions of the NREL phase VI rotor in the NASA Ames 80 ft x 120 ft wind tunnel. *Wind Energy*, 5(2-3):151–169.

SOWFA
2015. SOWFA: Simulator for wind farm applications. https://nwtc.nrel.gov/SOWFA. Accessed: October 2015.

Spalart, P.
2000. Strategies for turbulence modelling and simulation. *International Journal for Heat and Fluid Flow*, 21(3):252–263.

Spalart, P., W.-H. Jou, M. Strelets, and S. Allmaras
1997. Comments on the feasibility of LES for wings, and on a hybrid RANS/LES approach. In *Advances in LES/DNS, First AFOSR International Conference on DNS/LES*, Greyden Press, Louisiana Tech University.

Spalart, P. R. and S. R. Allmaras
1994. A one-equation turbulence model for aerodynamic flows. *La Recherche Aerospatiale*, 1(1):5–21.

Spalding, D. B.
1961. A single formula for the law of the wall. *Journal of Applied Mechanics*, 28(3):444–458.

Tangler, J. and M. Selig
1997. An evaluation of an empirical model for stall delay due to rotation for HAWTs. In *Proceedings of WindPower 97*, Austin, Texas.

Tangler, J. L.
2004. Insight into wind turbine stall and post–stall aerodynamics. *Wind Energy*, 7(3):247–260.

Troldborg, N.
2008. *Actuator Line Modeling of Wind Turbine Wakes*. PhD thesis, Technical University of Denmark.

Troldborg, N., C. Bak, N. Sørensen, H. Madsen, M. Réthoré, F. Zahle, and S. Guntur
2013. Experimental and numerical investigation of 3D aerofoil characteristics on a MW wind turbine. In *Proceedings of EWEA 2013*, Vienna, Austria.

Troldborg, N., J. N. Sørensen, and R. Mikkelsen
2007. Actuator line simulation of wake of wind turbine operating in turbulent inflow. In *Proceedings of the Science of Making Torque from Wind 2007*, Copenhagen, Denmark.

van Kuik, G.
1991. *On the limitations of Froude's actuator disc concept*. PhD thesis, Technical University Eindhoven, The Netherlands.

van Kuik, G. A. M., D. Micallef, I. Herráez, A. H. van Zuijlen, and D. Ragni
2014. The role of conservative forces in rotor aerodynamics. *Journal of Fluid Mechanics*, 750:284–315.

van Kuik, G. A. M., J. N. Sørensen, and V. L. Okulov
2015. Rotor theories by Professor Joukowsky: Momentum theories. *Progress in Aerospace Sciences*, 73:1–18.

Vermeer, L., J. Sørensen, and A. Crespo
2003. Wind turbine wake aerodynamics. *Progress in Aerospace Sciences*, 39(6-7):467–510.

Versteeg, H. and W. Malalasekera
1995. *An Introduction to Computational Fluid Dynamics*. Pearson Prentice Hall.

Wald, Q. R.
2006. The aerodynamics of propellers. *Progress in Aerospace Sciences*, 42(2):85–128.

Wilcox, D. C.
1998. *Turbulence Modelling for CFD*. DCW Industries.

Wood, D.
1991. A three-dimensional analysis of stall–delay on a horizontal–axis wind turbine. *Journal of Wind Engineering and Industrial Aerodynamics*, 37(1):1–14.

Wu, Y. T. and F. Porte-Agél
2010. Large-Eddy simulation of wind-turbine wakes: Evaluation of turbine parametrisations. *Boundary-Layer Meteorol*, 138:345–366.

Xiao, J., J. Wu, L. Chen, and Z. Shi
2011. Particle image velocimetry (PIV) measurements of tip vortex wake structure of wind turbine. *Appl. Math. Mech.*, 32(6):729—738.

Publications on which this thesis is based:

Peer-reviewed publications

I. HERRÁEZ, W. MEDJROUBI, B. STOEVESANDT AND J. PEINKE, Aerodynamic Simulation of the MEXICO Rotor, *Journal of Physics: Conference Series*, **555**, 012051, 2014.

I. Herráez performed the simulations, carried out the scientific analysis and wrote the manuscript. W. Medjroubi, B. Stoevesandt and J. Peinke had a supervising function.

I. HERRÁEZ, B. STOEVESANDT AND J. PEINKE, Insight into Rotational Effects on a Wind Turbine Blade Using Navier-Stokes Computations, *Energies*, **7**, 6798-6822, 2014.

I. Herráez performed the simulations, carried out the scientific analysis and wrote the manuscript. B. Stoevesandt and J. Peinke had a supervising function.

P. LIND, I. HERRÁEZ, M. WÄCHTER AND J. PEINKE, Fatigue Load Estimation through a Simple Stochastic Model, *Energies*, **7**, 8279, 2014.

The original idea of the article is from J. Peinke. P. Lind implemented the stochastic model and wrote the manuscript. I. Herráez carried out the fatigue load analysis. M. Wächter and J. Peinke had a supervising function.

G.A.M. VAN KUIK, D. MICALLEF, I. HERRÁEZ, A.H. VAN ZUJLEN AND D. RAGNI, The role of conservative forces in rotor aerodynamics, *Journal of Fluid Mechanics*, **750**, 284-315, 2014.

G.A.M. van Kuik proposed the main ideas of the paper. He also performed the analytical work and wrote the article. D. Micallef did the measurements and carried out panel code simulations. I. Herráez performed Navier-Stokes simulations based on the true blade geometry and on an actuator line model. A.H. van Zujlen contributed with actuator disk simulations. D. Ragni supported the experimental work.

I. HERRÁEZ, B. AKAY, G.J.W. VAN BUSSEL, J. PEINKE AND B. STOEVESANDT, Detailed Analysis of the Blade Root Flow of a Horizontal Axis Wind Turbine, *Wind Energy Science*, in review.

I. Herráez performed the simulations, carried out most of the scientific analysis and wrote the manuscript. B. Akay provided the experimental results. G.J.W. van Bussel contributed to the analysis of the measurements. J. Peinke and B. Stoevesandt had a supervising function.

I. HERRÁEZ, D. MICALLEF, G.A.M. VAN KUIK AND J. PEINKE, Numerical evidence of the influence of conservative forces on the performance of rotor blades, *Wind Energy Science*, in review.

I. Herráez performed the simulations, analysed the results and wrote the manuscript. D. Micallef and G.A.M. van Kuik contributed to the interpretation of the results. J. Peinke had a supervising function.

D. TRAPHAN, I. HERRÁEZ, P. MEINLSCHMIDT, F. SCHLÜTER, J. PEINKE AND G. GÜLKER, Remote surface damage detection on rotor blades of operating wind turbines by means of infrared thermography, *in preparation to be submitted to Applied Energy*.

D. Traphan carried out the measurements and wrote the manuscript. I. Herráez performed the simulations. The scientific analysis was done by D. Traphan and I. Herráez. P. Meinlschmidt and F. Schlüter contributed to the experimental work. J. Peinke and G. Gülker had a supervising function.

Book chapters

E. DANIELE, I. HERRÁEZ, B. STOEVESANDT AND J. PEINKE, DES study of airfoil lift coefficient sensitivity to flow turbulence, *Wind Energy - Impact of turbulence*, editors M. Hölling, J. Peinke and S. Ivanell, Springer Berlin Heidelberg, 2014.

Conference proceedings

B. AKAY, C. S. FERREIRA, G.J.W. VAN BUSSEL AND I. HERRÁEZ, Experimental and numerical quantification of the flow in the root region of a HAWT, *Proceedings of the 50th AIAA Aerospace Sciences Meeting*, Nashville, Tennessee, 2012.

I. HERRÁEZ, B. STOEVESANDT AND J. PEINKE, Validating OpenFOAM with the MEXICO Dataset, *Proceedings of the 7th EAWE PhD Seminar on Wind Energy in Europe*, Delft, the Netherlands, 2011.

I. HERRÁEZ, B. STOEVESANDT AND J. PEINKE, Numerical Study of Rotational Effects on Wind Turbines, *Proceedings of the DEWEK 2015*, Bremen, 2015.

Acknowledgments

Working on this thesis has been an enjoyable and rewarding adventure thanks to many people who supported me in one way or the other.

I would like to express my sincere gratitude to *Prof. Joachim Peinke* for advising me, placing his trust and confidence in my work and giving me a lot of freedom for following my own interests and ideas. Many thanks to *Bernhard Stoevesandt* for his support and helping me to develop my background in the field of CFD. I am also very grateful to *Wided Medjroubi* for her guidance and encouragement in the first stage of the PhD. I thank *Prof. Martin Kühn* for willing to be part of the defence committee of this thesis.

Many thanks to my collaborators from the TU-Delft: I am specially grateful to *Prof. Gijs A.M. van Kuik* , with whom I had the privilege to cooperate during his research stay at the University of Oldenburg (and afterwards). He gave me a new perspective for my research and I really enjoyed each of our (not only scientific) discussions. I also would like to thank *Prof. Gerard J.W. van Bussel* for his insightful and motivating comments about our common work. I am grateful to *Busra Akay* for sharing her experimental work with me and for the fruitful collaboration. Thanks a lot too to *Daniel Micallef*, from whom I learned much in our common articles.

I would like to express my gratitude to the participants of the MexNext-project for the insightful meetings and discussions.

I thank *Stefan Albensoeder* for his support with the computer cluster of the University of Oldenburg and for his kind help with any kind of IT problems. I am also very grateful to my colleges from the CFD group *Hamid Rahimi, Bastian Dose, Lena Vorspel, Sebastian Ehrich, Michael Schwarz, Elia Daniele, José Parra, Jonas Schmidt, Carlos Peralta, Matthias Schramm, Samuel Chang, and Cherif Mihoubi* for the relaxed and friendly working atmosphere. Many thanks also to other colleges of the TWiSt and We-Sys groups including *Philip Rinn, Matthias Wächter, Mike Hölling, Patrick Milan, Gerd Gülker, Jannik Schottler, Nico Reinke, Jarek Puczylowski, Stanislav Rockel, Alan Morales, Luis Vera-Tudela, Juan José Trujillo* and many others that contributed to make my stay at the University of Oldenburg an unforgettable experience. Special thanks to *Dominik Traphan* and *Pedro Lind* for the enjoyable cooperations within our research group. I would like to extend my sincere gratitude also to *George Pechlivanoglou*, who encouraged me to do this PhD.

I am very grateful to my parents and sister as well as to *Herena* for their continuous support not only during this thesis, but always. Last but no least, my deepest thankfulness goes to my daughters *Zoe* and *Yara*, who had to share their dad too often with this thesis.

Curriculum vitae

Personal data:

Name	Iván Herráez Hernádez
Date of birth	30.01.1979
Place of birth	Barcelona (Spain)
Nationality	Spanish

Education:

10/2010 – 12/2015	Doctoral student under the supervision of Prof. Dr. Peinke at University of Oldenburg, Germany
10/2005 – 04/2007	M.Sc. Renewable Energy at the University of Oldenburg, Germany.
10/1998 – 08/2002	B.Sc. Mechanical Engineering at the University of León, Spain. Exchange student at the FH-Ulm (WS00-01/SS01) and the RWTH-Aachen (WS01-02/SS02)

Professional experience:

10/2014 – present	Leader of the subgroup “CFD” in the research group of Prof. Dr. Peinke at the University of Oldenburg, Germany
05/2007 – 09/2010	Development engineer at the company Nordex GmbH. Load calculation and structural-dynamic analysis of wind turbines.

Erklärung

Ich erkläre hiermit, dass ich diese Arbeit selbstständig verfasst und nur die angegebenen Hilfsmittel benutzt habe.

Oldenburg, den 04. Januar 2016

.....

(Iván Herráez Hernádez)